Effects of Polydispersity in Bubbly Flows

Thesis by

Keita Ando

In Partial Fulfillment of the Requirements

for the Degree of

Doctor of Philosophy

California Institute of Technology

Pasadena, California

2010

(Defended May 20, 2010)

In memory of Kiyoko Tsukamoto (1920–1994).

Acknowledgments

First and foremost, I would like to express my sincerest thanks to my advisors, Professors Tim Colonius and Chris Brennen for their guidance throughout these past five years. With awe of their sharp eyes for flow physics, I always enjoyed discussing my research with them. I do appreciate their generosity that allowed me to pursue my own ideas. I also thank Professors Joseph Shepherd and Guruswami Ravichandran for serving on my thesis committee and for their helpful comments.

I was very fortunate to collaborate with many researchers. Discussions with Professor Rob Hagmeijer really helped me understand the fundamental physics of polydisperse bubbly flows. Professors Toshiyuki Sanada and Kazuaki Inaba generously conducted water-hammer experiments in order to validate my physical model. Sanada-san's technique to create small bubbles was particularly valuable. I am also grateful to Jason Damazo and Rafal Porowski for their beautiful bubble images.

I would also like to express my gratitude to the Computational Flow Physics Group members: Eric Johnsen, Guillaume Brès, Kunihiko Taira, Jen Frank, Kristján Gudmundsson, Jeff Krimmel, Won Tae Joe, Vedran Coralic, Sebastian Liska Cabrera, and Matthew Inkman. Especially, I appreciate cavitation group meetings with Eric, Jeff, and Vedran. My special thanks go to Jeff and Jen who have long been maintaining the computational resources. I also had great times with postdocs and visitors, Arnab Samanta, Daniel Appelö, Daniel Fuster, Shusuke Hori, Tomohiro Nishiyama, and Satoshi Yokojima.

I am very proud that I worked with Professors Colonius and Brennen here at Caltech. Certainly, they have been a model of professional scientists for me. Caltech is truly special, offering great education and research environment with leading scientists and engineers. I could not have come to the special place without my parents' understanding and support.

This work was supported by the DoD MURI on Mechanics and Mechanisms of Impulse Loading, Damage and Failure of Marine Structures and Materials through the Office of Naval Research (ONR Grant No. N00014-06-1-0730).

Abstract

This thesis concerns the dynamics of bubbly flows with a distribution of equilibrium bubble sizes. The main goal is to formulate the physical and numerical models of continuum bubbly flows that enable us to efficiently compute the average mixture dynamics. Numerical simulations are conducted to quantify the effects of bubble size distributions on the averaged dynamics for several model flows.

First, the ensemble-averaged conservation laws for polydisperse bubbly flows are derived. One-way-coupled flow computations are conducted to illustrate that the different-sized bubbles can oscillate with different frequencies. The resulting phase cancellations can be regarded as an apparent damping of the averaged dynamics of polydisperse flows. A high-order-accurate finite-volume method is then developed to compute the flow, paying special attention to issues of wave dispersion and stiffness.

Next, computations of one-dimensional shock propagation through bubbly liquids are performed. The numerical experiments reveal that the bubble size distribution has a profound impact on the averaged shock structure. If the distribution is sufficiently broad, the apparent damping due to the phase cancellations can dominate over the single-bubble-dynamic dissipation (due to thermal, viscous, and compressibility effects) and the averaged shock dynamics become insensitive to the individual bubble dynamics. One-dimensional cloud cavitation caused by fluid-structure interaction is also solved to investigate the collapse of cavitation clouds with both monodisperse and polydisperse nuclei. The phase cancellations among the cavitation bubbles with broad nuclei size distributions are found to eliminate violent cloud collapse in the averaged dynamics.

Finally, shock propagation through a bubbly liquid-filled, deformable tube is considered. The quasi-one-dimensional conservation law that takes into account structural deformation is formulated

and steady shock relations are derived. The results are compared to water-hammer experiments; the present shock theory gives better agreement with the measured wave speeds than linear theory. This indicates that the gas-phase nonlinearity needs to be included to accurately predict the propagation speeds of finite-amplitude waves in a deformable tube filled with a bubbly liquid.

Contents

List of Figures

List of Tables

Nomenclature

Greek letters

α	Void fraction
α_T	Thermal diffusivity
β	Cloud interaction parameter
γ	Liquid stiffness
δ	Dirac's delta
ϵ_θ	Hoop strain
η	Korteweg–Joukowsky FSI parameter
Θ	Transfer coefficient
κ	Polytropic index
λ	Eigenvalue
μ	Viscosity
μ_i	ith moment of bubble radius
ν	Poisson's ratio
ν_l	Kinematic viscosity of a liquid
ρ	Mixture density

ρ_l	Liquid density
σ	Standard deviation
τ	Time constant
Υ	Surface tension
χ_v	Mass fraction of vapor
ψ	Taylor's FSI parameter
ω	Temporal angular frequency
ω_i	Natural frequencies of oscillations of a spherical bubble cloud
ω_N	Natural frequency of bubble oscillations
φ	Bubble-dynamic variable

Roman letters

A	Internal tube area
$\mathbf{A}$	Jacobian matrix ($\partial\mathbf{f}/\partial\mathbf{q}$)
a	Internal tube radius
a^{att}	Attenuation
B	Tensile strength of a liquid
C	Sonic speed of a liquid at a bubble wall
c	Sonic speed
c_J	Korteweg–Joukowsky wave speed
c_p	Specific heat at constant pressure
c^{ph}	Phase velocity

$\mathcal{D}$	Binary diffusion coefficient
E	Young's modulus
e	Internal energy
f	Temporal frequency
$\mathbf{f}$	Flux vector
$\mathbf{f}^s$	Phase interaction flux vector
$f(R_0)$	Normalized distribution of equilibrium bubble radius
H	Enthalpy of a liquid at a bubble wall
h	Tube wall thickness
$\mathbf{I}$	Identity tensor
K	Bulk modulus
k	Thermal conductivity
L	Wavelength
l	Mean bubble spacing
M	Molecular weight
M_s	Shock Mach number
m	Mass
$\dot{m}_v''$	Mass flux of vapor
n	Bubble number density
p_b	Internal bubble pressure
p_{bw}	Bubble wall pressure

p_g	Partial pressure of noncondensible gases
p_l	Liquid pressure
p_{l0}	Ambient pressure
p_s	Shock pressure
p_v	Vapor pressure
$\tilde{p}$	Pressure fluctuations due to phase interactions
$\mathbf{q}$	Column vector of conserved variables
R	Bubble radius
R_0	Equilibrium bubble radius
R_0^{ref}	Probable bubble size
R_c	Radius of a spherical bubble cloud
$\mathfrak{R}$	Gas constant
r	Radial coordinate
r_s	Standoff distance
s	HLLC wave speed
$\mathbf{s}$	Column vector of bubble-dynamic sources
$\mathbf{s}^g$	Column vector of geometric sources
T_w	Bubble wall temperature
t	Time
U_s	Shock speed
u	Velocity component

$\mathbf{u}$	Velocity vector
$\mathcal{V}$	Control volume
x	Axial coordinate
x_v	Mole fraction of vapor
z	Underwater depth

Acronyms

CFL	Courant–Friedichs–Lewy (number)
ENO	Essentially non-oscillatory
FSI	Fluid-structure interaction
FV	Finite volume
STP	Standard temperature and pressure (20 °C, 101 kPa)
TNT	Trinitrotoluene
TVD	Total variation diminishing
UNDEX	Underwater explosion
WENO	Weighted ENO

Chapter 1

Introduction

1.1 Motivation

Complex bubbly flows are ubiquitous in engineering flows, such as underwater explosions, industrial piping systems and hydraulic machinery (Cole, 1948; Wylie & Streeter, 1993; Brennen, 1994). Seawater near the sea surface contains fairly big bubbles due to breaking waves. Even for liquid flows with small nuclei populations, the interaction with structures often produces tension waves (or negative pressure regions) that can cause cavitation with heterogeneous nucleation, and complex two-phase flow regimes are encountered. In most cases, cavitation has negative aspects that include performance loss of hydraulic machinery, and cavitation noise and erosion (Arndt, 1981; Tijsseling, 1996; Bergant *et al.*, 2006). The resulting gas or vapor bubbles lead to wave dispersion; the dynamics of bubbly mixtures cannot be described by simple barotropic relations (Brennen, 1995, 2005). An understanding of complex dynamics of such bubbly flows is still inadequate for many engineering applications.

The dynamics of bubbly flows have been theoretically, numerically and experimentally studied by many researchers. Difficulties with the physical and numerical modeling arise from the fact that bubbly flows contain multiple time and spatial scales that range from individual bubble collapse to average mixture dynamics. When it comes to tackling such a scale separation, it is practical to solve mixture-averaged conservation equations rather than solving the full equations of motion for each distinct phase; the mixture is considered to be a *continuum* or *homogeneous* medium. The term

homogeneous flow often indicates a flow with negligible relative motion between the host liquid and the bubbles (Brennen, 1995, 2005). In most of the previous studies, for simplicity and numerical efficiency, the equilibrium bubbles are assumed single-sized; namely the mixture is *monodisperse*. However, most flows of practical interest consist of bubbles with a broad range of the equilibrium sizes. In this case, the mixture is *polydisperse*.

The goals of this thesis are to derive a continuum bubbly flow model that incorporates a distribution of equilibrium bubble nuclei sizes and develop a robust and efficient numerical scheme in order to capture unsteady wave phenomena in bubbly flows. We use numerical simulations to quantify the effects of polydispersity on average mixture dynamics for a series of model problems associated with wave propagation and cavitation cloud collapse in liquids.

1.2 Historical perspective

1.2.1 Shock dynamics

Theoretical and numerical models have been developed to investigate shock dynamics in bubbly flows. Most of the studies rely on continuum models for monodisperse mixtures. In the classic papers of van Wijngaarden (1968, 1972), volume-averaged mixture quantities were derived in order to average out local scattering due to the dynamics of individual bubbles, and averaged conservation laws for bubbly flows were formulated based on heuristic, physical reasoning. Zhang & Prosperetti (1994) developed an ensemble-averaging technique to derive the mixture-averaged equations. By linearizing van Wijngaarden's equations, the dispersion relation can be obtained (Commander & Prosperetti, 1989). The computations of the mixture-averaged equations coupled to a Rayleigh-Plesset-type equation for spherical bubble dynamics (Nigmatulin *et al.*, 1988; Watanabe & Prosperetti, 1994; Kameda & Matsumoto, 1996; Kameda *et al.*, 1998) reproduced averaged shock structures. The direct numerical simulations of shock propagation in bubbly liquids (Delale *et al.*, 2005; Delale & Tryggvason, 2008) are an important step to quantify the scattering effect.

A finite cloud of bubbles has been extensively studied as a canonical example. One of the earliest

attempts is the work of van Wijngaarden (1964) that considered the collapse of a bubbly layer near a wall. The study of the linearized dynamics of spherical bubble clouds (d'Agostino & Brennen, 1989) identified the natural frequencies of the cloud that can be much smaller than the natural frequency of individual bubble oscillations. The nonlinear computations of bubble clouds (Chahine, 1982; Omta, 1987; Wang & Brennen, 1999; Colonius *et al.*, 2000) indicate that cloud collapse can generate higher pressure than that predicted by superposition of single-bubble calculations in the corresponding one-way-coupling case (in which interactions among the bubbles through the averaged field are ignored); this violent cloud collapse may account for cavitation noise and erosion. All of the above analyses were confined to the case of monodisperse mixtures. However, the computations of a spherical cloud with a distribution of equilibrium bubble sizes (Wang, 1999; Shimada *et al.*, 2000) suggest a profound impact of polydispersity on the averaged dynamics.

The continuum models have been validated by experiments. In the pioneering work of Campbell & Pitcher (1958), shock propagation in a bubbly liquid-filled, vertical tube was considered, and their results showed reasonable agreement with the steady shock relations derived from mixture-averaged equations. Subsequent experiments (Noordzij & van Wijngaarden, 1974; Beylich & Gülhan, 1990; Kameda & Matsumoto, 1996; Kameda *et al.*, 1998) used a similar device with careful control of bubble sizes, and identified oscillatory shock structures. Particularly, in the experiment of Kameda *et al.* (1998), monodisperse mixtures with a spatially uniform bubble distribution were carefully created; the experimental data were in quantitative agreement with their continuum bubbly flow computations with accurate evaluations of individual bubble dynamics. Beylich & Gülhan (1990) reported on the polydisperse case in which the smoothed shock structure was seen. Unfortunately, experimental observations on the shock dynamics of polydisperse mixtures are rather limited.

1.2.2 Underwater explosions and cavitation

Cavitation reloading on submerged structures is of considerable interest in underwater explosion (UNDEX) research (Rajendran, 2008). The fluid-structure interaction (FSI) often causes cloud cavitation near the target surface, and the subsequent collapse of the cloud of cavitation bubbles can

reload the target. In the pioneering study of Taylor (1950), the interaction of a plane shock with an infinite flat plate was considered, and the linearized solutions that indicate the occurrence of negative pressure in the non-cavitating liquid phase were obtained. Subsequently, the pressure cutoff model that assumes uniform pressure within cavitating regions was proposed to modify Taylor's theory (Kennard, 1950; Temperley, 1950). Bleich & Sandler (1970) assumed bilinear fluids, and computed cavitation in Taylor's problem using a method of characteristics. Wardlaw & Luton (2000) simulated close-in underwater explosions in multi-dimensions, and reproduced cavitation reloading based on the cutoff model. More recently, Xie *et al.* (2007, 2008, 2009) employed a barotropic relation to describe the state of cavitation cloud, and examined the effect of cavitation reloading on deformable structures. Although these cavitation models may replicate quasistatic trends in cavitating flows, it is not possible to accurately capture the unsteadiness.

UNDEX/FSI experiments have been conducted by structural engineers (Nurick & Martin, 1989; Mair, 1999; Rajendran & Narasimhan, 2006*a*); the classical experimental configuration is a flat plate with shock loading due to detonation of high explosives. The photographs of Eldridge *et al.* (1950) illustrate a cloud of cavitation bubbles near a shock-loaded plate. Rajendran & Satyanarayana (1997) and Rajendran & Narasimhan (2006*b*) observed cavitation reloading from pressure and strain evolution on a deformed plate surface. Brett *et al.* (2000) and Brett & Yiannakopolous (2008) also confirmed the collapse of cavitation clouds adjacent to a submerged cylinder loaded from a nearby explosion. Chambers *et al.* (2001) considered explosions inside a water-filled tube and measured cavitation reloading on the wall.

Dynamic loading of fluid-filled, deformable tubes can also be regarded as an UNDEX/FSI model problem (Kedrinskii, 2005; Shepherd & Inaba, 2009). Liquid-filled tubes were first studied by Korteweg (1878) and Joukowsky (1898), who introduced a linear wave speed that accounts for the compressibility of both the liquid and the structure. Later, Skalak (1956) include the effect of wave dispersion caused by the structural dynamics on their linear theory. The Korteweg–Joukowsky wave speed in the case of bubbly liquids was validated by Kobori *et al.* (1955). On the experimental side, an underwater shock simulator in which the impact of an accelerated projectile in the axial direction

generates a coupled stress wave propagating in the tube and fluid was proposed independently by Dashpande *et al.* (2006) and Espinosa *et al.* (2006). With a similar experimental setup, Inaba & Shepherd (2010) measured flexural waves in a water-filled steel tube, and obtained reasonable agreement with Skalak's water-hammer theory. To the author's knowledge, a (nonlinear) shock theory that includes both structural compressibility and bubbles has not been presented previously.

1.3 Contributions and outline

The main contributions of this thesis are:

- Formulation of a continuum bubbly flow model that incorporates a distribution of equilibrium bubble sizes.
- Development and verification of a high-order-accurate, shock-capturing algorithm to resolve wave dispersion and stiffness in polydisperse bubbly flows.
- Robust computations of shock propagation in bubbly liquids and cloud cavitation caused by structural interaction with UNDEX shocks.
- Quantification of the effects of polydispersity on average mixture dynamics.
- Assessment of cavitation reloading on structures in UNDEX problems.
- Derivation and validation of a steady shock theory of a bubbly liquid filled in a deformable cylindrical tube.

The contents of this thesis are organized as follows. In chapter 2, the continuum and single-bubble-dynamic models with their assumptions are presented, and the model limitations are discussed. One-way-coupled flow computations are also considered in order to clarify some fundamental issues arising in polydisperse flows. Chapter 3 provides the numerical scheme that includes spatial discretization, time marching, and boundary condition implementation. The verification of the numerical method is presented using some test problems. In chapter 4, one-dimensional shock

propagation in dilute bubbly liquids is computed, and the effect of polydispersity on the averaged shock dynamics is investigated. Parameter studies of probable bubble sizes, void fractions and shock strengths are also conducted. Chapter 5 examines dynamics of cavitation clouds caused by structural interaction with UNDEX shocks that is modeled using Taylor's theory. In chapter 6, shock propagation through a bubbly liquid filled in a deformable cylindrical tube is considered. Quasi-one-dimensional bubbly flow equations including FSI are formulated, and the steady shock relations are derived. The theoretical and measured wave speeds are compared, and the model limitations are discussed.

Chapter 2

Physical model

The main goal of this chapter is to provide the system of equations that govern the averaged dynamics of polydisperse bubbly flows. First, the continuum bubbly flow model is formally derived based on an ensemble-averaging approach, and the model limitations are discussed. The single-bubble-dynamic model that includes the effects of heat transfer, and liquid viscosity and compressibility is then proposed. The resulting one-dimensional system are presented for computational purposes. Moreover, the equality of ensemble and volume averages is discussed based on the ergodic hypothesis. One-way-coupled flow computations are finally considered to elucidate the fundamental physics of polydisperse flows.

2.1 Continuum bubbly flow model

2.1.1 Ensemble-averaged equations

With the ensemble-averaging technique of Zhang & Prosperetti (1994), one may formally derive the continuum bubbly flow model in order to evaluate the average mixture dynamics. The key concept of the ensemble averaging is to statistically treat the dynamical state of bubbly mixtures in which a large number of realizations of spherical bubbles (or isotropic scatters) exist. In other words, we discard any scattering effects in a specific realization, but explore the statistically averaged dynamics. Even though direct interactions between the neighboring bubbles are minimal, there can still appear (indirect) interactions among the bubbles through the averaged field; the problem is *two-*

way-coupled. In what follows, we present the ensemble-averaged conservation law for polydisperse bubbly flow with the model assumptions. The complete description of the derivation can be found in Zhang & Prosperetti (1994), and is also summarized in appendix A.

The continuum model assumes that (a) the bubbles are spherical; (b) mutual interactions among the bubbles are negligible except through their effect on the mixture-averaged flow; (c) wavelengths in the mixture are large compared to the mean bubble spacing; (d) the bubbles advect with the ambient liquid velocity (no slip); and (e) density and velocity fluctuations in the liquid phase are uncorrelated.

Assumption (a) implies that fission and coalescence of the bubbles are not permitted, so that the bubble number is conserved in time. Assumption (c) is used for the model closure. Relative motion between the phases has been shown to have minimal impact on linear wave propagation (d'Agostino *et al.*, 1988) and also plays a minor role in shock propagation (Kameda & Matsumoto, 1996). Assumption (e) is reasonable due to the fact that the velocity fluctuations caused by the bubble dynamics concentrate in the vicinity of the bubbles, where the liquid is effectively incompressible (Prosperetti & Lezzi, 1986).

Under these assumptions, we write the ensemble-averaged equations as

$$\frac{\partial \rho}{\partial t} + \nabla \cdot (\rho \mathbf{u}) = 0, \tag{2.1}$$

$$\frac{\partial \rho \mathbf{u}}{\partial t} + \nabla \cdot \left[\rho \mathbf{u}\mathbf{u} + (p_l - \tilde{p})\mathbf{I}\right] = 0, \tag{2.2}$$

$$\frac{\partial \alpha}{\partial t} + \nabla \cdot (\alpha \mathbf{u}) = 3\alpha \frac{\overline{R^3 \dot{R}^2}}{\overline{R^3}}, \tag{2.3}$$

where ρ is the mixture density, $\mathbf{u}$ is the mixture velocity vector, p_l is the averaged liquid-phase pressure, $\mathbf{I}$ is the identity tensor, α is the void fraction, R is the bubble radius, and $\dot{R}$ is the bubble wall velocity. For dilute cases (i.e., low void fraction), the mixture density is well approximated by $(1-\alpha)\rho_l$ where ρ_l is the liquid density. The averaged liquid pressure may be described by the Tait

equation of state (Thompson, 1972),

$$\frac{p_l + B}{p_{l0} + B} = \left(\frac{\rho_l}{\rho_{l0}}\right)^\gamma = \frac{1}{\rho_{l0}^\gamma}\left(\frac{\rho}{1-\alpha}\right)^\gamma, \tag{2.4}$$

where ρ_{l0} is the reference liquid density at the ambient pressure p_{l0}, and γ and B denote stiffness and tensile strength of the liquid, respectively. For water, we take $\gamma = 7.15$ and $B = 304$ MPa. Note that the constant value of B implies the homentropic behavior of the liquid.

The term $\tilde{p}$ in the momentum flux in equation (2.2) represents pressure fluctuations due to the phase interactions,

$$\tilde{p} = \alpha\left(p_l - \frac{\overline{R^3 p_{bw}}}{\overline{R^3}} - \rho\frac{\overline{R^3\dot{R}^2}}{\overline{R^3}}\right), \tag{2.5}$$

where p_{bw} is the bubble wall pressure described by the dynamic boundary condition (Brennen, 1995),

$$p_{bw} = p_b - 4\mu_l\frac{\dot{R}}{R} - \frac{2\Upsilon}{R}. \tag{2.6}$$

Here, p_b is the internal bubble pressure (sum of noncondensible gas pressure p_g and vapor pressure p_v), μ_l is the liquid viscosity and Υ is the surface tension.

The overbar in equations (2.3) and (2.5) denotes moments with respect to the (normalized) distribution of equilibrium bubble sizes, $f(R_0)$,

$$\overline{\varphi}(\mathbf{x}, t) = \int_0^\infty \varphi(\mathbf{x}, t; R_0) f(R_0) dR_0, \tag{2.7}$$

where R_0 is the equilibrium bubble radius corresponding to the ambient pressure and φ represents any of $R^2\dot{R}$, $R^3 p_{bw}$, $R^3\dot{R}^2$ or R^3. Note that the functional dependence of R_0 on the size distribution is assumed spatially uniform. This assumption is valid for all times due to the no-slip assumption (d). For example, the void fraction is defined as

$$\alpha = \frac{4\pi}{3} n \overline{R^3}, \tag{2.8}$$

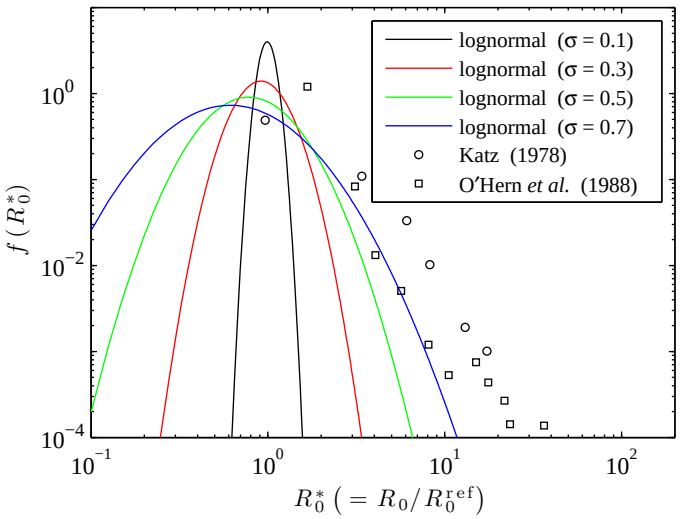

Figure 2.1: Normalized distributions of the equilibrium bubble radius. The probable size, R_0^{ref}, is set to be 10 μm.

where n is the number of bubbles per unit volume of the mixture and is conserved in time because of the assumption (a); namely

$$\frac{\partial n}{\partial t} + \nabla \cdot (n\mathbf{u}) = 0. \tag{2.9}$$

It should be noted that the phase interaction term $\tilde{p}$ does not appear in the volume-averaged equations of van Wijngaarden (1968, 1972). For linearized dynamics of the bubbles, $\tilde{p}$ contains corrections of order at most $O(\alpha^2)$ so that the ensemble-averaged equations (2.1) to (2.3) reduce to van Wijngaarden's equations in the linear context.

2.1.2 Model distributions of equilibrium bubble sizes

We model the distribution of the equilibrium bubble radius using a lognormal function with the probable size R_0^{ref} and standard deviation σ,

$$f(R_0^*) = \frac{1}{\sqrt{2\pi}\sigma R_0^*} \exp\left(-\frac{\ln^2 R_0^*}{2\sigma^2}\right), \tag{2.10}$$

where $R_0^* = R_0/R_0^{\mathrm{ref}}$. The lognormal function (2.10) approaches zero exponentially in the limit of $\ln R_0^* \to \infty$, so that contributions of extremely large sizes, which may deteriorate the continuum

model accuracy, to integration (2.7) can be minimized. In the limit of $\sigma \to 0$, the lognormal function (2.10) reduces to the Dirac delta function,

$$f(R_0^*) = \delta(R_0^* - 1), \tag{2.11}$$

which models monodisperse mixtures.

Figure 2.1 shows the measured nuclei size distributions in a water tunnel (Katz, 1978) and the ocean (O'Hern *et al.*, 1988), together with the lognormal function (2.10). It follows that $\sigma = 0.7$ may be a reasonable value to model the actual distributions in engineering flows and the ocean, but we use the distribution (2.10) as illustrative of the qualitative effects of polydispersity rather than to model a particular system. The numerical methods developed in the next chapter are independent of this choice, and an empirically determined distribution could easily be employed in future computations.

2.1.3 Model limitations

We now discuss specific limitations associated with assumptions (a) and (b) in section 2.1.1, which are essential for deriving the continuum model (2.1) to (2.3).

The spherical-bubble assumption (a) implies no fission of the bubbles. Possible mechanisms responsible for the fission are a re-entrant jet and a Rayleigh-Taylor-type instability (Brennen, 2002; Johnsen & Colonius, 2009). If the thickness of the incident shock is comparable to or smaller than the bubble sizes, the bubbles distort nonspherically and may finally result in fission due to the re-entrant jet. However, the interaction of the averaged pressure field and the bubble cloud is known to broaden the shock thickness. As a result, the bubble fission does not occur frequently if the shock strength is sufficiently small (Beylich & Gülhan, 1990). For strong shocks, the bubble collapse is so violent that nonspherical distortions arise and fission is likely. Accounting for bubble fission in continuum models is a challenge not yet met.

For assumption (b) to be valid, the mean bubble spacing ($l = n^{-1/3}$) must be much larger than the bubble sizes. It follows from equation (2.8) that this condition is satisfied in the dilute

limit (i.e., $\alpha \to 0$). The acoustic theory of linear waves in monodisperse bubbly liquids (Carstensen & Foldy, 1947; Commander & Prosperetti, 1989) is known to overestimate attenuation under the resonant condition since the bubble/bubble interactions can never be ignored even in the dilute limit (Waterman & Truell, 1961; Commander & Prosperetti, 1989). Inclusion of the broad size distribution (e.g., large standard deviation σ in lognormal distribution (2.10)) can de-emphasize errors associated with resonance since the probability that a bubble of certain size is under resonance is low among a broad spectrum of R_0 (Feuillade, 1996).

2.2 Single-bubble-dynamic model

2.2.1 Model assumptions

In order to close the continuum bubbly flow model, there is a need to solve the single bubble dynamics, but the detailed conservation equations of both the liquid phase and the bubble contents are computationally expensive. This necessitates employing a Rayleigh-Plesset-type equation with the following simplifications. The spherical-bubble-dynamic model assumes that (f) the bubble contents (noncondensible gas and vapor) have spatially uniform pressure; (g) the bubble contents are perfect; (h) the liquid is cold (far from the boiling point); (i) the mass of noncondensible gas in the bubble is unchanged; (j) phase change occurs instantaneously; (k) Fick's law holds for mass diffusion between the noncondensible gas and the vapor; and (l) the transport properties of the bubble contents are constant.

The homobaric assumption (f) is valid since the inertia of the bubble contents is negligible compared to that of the liquid. The cold liquid assumption (h) leads to undisturbed liquid temperature at the bubble wall, so that the energy equation in the liquid phase is unnecessary to solve (Prosperetti *et al.*, 1988; Preston *et al.*, 2007). The typical bubble growth rate due to mass transfer of dissolved air in water is so slow (compared to the bubble oscillation rate) that assumption (i) is reasonable (Plesset & Prosperetti, 1977). Assumptions (h) and (j) imply constant vapor pressure at the bubble wall, which is typically adequate except near the end of a violent bubble collapse

(Fujikawa & Akamatsu, 1980).

2.2.2 The Gilmore equation

The equation of Gilmore (1952),

$$R\ddot{R}\left(1-\frac{\dot{R}}{C}\right)+\frac{3}{2}\dot{R}^2\left(1-\frac{\dot{R}}{3C}\right)=H\left(1+\frac{\dot{R}}{C}\right)+\frac{R\dot{H}}{C}\left(1-\frac{\dot{R}}{C}\right), \tag{2.12}$$

is used to evaluate the spherical bubble dynamics. Here, the dot denotes the substantial time derivative, and H and C are the enthalpy and the sonic speed, respectively, at the bubble wall in the liquid:

$$H=\int_{p_l}^{p_{bw}}\frac{dp_l'}{\rho_l(p_l')},\quad C=\left(\left.\frac{dp_l}{d\rho_l}\right|_{p_l=p_{bw}}\right)^{\frac{1}{2}}, \tag{2.13}$$

where the bubble wall pressure p_{bw} is given by equation (2.6). In the dilute limit, the averaged liquid pressure p_l can be considered to be farfield pressure from the bubble in an infinite liquid (Takahira, 2004). Substitution of the Tait equation of state (2.4) into the above definitions yields the following expressions:

$$H=\frac{\gamma}{\gamma-1}\frac{p_{l0}+B}{\rho_{l0}}\left[\left(\frac{p_{bw}+B}{p_{l0}+B}\right)^{\frac{\gamma-1}{\gamma}}-\left(\frac{p_l+B}{p_{l0}+B}\right)^{\frac{\gamma-1}{\gamma}}\right], \tag{2.14}$$

$$C=\sqrt{\frac{\gamma(p_{l0}+B)}{\rho_{l0}}\left(\frac{p_l+B}{p_{l0}+B}\right)^{\frac{\gamma-1}{\gamma}}+(\gamma-1)H}. \tag{2.15}$$

2.2.3 Equations for bubble contents

Consider the bubble energy equation, which is coupled to the Gilmore equation (2.12). The rate of the bubble energy change equals the sum of work done by the bubble wall and energy transfered due to the mass flux of vapor and the heat flux at the bubble wall; namely

$$\frac{d}{dt}\int_0^{R(t)}(\rho_g e_g+\rho_v e_v)4\pi r'^2dr'=4\pi R^2\left(-\dot{R}p_b+c_{pv}T_w\dot{m}_v''+k_{bw}\left.\frac{\partial T}{\partial r}\right|_w\right), \tag{2.16}$$

where the subscripts g, v, b and w denote noncondensible gas, vapor, bubble contents (gas/vapor mixture) and bubble wall properties, respectively, e is the internal energy, c_p is the specific heat at constant pressure, T_w is the bubble wall temperature, $\dot{m}''$ is the mass flux, k is the thermal conductivity, T is the temperature (defined inside the bubble) and r is the radial coordinate measured from the bubble center. With assumptions (f) and (g), the energy balance (2.16) reduces to the following equation (Nigmatulin *et al.*, 1981; Prosperetti *et al.*, 1988),

$$\dot{p}_b = \frac{3\gamma_b}{R}\left(-\dot{R}p_b + \mathfrak{R}_v T_w \dot{m}_v'' + \frac{\gamma_b - 1}{\gamma_b} k_{bw} \left.\frac{\partial T}{\partial r}\right|_w\right), \tag{2.17}$$

where γ_b is the specific-heat ratio of the bubble contents and $\mathfrak{R}$ is the gas constant. In the derivation, it is assumed that the specific ratio of noncondensible gas, γ_g, is nearly the same as that of vapor, γ_v, so that $\gamma_b \approx \gamma_g \approx \gamma_v$. Note that the bubble wall temperature T_w is undisturbed for all times and the vapor pressure p_v is constant due to assumptions (h) and (j).

The species conservation (k) requires

$$\dot{m}_v'' = \frac{\mathcal{D}\rho_{bw}}{1 - \chi_{vw}} \left.\frac{\partial \chi_v}{\partial r}\right|_w, \tag{2.18}$$

where χ_v is the mass fraction of the vapor and $\mathcal{D}$ is the binary diffusion coefficient. It follows from the perfect gas law (g) that χ_{vw} and ρ_{bw} are written as

$$\chi_{vw} = \left[1 + \frac{\mathfrak{R}_v}{\mathfrak{R}_g}\left(\frac{p_b}{p_v} - 1\right)\right]^{-1}, \tag{2.19}$$

$$\rho_{bw} = \frac{p_v}{\chi_{vw}\mathfrak{R}_v T_w}. \tag{2.20}$$

The thermal conductivity for the bubble contents is taken from a semi-empirical formula (Bird *et al.*, 1960):

$$k_{bw} = \frac{x_{vw}k_v}{x_{vw}\phi_{vv} + (1 - x_{vw})\phi_{vg}} + \frac{(1 - x_{vw})k_g}{x_{vw}\phi_{gv} + (1 - x_{vw})\phi_{gg}}, \tag{2.21}$$

where

$$\phi_{pq} = \frac{1}{\sqrt{8}}\left(1+\frac{M_p}{M_q}\right)^{-\frac{1}{2}}\left[1+\left(\frac{\mu_p}{\mu_q}\right)^{\frac{1}{2}}\left(\frac{M_q}{M_p}\right)^{\frac{1}{4}}\right]^2, \tag{2.22}$$

$$x_{vw} = \frac{M_g \chi_{vw}}{M_v + (M_g - M_v)\,\chi_{vw}}. \tag{2.23}$$

Here, M_p (or μ_p) is the molecular weight (or the viscosity) of component p, and x_{vw} is the mole fraction of the vapor at the bubble wall.

For efficient computations, the temperature and concentration gradients, in equations (2.17) and (2.18), at the bubble wall are estimated using the reduced-order model of Preston *et al.* (2007), which has been shown to be accurate for small bubbles. The details of Preston's model, together with the (dimensionless) bubble-dynamic equations, are described in appendix B.

It should be noted that the polytropic gas obeys

$$p_b = p_v + p_{g0}\left(\frac{R}{R_0}\right)^{-3\kappa}, \tag{2.24}$$

where p_{g0} is the partial pressure of the noncondensible gas in the equilibrium state and κ is the polytropic index; $\kappa = 1$ implies constant bubble temperature and $\kappa = \gamma_g$ would model adiabatic behavior. In this case, the bubble energy balance (2.17) is unnecessary to solve.

2.2.4 The conservation form

We now write the bubble-dynamic equations (parameterized by R_0) in a conservation form, which is suitable for shock computations (LeVeque, 1992):

$$\frac{\partial n\varphi}{\partial t} + \nabla\cdot(n\varphi\mathbf{u}) = n\dot{\varphi}. \tag{2.25}$$

In this form, the bubble-dynamic variables, φ, are treated as Eulerian variables (i.e., $\varphi = \varphi(\mathbf{x}, t; R_0)$) rather than Lagrangian particles (Watanabe & Prosperetti, 1994). Since we assume a large number

of the bubbles in mixtures, the bubbles may be considered to be distributed continuously in space. If we evaluate the heat and vapor fluxes using Preston's model, the bubble pressure p_b and the mass of vapor m_v (in addition to R and $\dot{R}$) need to be included in φ.

2.3 The complete system

For simplicity, we write the resulting system in one dimension using a vector form:

$$\mathbf{q}_t + \mathbf{f}(\mathbf{q})_x = \mathbf{f}^s(\mathbf{q})_x + \mathbf{s}(\mathbf{q}), \tag{2.26}$$

where the subscripts denote partial derivatives. The column vectors are

$$\mathbf{q} = \begin{Bmatrix} \rho \\ \rho u \\ \alpha \\ n\varphi \end{Bmatrix}, \quad \mathbf{f} = \begin{Bmatrix} \rho u \\ \rho u^2 + p_l \\ \alpha u \\ n\varphi u \end{Bmatrix}, \quad \mathbf{f}^s = \begin{Bmatrix} 0 \\ \tilde{p} \\ 0 \\ 0 \end{Bmatrix}, \quad \mathbf{s} = \begin{Bmatrix} 0 \\ 0 \\ 3\alpha\frac{\overline{R^3\dot{R}^2}}{\overline{R^3}} \\ n\dot{\varphi} \end{Bmatrix}, \tag{2.27}$$

where u is the x-component velocity and $\mathbf{f}^s$ may be called the *phase interaction flux*. Note that the source terms, $\mathbf{f}^s$ and $\mathbf{s}$, vanish in the equilibrium state. Given the conserved variables $\mathbf{q}$, the bubble number density is computed by

$$n = \sqrt{\frac{4\pi}{3\alpha}\int_0^\infty (nR)^3 f(R_0) dR_0}. \tag{2.28}$$

The quasilinear form of equation (2.26) is

$$\mathbf{q}_t + \mathbf{A}\mathbf{q}_x = \mathbf{f}^s(\mathbf{q})_x + \mathbf{s}(\mathbf{q}), \tag{2.29}$$

where $\mathbf{A}$ is the Jacobian matrix ($\partial\mathbf{f}/\partial\mathbf{q}$). The eigenvalues of $\mathbf{A}$ are

$$\lambda_1 = u - \tilde{c}_l, \quad \lambda_2 = u + \tilde{c}_l, \quad \lambda_3 = \lambda_4 = u. \tag{2.30}$$

where $\tilde{c}_l$ is the sonic speed of the (Tait) liquid, c_l, with corrections of order $O(\alpha)$:

$$\tilde{c}_l = \frac{c_l}{1-\alpha} = \frac{1}{1-\alpha}\sqrt{\frac{\gamma(p_l + B)}{\rho_l}}. \tag{2.31}$$

The matrix of the right (column) eigenvectors (satisfying $\mathbf{A}\mathbf{r}_i = \lambda_i \mathbf{r}_i$) of $\mathbf{A}$ is

$$\mathbf{R} = [\mathbf{r}_1 \ \mathbf{r}_2 \ \mathbf{r}_3 \ \mathbf{r}_4] = \begin{bmatrix} \rho & \rho & \rho & 0 \\ \rho(u-\tilde{c}_l) & \rho(u+\tilde{c}_l) & \rho u & 0 \\ \alpha & \alpha & \alpha - 1 & 0 \\ n\varphi & n\varphi & 0 & 1 \end{bmatrix}, \tag{2.32}$$

where the fields associated with $\mathbf{r}_3$ and $\mathbf{r}_4$ are linearly degenerate and represent the contact waves. Note that the generalized Riemann invariants (Toro, 1999) reveal that across the contact waves, u and p_l are continuous but ρ, α and $n\varphi$ are discoutinuous. Correspondingly, the matrix of the left (row) eigenvectors (satisfying $\mathbf{l}_i\mathbf{A} = \lambda_i \mathbf{l}_i$) of $\mathbf{A}$ is

$$\mathbf{L} = \begin{bmatrix} \mathbf{l}_1 \\ \mathbf{l}_2 \\ \mathbf{l}_3 \\ \mathbf{l}_4 \end{bmatrix} = \begin{bmatrix} \frac{u+(1-\alpha)\tilde{c}_l}{2\rho\tilde{c}_l} & \frac{-1}{2\rho\tilde{c}_l} & \frac{1}{2} & 0 \\ \frac{-u+(1-\alpha)\tilde{c}_l}{2\rho\tilde{c}_l} & \frac{1}{2\rho\tilde{c}_l} & \frac{1}{2} & 0 \\ \frac{\alpha}{\rho} & 0 & -1 & 0 \\ \frac{(\alpha-1)n\varphi}{\rho} & 0 & -n\varphi & 1 \end{bmatrix}. \tag{2.33}$$

The right and left eigenvectors (2.32) and (2.33) are used for the transformation from the conserved to the characteristic variables (i.e., $\mathbf{p} = \mathbf{L}\mathbf{q}$) or from the characteristic to the conserved variables (i.e., $\mathbf{q} = \mathbf{R}\mathbf{p}$).

2.4 Ensemble and volume averaging

Here, we consider the relation between ensemble and volume averages. The concept of volume averaging is to average field quantities within a control volume of mixtures with specific, instantaneous realizations of bubbly flows. For example, with the control volume $\mathcal{V}$ consisting of the liquid-phase and gas-phase volumes (i.e., $\mathcal{V} = \mathcal{V}_l + \mathcal{V}_g$), the dilute mixture density ρ can be defined as

$$\rho = \frac{\mathcal{V}_l \rho_l + \mathcal{V}_g \rho_g}{\mathcal{V}} \approx \frac{\mathcal{V}_l \rho_l}{\mathcal{V}}. \tag{2.34}$$

In order that the mixture within $\mathcal{V}$ be considered homogeneous and the averaged wave structure be well resolved, we need to choose an appropriate averaging volume and presuppose the scale separation (Nigmatulin, 1979; Prosperetti, 2001):

$$l = n^{-\frac{1}{3}} \ll \mathcal{V}^{\frac{1}{3}} \ll L, \tag{2.35}$$

where l is the mean bubble spacing and L is the (averaged) wavelength in the mixture. On the other hand, in ensemble averaging, we need not presuppose such a scale separation for deriving the averaged equations; this enables us to rigorously manipulate differentiation and integration. However, the scale separation assumption is ultimately still needed for the model closure.

Under the scale separation (2.35), the system can be considered homogeneous locally in space and the equality between ensemble and volume averages (or the ergodicity property) will thus hold (Batchelor, 1970; Biesheuvel & van Wijngaarden, 1984). In other words, if the wavelength of interest is large enough to satisfy the scale separation, the ensemble-averaged quantities will be equivalent to the volume averages. This observation is consistent with the fact that the ensemble-averaged equations derived in section 2.1.1 are essentially the same as van Wijngaarden's volume-averaged equations (except for the phase interaction term $\tilde{p}$).

It is also instructive to mention the analysis of d'Agostino & Brennen (1989). They considered the dynamics of a spherical (monodisperse) bubble cloud with radius R_c, under sinusoidal pressure

forcing at infinity, with the implicit assumption that the cloud dimension is far smaller than the wavelength associated with the pressure forcing (i.e., $R_c \ll L$). That is, their cloud size corresponds to the dimension of the control volume, $\mathcal{V}^{1/3}$, in the relation (2.35). A simple linear analysis reveals that the cloud has an infinite set of natural frequencies:

$$\omega_i = \omega_N \left[1 + \frac{12\beta}{(2i-1)^2\pi^2}\right]^{-\frac{1}{2}}, \tag{2.36}$$

where i is positive integers, ω_N is the natural frequency of individual bubble oscillations and β is termed the *cloud interaction parameter* defined as

$$\beta = \frac{\alpha_0(1-\alpha_0)R_c^2}{R_0^2}. \tag{2.37}$$

Note in particular that the lowest natural frequency, $\omega_1 = \omega_N(1+12\beta/\pi^2)^{-1/2}$, can be much smaller than the individual bubble frequency if β is far larger than unity (i.e., $\beta \gg 1$). In the limit of $\beta \to 0$, on the contrary, the cloud interaction effect is minimized and all the bubbles tend to oscillate freely with ω_N. Namely, this parameter governs the extent of bubble-bubble interactions through the averaged field.

With the aid of the cloud interaction parameter β, we revisit the scale separation problem. Now that $\mathcal{V}^{1/3}$ can be replaced with R_c, the scale separation (2.35) may read

$$\alpha_0^{\frac{1}{3}} \ll \beta \ll \left(\frac{L}{R_0^{\mathrm{ref}}}\right)^2 \alpha_0. \tag{2.38}$$

Provided that there exists the value of β that satisfies the above relation, we can suitably choose an averaging volume in instantaneous realizations of bubbly flows. In this case, the ensemble and volume averages will again be equivalent. To meet the scale separation (2.38), we say that the right-hand side, $(L/R_0^{\mathrm{ref}})^2\alpha_0$, needs to be S times larger than the left-hand side, $\alpha_0^{1/3}$; namely

$$L = S^{\frac{1}{2}}\alpha_0^{-\frac{1}{3}}R_0^{\mathrm{ref}}. \tag{2.39}$$

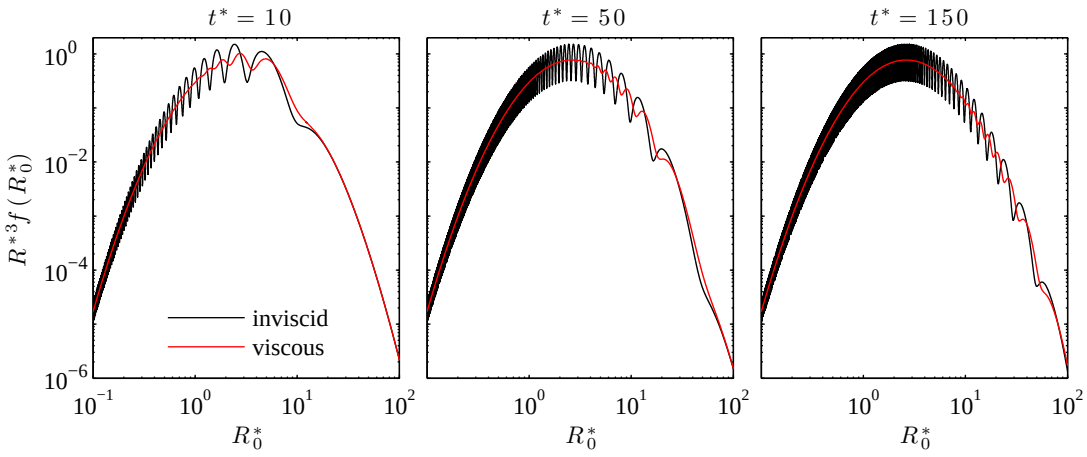

Figure 2.2: Integrands of the third moment μ_3 for the inviscid Rayleigh–Plesset equation and the viscous Gilmore equation. The equilibrium bubble size is assumed lognormally distributed with $R_0^{\text{ref}} = 10$ μm and $\sigma = 0.7$.

If we take $S = 10^2$ and $\alpha_0 = 10^{-3}$ as an example, the above relation yields $L = 100R_0^{\text{ref}}$. This suggests that wavelengths shorter than this bound will not be accurately captured using continuum models.

2.5 One-way-coupled flow computations

Before proceeding to two-way-coupled flow computations, we consider the evolution of moments (2.7) in the one-way-coupling case where any bubble/bubble interactions are neglected (in the limit of $\beta \to 0$). Specifically, our interest is to predict the moments of bubble radius with respect to the lognormal distribution (2.10):

$$\mu_i(\mathbf{x}, t) = \int_0^\infty R^i(\mathbf{x}, t; R_0) f(R_0) dR_0, \tag{2.40}$$

where i is integers. For example, the third moment $\mu_3(\mathbf{x}, t)$ represents the mean bubble volume, which is proportional to the void fraction (2.8). In the volume-averaging sense, $\mu_3(\mathbf{x}, t)$ can be interpreted as the mean bubble volume within an averaging volume $\mathcal{V}$ centered at $\mathbf{x}$.

We now consider the problem that air/vapor bubbles in water are initialized with lognormal

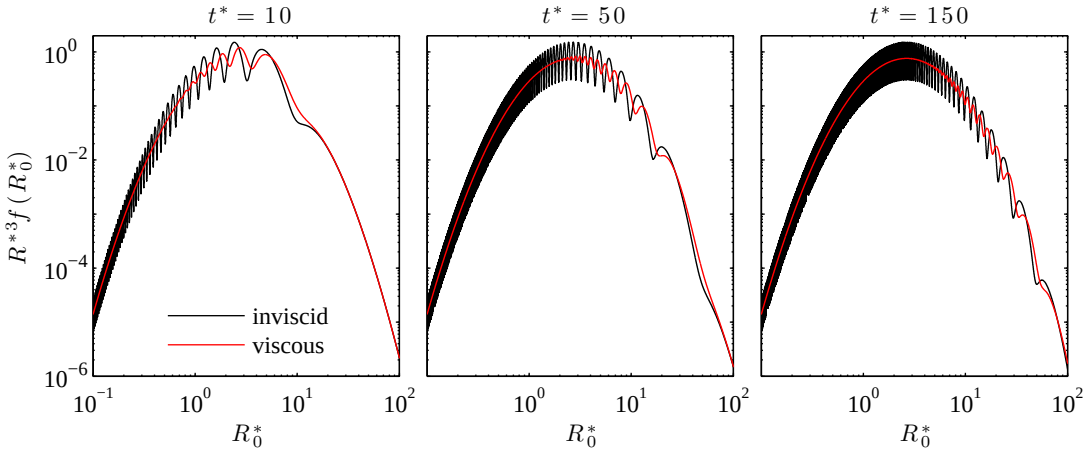

Figure 2.3: As figure 2.2, but with $R_0^{\mathrm{ref}} = 50$ μm.

distributions (2.10) at standard temperature and pressure (STP; 20 °C and 101 kPa) and then forced according to a step-wise (farfield) pressure change from p_{l0} to $2p_{l0}$ at $t = 0$. This may be a simple example to shock propagation in bubbly flows. The bubble dynamics are computed by solving the inviscid Rayleigh–Plesset equation (with isothermal air) and the Gilmore equations including acoustic, viscous and thermal damping as described in section 2.2. The time integration is handled using a Runge–Kutta scheme with adaptive step-size control (Press *et al.*, 1994). The physical properties are taken from Lide (2006).

Figures 2.2 and 2.3 show the integrands of the third moment μ_3, at three different times, for the lognormal distribution with $\sigma = 0.7$, and $R_0^{\mathrm{ref}} = 10$ μm and 50 μm, respectively. Time is normalized by the time scale, $R_0^{\mathrm{ref}}\sqrt{\rho_{l0}/p_{l0}}$, as in appendix B; t^* denotes the normalized time. Note that the integrands are initially ($t^* = 0$) very smooth with the lognormal distribution of equilibrium bubble sizes. For the inviscid case, the integrands become more oscillatory as the bubble oscillations evolve, because the bubbles with different equilibrium sizes oscillate with different frequencies; eventually, the different-sized bubbles oscillate totally out of phase. On the other hand, the bubble-dynamic dissipation for small bubbles is found to be effective enough to damp down the dynamics. As a result, the integrands for the viscous case are less oscillatory. Since the damping is more effective for smaller bubbles (Plesset & Prosperetti, 1977; Brennen, 1995), the case with $R_0^{\mathrm{ref}} = 10$ μm in figure

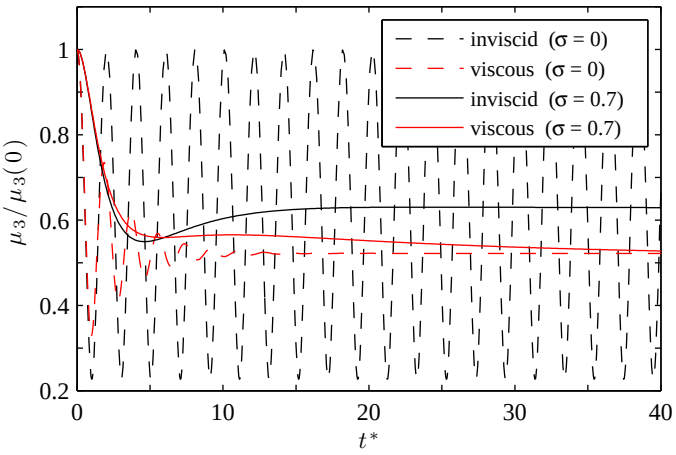

Figure 2.4: Evolution of μ_3 for the inviscid Rayleigh–Plesset equation and the viscous Gilmore equation. The equilibrium bubble size is assumed lognormally distributed with $R_0^{\text{ref}} = 10$ μm.

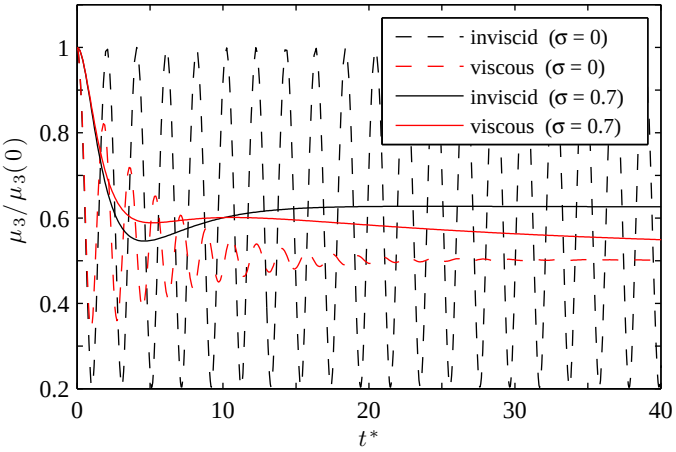

Figure 2.5: As figure 2.4, but with $R_0^{\text{ref}} = 50$ μm.

2.2 shows the smoother integrands.

Figures 2.4 and 2.5 show the evolution of the third moment $\mu_3(t^*)$ for the cases of $R_0^{\text{ref}} = 10$ μm and 50 μm, respectively. For reference, the monodisperse cases ($\sigma = 0$), for which no quadrature is needed, are also plotted. It is interesting to note that the inviscid bubble oscillations in the polydisperse case achieve a time-invariant value of the moment even though all the bubbles keep oscillating without any damping. We say that the bubble oscillations reach a *stationary statistical equilibrium* due to phase cancellations among bubbles with different sizes as presented in figures 2.2 and 2.3. The existence of the statistical equilibrium is mathematically proven by Colonius

et al. (2008). We can say, in the volume-averaging sense, that at the statistical equilibrium, the polydisperse bubble cloud does not oscillate in volume, regardless of oscillations of the individual bubbles. Thus, the phase cancellations (that appear only in the polydisperse case) can be regarded as an *apparent* damping of the average mixture dynamics (Smereka, 2002; Colonius *et al.*, 2008). It is also seen in the polydisperse case that the statistical equilibrium is rapidly achieved whereas the moment with single-bubble-dynamic damping shows a gradual decay to the equilibrium state with $2p_{l0}$. Therefore, if the equilibrium bubble sizes are broadly distributed, the effect of polydispersity can dominate over the bubble-dynamic damping.

2.6 Summary

This chapter provided the complete set of the governing equations for a continuum model of bubbly flows. The ensemble-averaged equations incorporating a distribution of equilibrium bubble sizes were obtained to described the average mixture dynamics. The single-bubble-dynamic model that includes the effects of thermal, viscous and acoustic damping was also introduced to close the continuum bubbly flow model. The system is written in a conservation form for robust shock computations. We examined the relation between ensemble and volume averaging based on the ergodic hypothesis and confirmed that the volume averages will be equivalent to the ensemble-averaged quantities if one appropriately chooses averaging volume under the scale separation assumption. One-way-coupling flow computations suggested that the different-sized bubbles oscillate with different frequencies and the phase cancellations can be regarded as an apparent damping of the averaged dynamics of polydisperse bubbly flows.

Chapter 3

Numerical method

This chapter presents a numerical method designed to conduct efficient and robust shock computations for polydisperse bubbly flows. The system is written in a conservation form and is discretized using a finite-volume method with an approximate Riemann solver. Time marching, including a time-step splitting technique that handles the stiffness, is introduced. Implementation of boundary conditions is also discussed. Finally, the method is used to solve some test problems for verification purposes.

3.1 Spatial discretization

3.1.1 Finite-volume reconstruction

Since shocks in bubbly flows often have oscillatory structures that result from bubble dynamics, we favor the properties of high-order accurate resolution in complex smooth structures as well as shock capturing. Herein, we choose a finite-volume (FV) weighted essentially non-oscillatory (WENO) scheme (Liu *et al.*, 1994) that contains such properties in addition to robustness.

The system (2.26) is discretized in FV fashion. Given a computational cell $[x_{i-1/2}, x_{i+1/2}]$ where i denotes the grid index, the cell-averaged conserved variables are defined as

$$\bar{\mathbf{q}}_i(t) = \frac{1}{\Delta x_i} \int_{x_{i-1/2}}^{x_{i+1/2}} \mathbf{q}(x', t) dx', \quad \Delta x_i = x_{i+1/2} - x_{i-1/2}, \tag{3.1}$$

so that $\bar{\mathbf{q}}_i$ approximates $\mathbf{q}$ at the cell center $x_i = (x_{i-1/2} + x_{i+1/2})/2$. With the aid of equation (3.1), the system is written in a semi-discrete form:

$$\frac{d\bar{\mathbf{q}}_i}{dt} = -\frac{\mathbf{f}_{i+1/2} - \mathbf{f}_{i-1/2}}{\Delta x_i} + \frac{\mathbf{f}^s_{i+1/2} - \mathbf{f}^s_{i-1/2}}{\Delta x_i} + \bar{\mathbf{s}}_i. \tag{3.2}$$

In FV methods, $\bar{\mathbf{q}}_i$ is reconstructed at each cell edge, and the numerical flux $\mathbf{f}_{i+1/2}$ is computed by solving a Riemann problem with the left and right states $(\mathbf{q}^{\mathrm{L}}_{i+1/2}, \mathbf{q}^{\mathrm{R}}_{i+1/2})$.

In order to resolve the complex wave structures, we choose the fifth-order FV-WENO reconstruction (Liu *et al.*, 1994; Shu, 1997) with monotonicity preserving bounds (Balsara & Shu, 2000). ENO reconstruction (Harten *et al.*, 1987) is based on adaptive stencils in the sense that interpolation across discontinuities is automatically avoided. WENO schemes use a convex combination of all the ENO candidate stencils for more efficient and accurate computations. To guarantee essentially non-oscillatory solutions, it is safe to implement the WENO reconstruction in characteristic space even though a local characteristic decomposition is computationally expensive (Qiu & Shu, 2002).

3.1.2 HLLC approximate Riemann solver

To compute the numerical flux $\mathbf{f}_{i+1/2}$, *approximate* Riemann solvers are conventionally used to solve the Riemann problem that results from the reconstruction at each cell edge (Toro, 1999). We choose the HLLC Riemann solver (Toro *et al.*, 1994; Toro, 1999) that automatically satisfies the entropy condition. The HLLC solver restores the contact waves that are ignored in the HLL solver (Harten *et al.*, 1983), and gives better resolutions of the contact discontinuities.

If the left and right states $(\mathbf{q}^{\mathrm{L}}, \mathbf{q}^{\mathrm{R}})$ are imposed at $x = 0$ and $t = 0$, the HLLC Riemann solution is given by

$$\mathbf{q}^{\mathrm{HLLC}}(x,t) = \begin{cases} \mathbf{q}^{\mathrm{L}} & \text{if } x/t \le s^{\mathrm{L}}, \\ \mathbf{q}^{*\mathrm{L}} & \text{if } s^{\mathrm{L}} \le x/t \le s^{*}, \\ \mathbf{q}^{*\mathrm{R}} & \text{if } s^{*} \le x/t \le s^{\mathrm{R}}, \\ \mathbf{q}^{\mathrm{R}} & \text{if } x/t \ge s^{\mathrm{R}}. \end{cases} \tag{3.3}$$

The Rankine–Hugoniot conditions with the constraints across the contact waves (constructed for the hyperbolic part) yield the expression for the intermediate (star) state:

$$\mathbf{q}^{*\mathrm{K}} = \frac{s^{\mathrm{K}} - u^{\mathrm{K}}}{s^{\mathrm{K}} - s^*} \begin{Bmatrix} \rho^{\mathrm{K}} \\ \rho^{\mathrm{K}} s^* \\ \alpha^{\mathrm{K}} \\ (n\varphi)^{\mathrm{K}} \end{Bmatrix}, \tag{3.4}$$

where K = L or R. It follows from Einfeldt *et al.* (1991) that

$$s^{\mathrm{L}} = \min\left((u - \tilde{c}_l)^{\mathrm{Roe}}, u^{\mathrm{L}} - \tilde{c}_l^{\mathrm{L}}\right), \quad s^{\mathrm{R}} = \max\left((u + \tilde{c}_l)^{\mathrm{Roe}}, u^{\mathrm{R}} + \tilde{c}_l^{\mathrm{R}}\right), \tag{3.5}$$

where the superscript "Roe" stands for the Roe averages (Roe, 1981). The momentum conservation yields the expression for the intermediate wave speed (Batten *et al.*, 1997):

$$s^* = \frac{p_l^{\mathrm{R}} - p_l^{\mathrm{L}} + \rho^{\mathrm{L}} u^{\mathrm{L}}(s^{\mathrm{L}} - u^{\mathrm{L}}) - \rho^{\mathrm{R}} u^{\mathrm{R}}(s^{\mathrm{R}} - u^{\mathrm{R}})}{\rho^{\mathrm{L}}(s^{\mathrm{L}} - u^{\mathrm{L}}) - \rho^{\mathrm{R}}(s^{\mathrm{R}} - u^{\mathrm{R}})}. \tag{3.6}$$

Using the HLLC solution (3.3), the HLLC fluxes are computed as

$$\mathbf{f}^{\mathrm{HLLC}} = \mathbf{f}\left(\mathbf{q}^{\mathrm{HLLC}}\right), \quad \mathbf{f}^{s\,\mathrm{HLLC}} = \mathbf{f}^s\left(\mathbf{q}^{\mathrm{HLLC}}\right). \tag{3.7}$$

It is instructive to note that the (one-dimensional) divergence of the velocity field is approximated by

$$\left.\frac{\partial u}{\partial x}\right|_i \approx \frac{u_{i+1/2} - u_{i-1/2}}{\Delta x_i}, \tag{3.8}$$

where the cell-edge velocity is computed from the HLLC solution (3.3). The divergence $\nabla \cdot \mathbf{u}$ is needed for evaluating the rate of change of the liquid pressure (B.12).

3.2 Time marching

3.2.1 Unsplit time integration

Given the HLLC fluxes and the sources, the system written in a semi-discrete form can be integrated in time. The simplest way is to employ explicit methods in which a single time step Δt is used to resolve both the convective and the bubble-dynamic terms. A third-order TVD Runge–Kutta scheme (Shu & Osher, 1988; Gottlieb & Shu, 1998) is often used for stable shock computations. The choice of Δt depends on the constraint on the dimensionless Courant–Friedrichs–Lewy (CFL) number (LeVeque, 1992; Toro, 1999; LeVeque, 2002), which is defined as the ratio of the physical wave speed to the grid speed $\Delta x_i/\Delta t$. For one-dimensional computations, the maximum CFL number may be defined as

$$\mathrm{CFL} = \Delta t \max_i \left\{ \frac{|u_i| + (\tilde{c}_l)_i}{\Delta x_i} \right\}. \tag{3.9}$$

For hyperbolic systems, a linear analysis shows that the CFL constraint is given by $0 < \mathrm{CFL} \leq 1$. However, the system (2.26) is not rigorously hyperbolic, and the bubble dynamics would alter the stability condition.

3.2.2 Time-step splitting

In cases of strong shocks and cavitation, the bubble-dynamic sources are very stiff. As a result, the unsplit time integration requires very small CFL number for stable bubble-dynamic computations. This necessitates applying a splitting technique to solve the averaged fluid dynamics and the bubble dynamics separately. One benefit of splitting schemes is that a well-established, tailor-made numerical technique can be applied to each subproblem. For example, stiff ordinary differential equation (ODE) solvers or implicit methods are suitable to handle the stiffness. However, we need to be cautious about the splitting errors.

Consider the initial value problem (2.26) with initial condition $\mathbf{q}(x, t^n) = \mathbf{q}^n$ where the superscript n refers to the time discretization. We need to find $\mathbf{q}(x, t^{n+1}) = \mathbf{q}^{n+1}$ by integrating the

system (2.26) over the time step $\Delta t = t^{n+1} - t^n$. First, we integrate the fluid-dynamic part:

$$\mathbf{q}^*_t + \mathbf{f}(\mathbf{q}^*)_x = \mathbf{f}^s(\mathbf{q}^*)_x, \tag{3.10}$$

with the initial condition $\mathbf{q}^n$ over the splitting time step Δt (which satisfies the CFL constraint), and then obtain the intermediate value $\mathbf{q}^*(x, t^{n+1})$. Next, we integrate the bubble-dynamic part:

$$\mathbf{q}^{**}_t = \mathbf{s}(\mathbf{q}^{**}), \tag{3.11}$$

where $\mathbf{q}^*(x, t^{n+1})$ is imposed as the initial condition at time t^n. During the source term integration from t^n to t^{n+1}, ρ, u and n are unchanged. In addition, it may be reasonable to assume that the rate of change of the liquid pressure, $\dot{p}_l$, is constant during the integration of equation (3.11) because the averaged fluid-dynamic time scale is typically much larger than the bubble-dynamic time scale. The solution of equation (3.11), $\mathbf{q}^{**}(x, t^{n+1})$, is therefore regarded as an approximation to the numerical solution $\mathbf{q}^{n+1}$ of the unsplit problem (2.26).

We now write the splitting scheme consisting of equations (3.10) and (3.11) as

$$\mathbf{q}^{n+1} = S_2^{(\Delta t)} S_1^{(\Delta t)} \mathbf{q}^n, \tag{3.12}$$

where $S_1^{(\Delta t)}$ and $S_2^{(\Delta t)}$ are the solution operators for the convective part (3.10) and for the bubble-dynamic part (3.11), respectively, taken over Δt. This procedure is called the Godunov splitting and is only first-order accurate (Toro, 1999; LeVeque, 2002). Instead, the second-order Strang splitting (Strang, 1968) can be used:

$$\mathbf{q}^{n+1} = S_2^{(\Delta t/2)} S_1^{(\Delta t)} S_2^{(\Delta t/2)} \mathbf{q}^n, \tag{3.13}$$

where the operators are at least second-order accurate. It is pointed out in Sportisse (2000) that if the splitting time step Δt is much larger than time scales of stiff sources, a classical analysis of the splitting error using $\Delta t \to 0$ no longer holds. A singular perturbation theory revealed that the

Strang splitting (3.13) is only first-order accurate in such stiff cases.

3.3 Boundary conditions

3.3.1 Reflective boundaries

Reflective boundary conditions are used to model an impermeable solid wall that touches inviscid flows. Now suppose that a wall surface is initially located at $x_{1/2}$, the end of the computational domain ($x \geq x_{1/2}$), but can move. If the displacement is sufficiently small, the wall motion can be incorporated at the fixed point $x_{1/2}$ in an Eulerian frame (Toro, 1999; LeVeque, 2002). This situation is handled by solving a Riemann problem at $x_{1/2}$ with the following fictitious conditions:

$$\rho_0 = \rho_1, \quad u_0 = 2u_w - u_1, \quad (p_l)_0 = (p_l)_1, \quad (n\varphi)_0 = (n\varphi)_1, \tag{3.14}$$

where u_w is the wall velocity and the quantities with the subscript 0 are defined at the fictitious computational cell, outside the domain, that is centered at $x_0 = x_{1/2} - \Delta x_1/2$. Note that the conditions (3.14) with $u_w = 0$ represent the case of stationary walls. To maintain the formal order of accuracy of the reconstruction, we can add extra fictitious cells further away from the boundary (Dadone & Grossman, 1994).

3.3.2 Nonreflective boundaries

The treatment of nonreflective boundaries is based on the work of Thompson (1987). His idea is to evaluate only outgoing waves from a finite computational domain at the boundaries. Since the outgoing waves depend only on the information within the boundaries, the waves are evaluated using one-sided, upwind differencing. It should be noted that the fifth-order accuracy of the WENO reconstruction cannot be retained near the nonreflective boundaries since the information outside the domain is missing; thus, the lower-order accurate scheme needs to be used near the boundaries (Johnsen, 2007).

For computations of bubbly flows with finite void fractions, the sonic speed evaluation at the boundaries is intractable because the waves are dispersive. For shock computations in chapter 4, the sonic speed of mixtures in the quasistatic limit (Brennen, 1995), rather than $\tilde{c}_l$ in equation (2.31), is used for the sonic speed evaluation:

$$c = \sqrt{\frac{\gamma(p_l + B)}{\rho} \frac{\kappa p_l}{\alpha\gamma(p_l + B) + (1 - \alpha)\kappa p_l}}. \tag{3.15}$$

However, in this manner, high-frequency waves can be reflected back into the computational domain. The domain is thus set to be large enough that the spurious waves do not contaminate the solution of interest or the waves are effectively attenuated (due to bubble-dynamic damping) before reaching the boundaries.

3.4 Verification

In the following test problems, we implement the method and investigate its performance. In section 3.4.1, linear wave propagation in a pure liquid is computed to confirm the numerical convergence. In section 3.4.2, dispersive linear waves in a bubbly liquid are solved and their computed phase velocity and attenuation are compared to the theoretical predictions. The continuum model limitation is revisited, and the cloud effect in two-way-coupled flow computations is also examined. Finally, in section 3.4.3, cloud cavitation caused by valve closure in a pipe flow is considered and the performance of the time-step splitting schemes is quantified.

As mentioned in section 3.1, the fifth-order monotonicity-preserving FV-WENO reconstruction is implemented in the characteristic space, and the HLLC Riemann solver manipulates the numerical flux. The computational grid is uniform with $\Delta x_i = \Delta x$ (for all i). Runge–Kutta schemes with uniform time step Δt are used to march the entire system (for unsplit cases) or the convective terms (for cases with time-step splitting). Besides, the transport properties of bubble contents are assumed constant and taken from Lide (2006).

Δx	L_1 error	L_1 order	L_∞ error	L_∞ order
1/20	1.31×10^{-7}		6.55×10^{-7}	
1/40	1.47×10^{-8}	3.15	7.43×10^{-8}	3.14
1/80	4.83×10^{-10}	4.93	2.69×10^{-9}	4.79
1/160	1.47×10^{-11}	5.04	8.68×10^{-11}	4.95
1/320	4.65×10^{-13}	4.98	2.80×10^{-12}	4.95

Table 3.1: Density convergence study for linear wave propagation in pure water. The errors are normalized by the reference water density ρ_{l0}.

3.4.1 Convergence analysis

In order to confirm the accuracy of the WENO reconstruction, (non-dispersive) linear waves in a pure water with $\alpha_0 = 0$ are considered. We impose the following initial condition in $x \in [-0.5, 0.5]$:

$$p_l(x) = p_{l0}\left[1 + \epsilon \exp\left(-\frac{x^2}{h^2}\right)\right], \quad u_l(x) = 0. \tag{3.16}$$

Provided that ϵ is sufficiently small, nonlinearity in the governing equations is effectively eliminated, and the perturbation would propagate with the sonic speed of water, c_{l0}, at one atmosphere p_{l0}. Note that the pressure perturbations (in water) up to several hundred atmospheres can be regarded as linear waves (Thompson, 1972). If the boundaries (at $x = -0.5$ and 0.5) are periodic, the solution after one period would recover the initial conditions (3.16). The time integration is handled using a fifth-order Runge–Kutta scheme with CFL $\approx c_{l0}\Delta t/\Delta x = 0.1$.

Table 3.1 summarizes the convergence analysis in which the error norm and the order of accuracy are presented. The initial conditions (3.16) with $\epsilon = 0.1$ and $h = 0.1$ are taken as the reference solution to define the L_1 and L_∞ errors in the liquid density after one period. It is confirmed that the accuracy asymptotes to the fifth order as the number of the computational cells increases.

3.4.2 Linear waves in a bubbly liquid

Consider one-dimensional linear wave propagation in an air/water mixture of $\alpha_0 = 0.001$ at STP. Since the vapor pressure of water is much smaller than the ambient pressure, the vapor flux term in equation (2.17) is omitted. The initial conditions (3.16) with $\epsilon = 10^{-4}$ and $h = 4R_0^{\mathrm{ref}}$ are

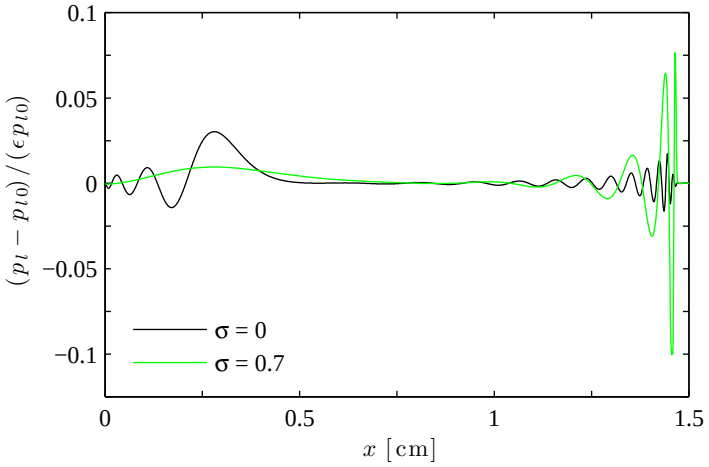

Figure 3.1: Liquid pressure distribution at $t = 10$ μs for linear wave propagation in an air/water mixture of $\alpha_0 = 0.001$ and $R_0^{\mathrm{ref}} = 10$ μm at STP.

initially ($t = 0$) imposed to see wave dispersion. It is assumed that all the bubbles are initially in equilibrium with the perturbed liquid pressure. It is also assumed that the equilibrium bubble sizes are lognormally distributed with $R_0^{\mathrm{ref}} = 10$ μm and σ. The time marching is handled using a third-order TVD Runge–Kutta scheme (Shu & Osher, 1988; Gottlieb & Shu, 1998) with CFL $\approx \tilde{c}_{l0}\Delta t/\Delta x = 0.1$ and $\Delta x = R_0^{\mathrm{ref}}$. Noting that the isothermal natural period for the bubble size R_0^{ref} is 3.44 μs and is approximately $5000\Delta t$, this time step will be small enough to resolve the bubble dynamics. For the polydisperse case, the moment (2.7) is evaluated using Simpson's rule with 101 quadrature points.

Figure 3.1 shows the averaged liquid pressure distribution at $t = 10$ μs for the linear wave propagation in the monodisperse mixture ($\sigma = 0$) or polydisperse mixture ($\sigma = 0.7$). As in the experiment of Kuznetsov *et al.* (1978), we observe wave dispersion due to bubble dynamics. Specifically, the high-wavenumber waves propagate essentially with the sonic speed of water alone, c_{l0}, but the waves with low wavenumbers propagate more slowly than c_{l0}. Note that the bubble size distribution with $\sigma = 0.7$ smoothes out the oscillatory structure in the low-frequency signal.

To verify the present model, the phase velocity and attenuation of the linear waves are computed from the numerical experiment, and compared to the acoustic theory (Ando *et al.*, 2009) that can be derived by linearizing the volume-averaged equations of van Wijngaarden (1968, 1972). The

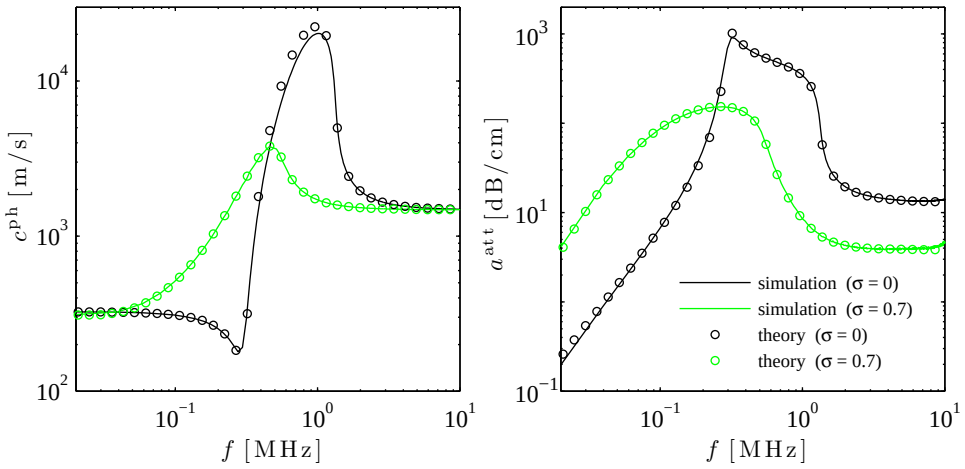

Figure 3.2: Phase velocity (left) and attenuation (right) of the linear waves in the air/water mixture. The isothermal natural frequency for $R_0^{\mathrm{ref}} = 10$ μm is 0.291 MHz.

computation of the phase velocity and attenuation is explained in appendix C. Figure 3.2 compares the computed phase velocity and attenuation to the theoretical predictions. Quantitative agreement in a wide range of frequency totally verifies the present method. It also follows from the phase velocity plot that the waves with low and high wavenumbers in figure 3.1 correspond to the low-frequency (quasistatic) and high-frequency (ultrasonic) regimes, respectively. The slight deviations from the theory result from the reduced-order model of Preston *et al.* (2007) for evaluating heat conduction at the bubble wall since Preston's model is never exact for finite values of the Peclet number; nevertheless, this enables us to avoid solving the detailed conservation equations inside the bubble and therefore dramatically reduces the computational effort.

We now revisit the scale separation discussion (in section 2.4) to examine the continuum assumption. In this example ($\alpha_0 = 0.001$, $R_0^{\mathrm{ref}} = 10$ μm), the relation (2.38) now reads

$$0.1 \ll \beta \ll 0.001 \left(\frac{L}{R_0^{\mathrm{ref}}} \right)^2 . \tag{3.17}$$

For the right-hand side to be two orders of magnitude larger than 0.1, we need large wavelengths to satisfy $L/R_0^{\mathrm{ref}} \gtrsim 100$. The low-wavenumber waves in figure 3.1 reasonably meet this constraint; thus, we can suitably choose an averaging control volume with $\beta \approx 1$ to define volume averages,

which will be equivalent to ensemble averages. However, the high-wavenumber waves in figure 3.1 are larger than the bubble dimensions but comparable to the mean bubble spacing (≈ 0.16 mm for $\sigma = 0$); the scale separation (3.17) does not hold and the continuum approach itself is invalid. In summary, the continuum model is applicable to low-frequency waves in the quasistatic regime but is less accurate in ultrasonic wave solutions.

Finally, we consider the corresponding one-way-coupled problem in order to quantify the two-way-coupling effect in the polydisperse case. Provided that the cloud interaction is minimized (in the limit of $\beta \to 0$), the two-way-coupled problem at $x = 0$ may reduce to the one-way-coupling case in which individual dynamics are excited by impulsive pressure forcing and all the bubbles are oscillating independently with their natural frequencies $\omega_N(R_0)$. Our concern is to predict the second moment of the perturbed bubble radius with respect to the lognormal distribution (2.10) with $\sigma = 0.7$,

$$\mu_2'(t) = \int_0^\infty \left[R(t; R_0) - R_0\right]^2 f(R_0) dR_0, \tag{3.18}$$

whereas the first moment μ_1', for the case of linearized dynamics, vanishes at the statistical equilibrium (Colonius *et al.*, 2008). For the one-way-coupled flow computation, the bubble dynamics are computed by integrating the Gilmore equation with the physical dissipation as in section 2.5, and the farfield pressure impulse is modeled by

$$p_l(t) = p_{l0}\left[1 + \epsilon \exp\left(-\frac{t^2}{T_f^2}\right)\right], \tag{3.19}$$

where T_f is chosen to be small enough to ensure that the dynamics are independent of T_f.

Figures 3.3 and 3.4 present the integrands of μ_2' at $t = 2$ μs and $t = 10$ μs, respectively. For the two-way-coupling case, we plot the integrands at $x = 0$ where the narrow pressure perturbation is initially imposed. In the inviscid and one-way-coupling case, the bubbles of any size keep oscillating with $\omega_N(R_0)$ and their oscillations tend to be out of phase as they evolve; in the viscous cases, on the contrary, oscillations of the small bubbles are damped down before the integrands become very oscillatory as in the inviscid case, but there still appear phase cancellations among the different-sized

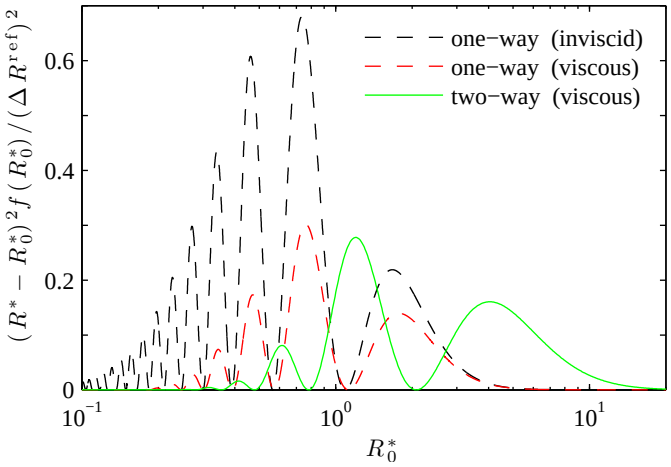

Figure 3.3: Integrands of the second moment μ_2' at $t = 2$ μs. The maximum perturbation, ΔR^{ref}, in bubble radius for $R_0 = R_0^{\mathrm{ref}}$ is used to normalize the integrands.

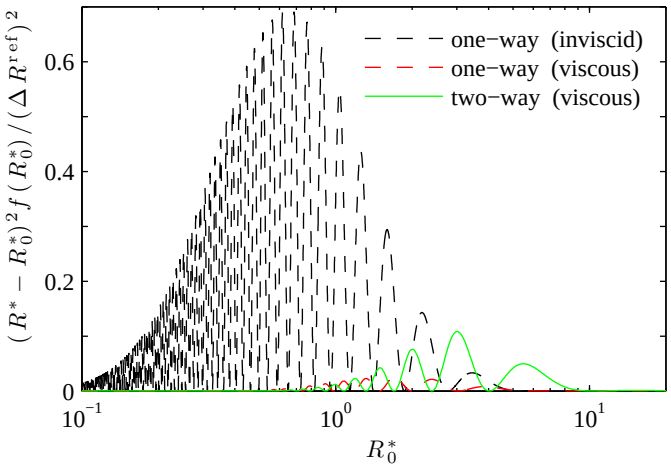

Figure 3.4: As figure 3.3, but at $t = 10$ μs.

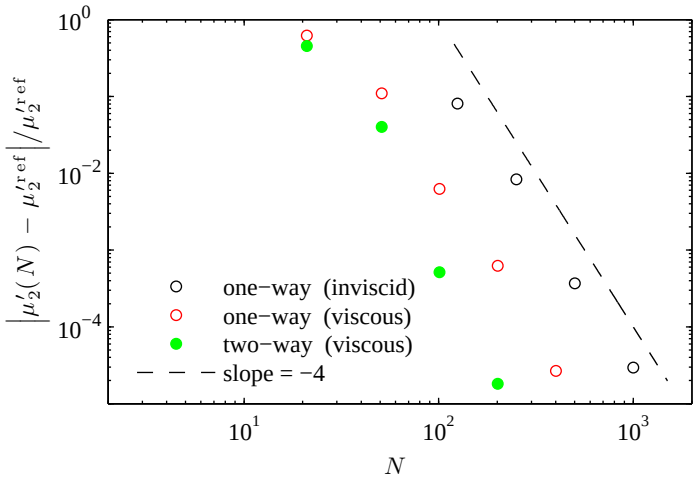

Figure 3.5: Quadrature errors for μ_2' at $t = 10$ μs.

bubbles of larger sizes. These phase cancellations can be interpreted as an apparent damping of low-frequency wave propagation and augment the attenuation as seen in figure 3.2 (Ando *et al.*, 2009). It should be noticed that the two-way-coupling (or cloud) effect lowers the oscillation frequencies (as discussed in section 2.4) so that the integrand becomes less oscillatory. In other words, the bubble oscillations in the two-way-coupled flow more slowly reach the statistical equilibrium state in which the different-sized bubbles oscillate totally out of phase.

The quadrature errors in computing μ_2' at $t = 10$ μs are defined by comparing the values of the integral using fourth-order-accurate Simpson's rule (with varying the number of quadrature points N) to their values using a far larger number, and plotted in figure 3.5. This plot suggests that the moment in the two-way-coupled viscous flow computation can be predicted with fewer quadrature points than in the one-way-coupling cases. This is consistent with the observation in figures 3.3 and 3.4 that the viscous and cloud effects make the integrand less oscillatory. Furthermore, in the two-way-coupling case, 0.1-percent accuracy is achieved at $N = 101$. Hence, the solution for the polydisperse case in figure 3.1 reasonably converges with respect to the integral over the bubble size distribution.

Also in polydisperse flow computations in chapters 4 and 5, Simpson's rule is employed to evaluate the moments with respect to the lognormal distribution of equilibrium bubble sizes; 401 quadrature

points are used for bubble screen computations in section 4.5, but otherwise 101 quadrature points are used. These numbers of quadrature points are enough to obtain well converged solutions. However, in practical calculations where 0.1-percent accuracy is too demanding, one can further decrease the number.

3.4.3 Pipe flow with valve closure

Consider a water-hammer event in which a valve closes suddenly in pipe flows and the resulting rarefaction waves that propagate downstream cause cloud cavitation. Because the system can be very stiff due to violent collapse of cavitation bubbles, we favor solving the (averaged) fluid dynamics and the bubble dynamics separately for efficient time integration. We now solve a one-dimensional water-filled pipe flow with constant velocity ($u_0 = 0.5$ m/s) and with air nuclei conditions ($\alpha_0 = 10^{-6}$, $R_0^{\mathrm{ref}} = 50$ μm, $\sigma = 0$) at STP, and assume sudden closure of a valve at $x = 0$ and $t = 0$. The reflective boundary conditions (3.14) with $u_w = 0$ are imposed at $x = 0$ to replicate the valve closure. The Godunov (3.12) and Strang (3.13) splitting schemes are implemented to integrate the entire system in time; the third-order TVD Runge–Kutta scheme is used to compute the convective terms and the Runge–Kutta scheme with adaptive step-size control (Press *et al.*, 1994) resolves the bubble-dynamic sources. The reference solution is taken as that obtained by the unsplit scheme using the third-order TVD Runge–Kutta scheme with CFL = 0.01 and $\Delta x = 5R_0^{\mathrm{ref}}$. To examine the spatial convergence, the solution on the finer grid with $\Delta x = R_0^{\mathrm{ref}}$ is also obtained.

The spatial evolution of the averaged pressure and the void fraction at $t = 0.16$ ms for the unsplit cases is presented in figure 3.6. Whereas the non-cavitating solution remains self-similar, the solutions with bubble-dynamic computations show cloud cavitation behind the tension wave front. The cloud collapse that may be identified as local minima of the void fraction is found to be well captured on the coarser grid with $\Delta x = 5R_0^{\mathrm{ref}}$. In figure 3.7, the splitting solutions with $\Delta x = 5R_0^{\mathrm{ref}}$ are compared to the reference solution in the void fraction in figure 3.6. With the fixed CFL number, the Strang solution shows better agreement than the Godunov solution; the Strang solution with CFL = 0.1 visually coincides with the unsplit solution.

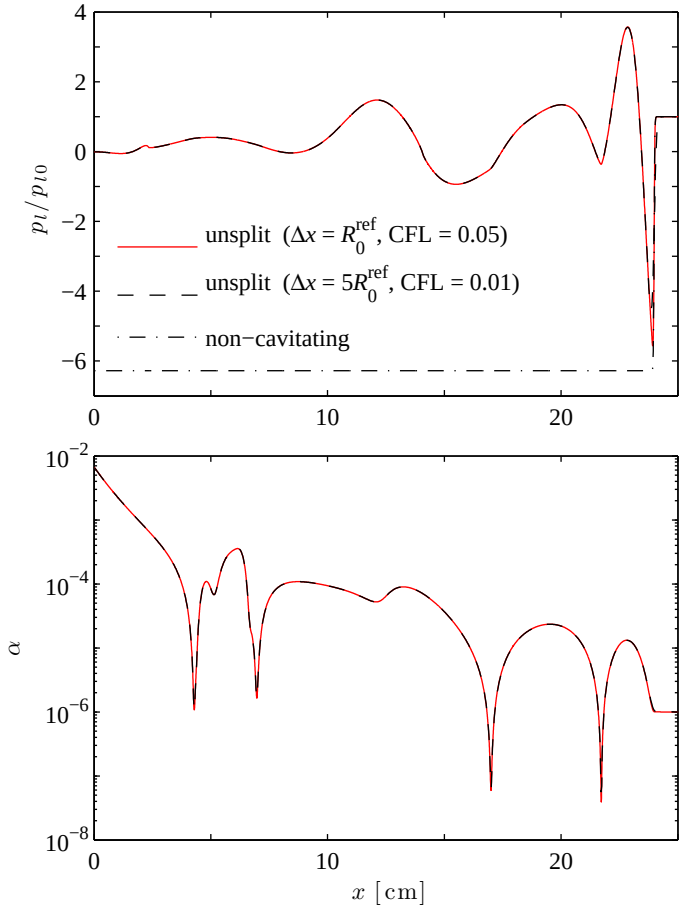

Figure 3.6: Spatial evolution of the averaged liquid pressure (top) and void fraction (bottom) at $t = 0.16$ ms for the one-dimensional cavitation tube problem.

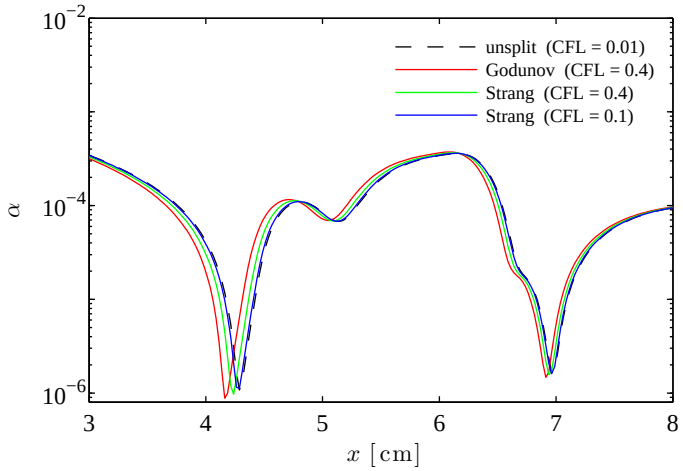

Figure 3.7: Comparison of the splitting solutions to the reference solution in the void fraction distribution in figure 3.6. All the solutions are based on the same grid resolution with $\Delta x = 5R_0^{\text{ref}}$.

CFL	L_1 error	L_1 order	L_∞ error	L_∞ order
0.4	1.14×10^{-5}		2.89×10^{-4}	
0.2	5.63×10^{-6}	1.02	1.42×10^{-4}	1.02
0.1	2.80×10^{-6}	1.01	7.05×10^{-5}	1.01
0.05	1.39×10^{-6}	1.00	3.51×10^{-5}	1.01

Table 3.2: Density convergence study for the Godunov splitting in the cavitation tube problem. The errors are defined on the domain shown in figure 3.6 and normalized by water density ρ_{l0}.

CFL	L_1 error	L_1 order	L_∞ error	L_∞ order
0.4	5.65×10^{-6}		1.41×10^{-4}	
0.2	2.80×10^{-6}	1.01	7.14×10^{-5}	0.987
0.1	1.40×10^{-6}	1.01	3.58×10^{-5}	0.996
0.05	6.97×10^{-7}	1.00	1.79×10^{-5}	0.998

Table 3.3: As table 3.2, but for the Strang splitting.

Tables 3.2 and 3.3 summarize the convergence analysis (with fixed Δx but with varying Δt) for the Godunov and Strang splitting schemes, respectively. The error norm and the order of accuracy are computed from the mixture density at $t = 0.16$ ms. Note that the global errors consist of temporal and spatial errors. Since the void fraction field involves nonsmooth spatial variation as observed in figure 3.6, the global errors will be contaminated by local spatial errors that decay as Δx, not Δx^5. It turns out that both splitting schemes are at most first-order accurate as the time step decreases, but the error for the Strang splitting is about half that for the Godunov splitting if the CFL number is fixed. Nonetheless, we may say that the errors are fairly small even for large CFL numbers.

3.5 Summary of the numerical implementation

In this chapter, the high-order-accurate FV method and the time-marching scheme with the time-step splitting technique were developed to resolve wave dispersion and stiffness in continuum bubbly flows and verified by solving some test problems. For all the computations in the following two chapters, the fifth-order monotonicity-preserving FV-WENO reconstruction is implemented in the characteristic space and the HLLC Riemann solver is used to compute the numerical flux. The

grid stretching is adopted for the axisymmetric problems, but otherwise the computational grid is uniform with $\Delta x = R_0^{\text{ref}}$. For shock computations in chapter 4, the third-order TVD Runge–Kutta scheme with uniform time steps (CFL = 0.1) is used to march the entire system. For cavitation computations in chapter 5, the Strang splitting scheme is implemented to march the system in time; the third-order TVD Runge–Kutta scheme with uniform time steps (CFL = 0.1) integrates the convective terms and the Runge–Kutta scheme with adaptive stepsize control resolves the stiff bubble-dynamic sources. For polydisperse flow computations, Simpson's rule is employed to evaluate the moments with respect to the lognormal distribution of equilibrium bubble sizes; 401 quadrature points are used for bubble screen computations in section 4.5, but otherwise 101 quadrature points are used.

Chapter 4

Shock dynamics of bubbly flows

In this chapter, one-dimensional shock propagation through bubbly liquids is simulated to explore the averaged shock dynamics. First, steady shock relations that can be used as initial conditions for shock computations are derived based on a conventional control volume analysis. The experiment of Kameda *et al.* (1998) is then simulated to validate the present method. Shock propagation through polydisperse flows with a lognormal distribution of equilibrium bubble sizes is computed and the effects of polydispersity on the averaged shock structure are quantified. Parameter studies of probable bubble sizes, initial void fractions and shock strength are also conducted to investigate their effects on the averaged dynamics. Finally, shock propagation through a bubble screen is computed and the size distribution effect on the screen performance is discussed.

4.1 Steady shock relations

We first derive the steady shock relations that can be employed as initial conditions for shock computations. In front of the shock, the bubbles are in equilibrium at (R_0, T_0, p_{l0}) where T_0 is the initial temperature of the bubble contents. Far downstream of the shock front, the bubble dynamics are finally damped out and the bubbles are once again in equilibrium at (R_H, T_0, p_{lH}) where R_H is the new equilibrium radius corresponding to the shock pressure $p_{lH} > p_{l0}$. The specification of T_0 in the final equilibrium state follows from the assumption that the liquid temperature is undisturbed and the bubble temperature eventually returns to the liquid temperature. Note that the bubble-

dynamic sources (including the phase interaction term $\tilde{p}$) would vanish under the equilibrium state. The one-dimensional conservation law for mass, momentum and bubble number density is now written in a coordinate system ($x' = x - U_s t$ and velocity u') moving with the shock velocity U_s:

$$\frac{\partial \rho u'}{\partial x'} = 0, \tag{4.1}$$

$$\frac{\partial}{\partial x'}(\rho u'^2 + p_l - \tilde{p}) = 0, \tag{4.2}$$

$$\frac{\partial n u'}{\partial x'} = 0. \tag{4.3}$$

Integrating equations (4.1) to (4.3) from upstream (denoted by subscript 0) to far downstream (denoted by subscript H), it transpires that, independent of the detailed shock structure,

$$-\rho_H u'_H = \rho_0 U_s, \tag{4.4}$$

$$\rho_H u'^2_H + p_{lH} = \rho_0 U_s^2 + p_{l0}, \tag{4.5}$$

$$-n_H u'_H = n_0 U_s, \tag{4.6}$$

where $\rho_0 = (1-\alpha_0)\rho_{l0}$ and $\rho_{lH} = (1-\alpha_H)\rho_{lH}$.

The shock pressure, p_{lH}, may be written as

$$p_{lH} = \left(p_{l0} - p_v + \frac{2\Upsilon}{R_0}\right)\left(\frac{R_H}{R_0}\right)^{-3\kappa} + p_v - \frac{2\Upsilon}{R_H}, \tag{4.7}$$

where the polytropic index κ is set to unity in order that the bubble temperature finally be back to T_0. For adiabatic bubbles, κ needs to be replaced with the specific ratio γ_g. It follows from equations (4.4) and (4.6) that

$$n_H = \left[(1-\alpha_0)\left(\frac{p_{l0}+B}{p_{lH}+B}\right)^{\frac{1}{\gamma}} + \frac{4\pi}{3} n_0 \overline{R_H^3}\right]^{-1}. \tag{4.8}$$

With the aid of equations (4.7) and (4.8), the void fraction α_H corresponding to p_{lH} can be determined.

From equations (4.4) and (4.5), the steady shock speed becomes

$$U_s = \sqrt{\frac{p_{lH} - p_{l0}}{\rho_0 \left(1 - \frac{\rho_0}{\rho_H}\right)}}, \tag{4.9}$$

and the induced velocity far downstream of the shock front is then given by

$$u_H = u'_H + U_s = \left(1 - \frac{\rho_0}{\rho_H}\right) U_s. \tag{4.10}$$

These steady shock relations are similar to those of Matsumoto & Kameda (1996). It is readily shown that the shock speed (4.9) reduces to the sonic speed (3.15) if the shock strength is infinitesimal. Consequently, the shock Mach number may be defined as $M_s = U_s/c$.

4.2 Comparison to experiment

To validate the continuum bubbly flow model, we simulate the experiment of Kameda *et al.* (1998) in which a spatially uniform bubble distribution was carefully created. We consider shock propagation (with shock pressure $p_{lH} = 2.157 p_{l0}$) in an SF_6/silicone-oil monodisperse mixture of $\alpha_0 = 0.0024$ and $R_0^{\rm ref} = 0.613$ mm. The corresponding Peclet number for heat conduction is $\mathrm{Pe}_T = 3770$ (see the definition of Pe_T in appendix B). Note that the large value of Pe_T means that the thermal boundary layer inside the bubble is thin compared to the bubble radius. The bubbles thus tend to behave adiabatically; the adiabatic relation (2.24) with $\kappa = \gamma_g = 1.09$, rather than equation (2.17), is solved. In addition, vapor pressure of the silicone oil at the room temperature is negligible and is set to zero in the computation. Given the shock strength and the adiabatic assumption, the shock Mach number is computed as $M_s = 1.4$. The steady shock relations with $\kappa = \gamma_g$ are initially imposed by a diaphragm at $x = 0$.

The comparison is made in figure 4.1 that shows the time history of the ensemble-averaged liquid pressure at $x = 1.462$ m. In their experiment, the liquid pressure evolution is averaged over ten experimental runs. The simulation well reproduces the amplitude and phase of the oscillations in

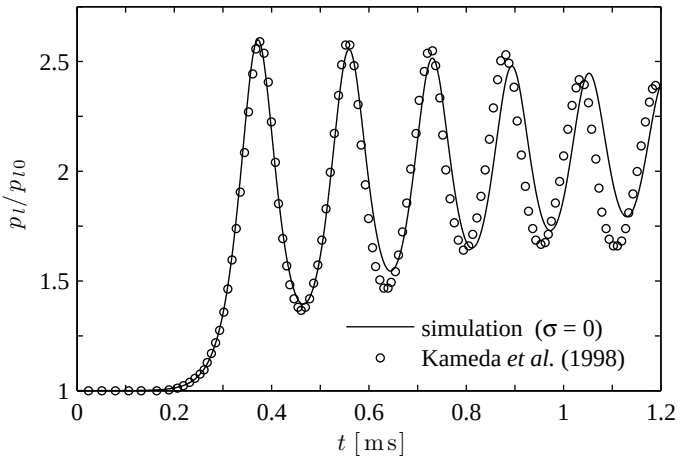

Figure 4.1: Evolution of the averaged liquid pressure for shock propagation in an SF_6/silicone-oil mixture of $\alpha_0 = 0.0024$ and $R_0^{\text{ref}} = 0.613$ mm.

the averaged liquid pressure (so-called relaxation oscillations). The oscillation period τ is about 0.2 ms so that the wavelength is approximately $U_s\tau \approx 6$ cm. On the other hand, the mean bubble spacing is estimated as $n^{-1/3} = 7.4$ mm. It is therefore concluded that the continuum bubbly flow model is accurate since these length scales satisfy the continuum assumption or the scale separation constraint.

4.3 Effects of polydispersity on shock dynamics

We now consider unsteady and steady shock propagation through polydisperse bubbly liquids and quantify the effects of polydispersity on the averaged shock dynamics. As an example, we compute shock propagation (with shock pressure $p_{lH} = 2p_{l0}$) in an air/water mixture of $\alpha_0 = 0.005$ at STP where the equilibrium bubble size is lognormally distributed about $R_0^{\text{ref}} = 10$ μm and with the standard deviation, σ, ranging from 0 to 0.7. Given the shock strength and the isothermal assumption in equation (3.15), the corresponding shock Mach number is computed as $M_s = 1.4$ for all σ. The steady shock relations with $\kappa = 1$ are initially imposed by a diaphragm at $x = 0$. We judge steadiness by observing the first peak of the relaxation oscillations; if the peak pressure is unchanged, the shock propagation can be considered to be in a steady state.

4.3.1 Unsteady shock propagation

The unsteady shock propagation for the cases with $\sigma = 0$ and 0.7 is investigated in figure 4.2 where the spatial evolution of the bubble radius for different equilibrium sizes ($R_0^* = 0.25$, 0.5, 1, 2, 4) is plotted to interpret the individual bubble dynamics. It is seen that the (high-frequency) precursory pressure wave precedes the primary shock wave and propagates essentially with the sonic speed of (pure) water. Whereas the precursory pressure wave in the monodisperse mixture is damped out, that in the polydisperse case is still on the decay. This may be due to the fact that the bubble size distribution decreases the attenuation of high-frequency waves as seen in figure 3.2. It also turns out that only the small-sized bubbles can respond to such high-frequency excitation, for the natural frequency of such small bubbles is comparable with or higher than the forcing frequency. As observed in the low-frequency regime of the linear waves in figure 3.2, the bubble size distribution with $\sigma = 0.7$ smoothes the relaxation oscillations in the averaged pressure and void fraction distributions that appear in the monodisperse case with $\sigma = 0$. It should be noticed that the different-sized bubbles oscillate with different phases in the neighborhood of the primary shock front.

Figure 4.3 presents the spatial evolution of the averaged liquid pressure and the different-sized bubbles (in the polydisperse mixture) at two different times at which the larger-sized bubbles still show radial oscillations (with less effective bubble-dynamic damping). The shock profile in the averaged pressure seems unchanged during this period, and the shock propagation can thus be considered to be steady, regardless of unsteadiness associated with the individual bubble dynamics. In other words, the bubble size distribution yields an apparent damping mechanism of the averaged shock dynamics. In this example, we can say that the effect of polydispersity dominates over the single-bubble-dynamic damping since the individual bubble dynamics have minor impact on the averaged shock dynamics. Because the bubbles with different sizes can oscillate with different phases as in the linear wave propagation in section 3.4.2, the phase cancellations in a polydisperse bubble cloud occur locally and the polydisperse cloud does not oscillate in volume (or in void fraction) in the volume-averaging sense. This collective effect thus leads to the smoothed shock structure.

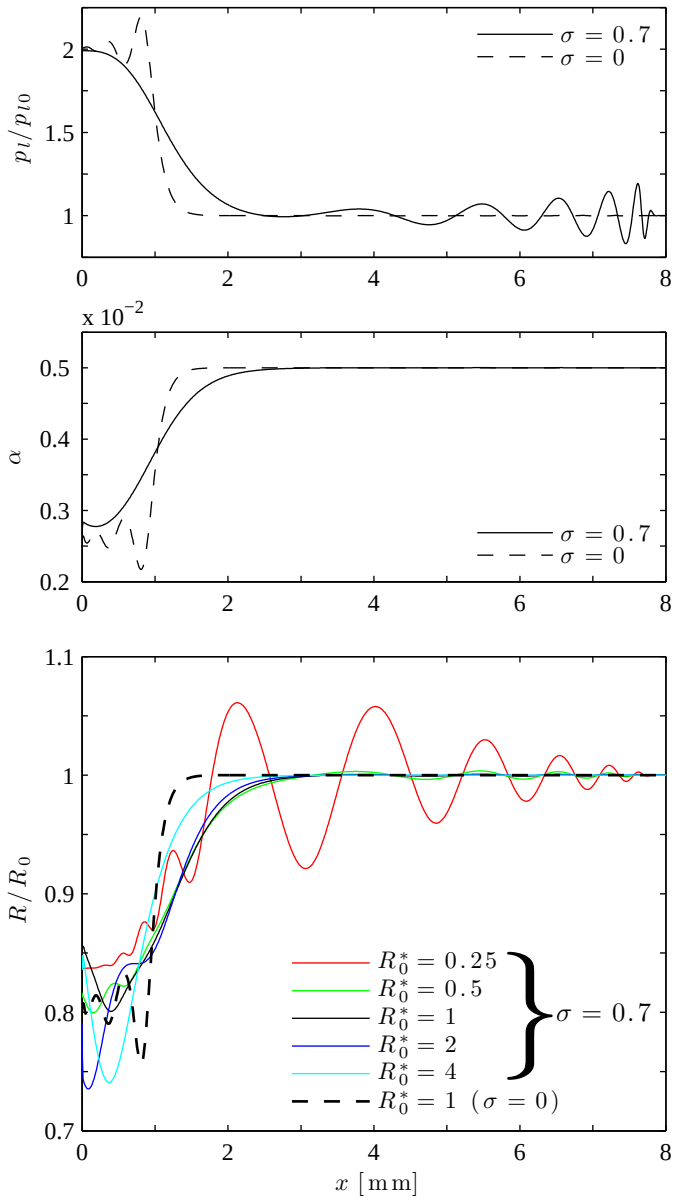

Figure 4.2: Spatial evolution of the averaged liquid pressure (top), the void fraction (middle) and the bubble radius for different equilibrium sizes (bottom) at $t = 5.2$ μs for unsteady shock propagation in an air/water mixture of $\alpha_0 = 0.005$ and $R_0^{\text{ref}} = 10$ μm at STP. The diaphragm is initially located at $x = 0$.

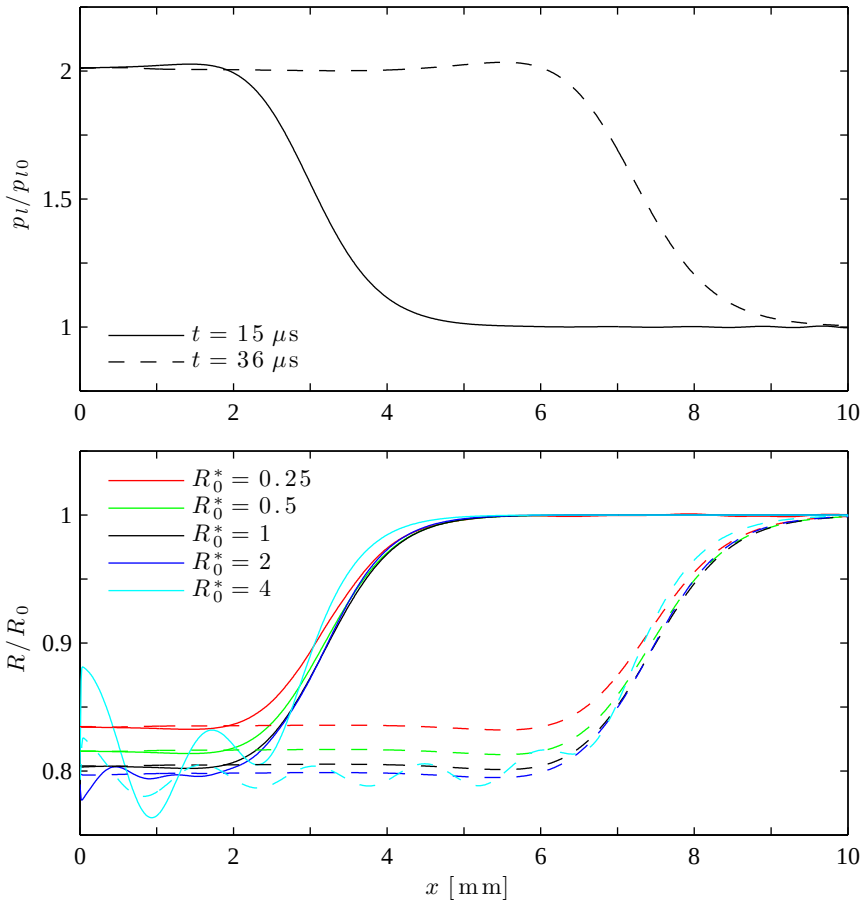

Figure 4.3: Spatial evolution of the averaged liquid pressure (top) and the bubble radius with different equilibrium sizes (bottom) at two different times for unsteady shock propagation in an air/water mixture of $\alpha_0 = 0.005$, $R_0^{\text{ref}} = 10$ μm and $\sigma = 0.7$ at STP. The solid and dashed lines denote the solutions at $t = 15$ μs and 36 μs, respectively.

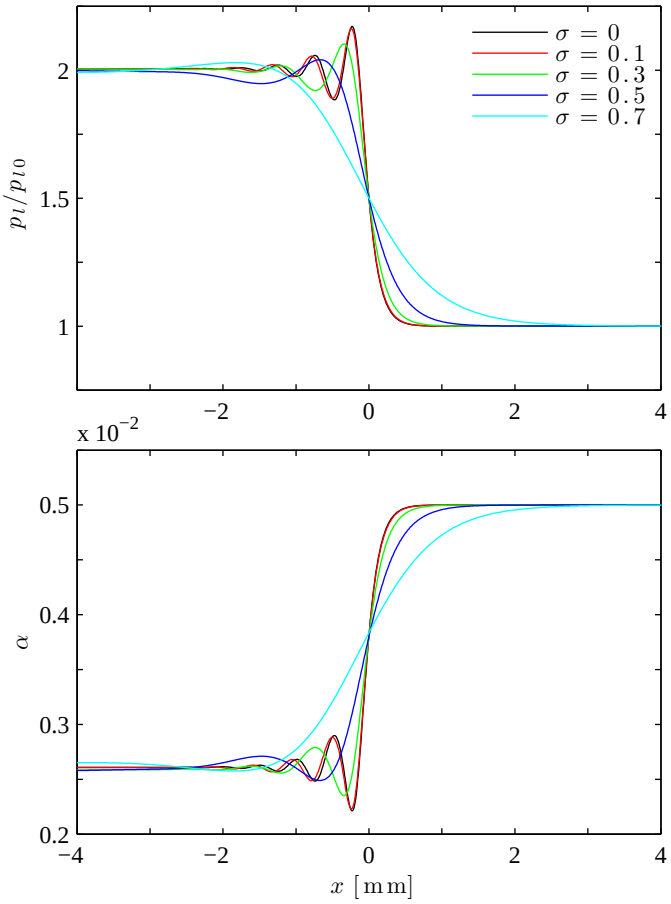

Figure 4.4: Effect of the standard deviation, σ, in the lognormal bubble size distributions on steady shock propagation in an air/water mixture of $\alpha_0 = 0.005$ and $R_0^{\text{ref}} = 10$ μm at STP. The position where the liquid pressure is $(p_{l0} + p_{lH})/2$ is set at $x = 0$.

4.3.2 Steady shock structure

The steady shock structures in the averaged liquid pressure are plotted in figure 4.4 with varying the standard deviation σ in the lognormal distributions (2.10). The position where the averaged pressure is $(p_{l0} + p_{lH})/2$ is set at $x = 0$. It transpires that the averaged shock structure becomes less oscillatory and the first peak become less steep as the bubble size distribution broadens. That is, the broader distribution can yield the more effective apparent damping, for the phase cancellation effect is emphasized with increasing σ. If the distribution is sufficiently broad ($\sigma = 0.7$), the shock profile in both averaged pressure and void fraction fields is practically monotonic; the polydisperse bubble cloud does not show oscillations in the void fraction due to the phase cancellations among

the different-sized bubbles and can be regarded to behave quasistatically in spite of the individual bubble dynamics. Such a smoothed shock profile in a polydisperse mixture was experimentally identified by Beylich & Gülhan (1990).

Finally, we check the the continuum model limitation. For the lognormal distributions (2.10), the mean bubble spacing is computed by

$$l = \left(\frac{3\alpha_0}{4\pi}\right)^{-\frac{1}{3}} \exp\left(\frac{3\sigma^2}{2}\right) R_0^{\mathrm{ref}}. \tag{4.11}$$

For the case of $\alpha_0 = 0.005$ and $\sigma = 0.7$, we have $l \approx 20 R_0^{\mathrm{ref}} = 0.2$ mm, which is much shorter than the wavelength of the smoothed shock profile in figure 4.4; the scale separation constraint is adequately satisfied. However, there may be an issue with the interaction between the largest bubbles, but this is difficult to assess.

4.4 Effects of other parameters

We further conduct parametric studies of the probable bubble size, R_0^{ref}, and the initial void fraction, α_0, and investigate their effects on the steady shock structures. In all the examples presented here, we also discuss the effects of the bubble size distributions using the lognormal function (2.10) with $\sigma = 0$ and 0.7.

The effect of the probable bubble size R_0^{ref} is examined in figure 4.5, which shows the averaged liquid pressure distributions for steady shocks (with shock strength $p_{lH} = 2p_{l0}$) propagating in an air/water mixture of $\alpha_0 = 0.005$ at STP. We consider three probable bubble sizes $R_0^{\mathrm{ref}} = 5\ \mu$m, $10\ \mu$m and $20\ \mu$m. The spatial coordinate is normalized by R_0^{ref}. For the monodisperse cases, the first peak in the relaxation oscillations decreases with increasing R_0^{ref}; the bubble-dynamic damping depends on the bubble sizes and is critical to the averaged shock structures in the monodisperse mixture. However, the inclusion of the broad bubble size distribution leads to the fact that the shock profiles coincide in the normalized coordinate. Namely, the dynamics of the polydisperse bubble cloud are insensitive to the individual bubble dynamics, which are deemphasized by the apparent damping

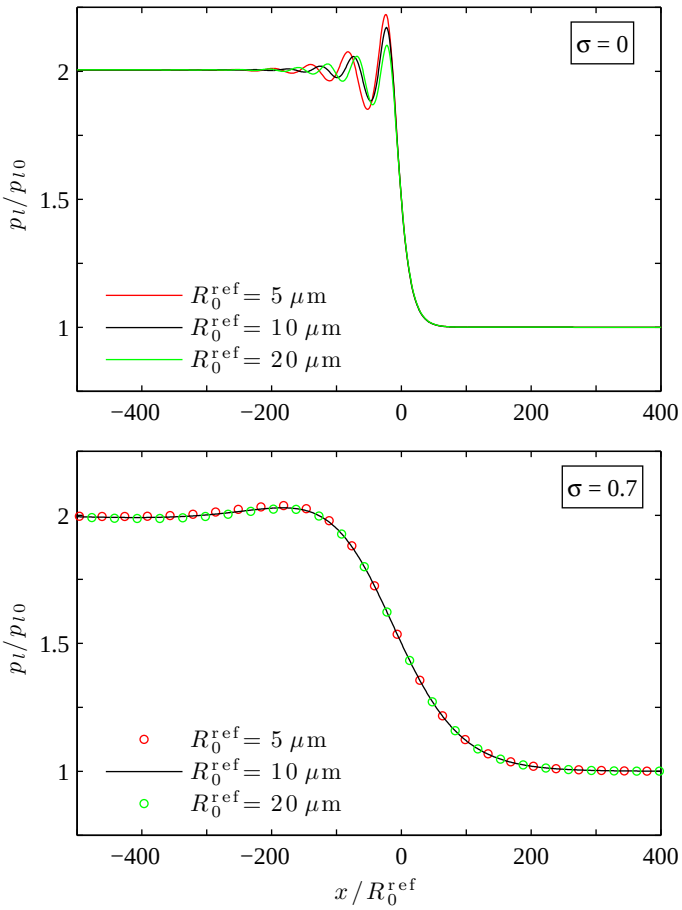

Figure 4.5: Effect of the probable bubble size, R_0^{ref}, on steady shock propagation in an air/water mixture of $\alpha_0 = 0.005$ at STP. $M_s \approx 1.4$ for all the cases.

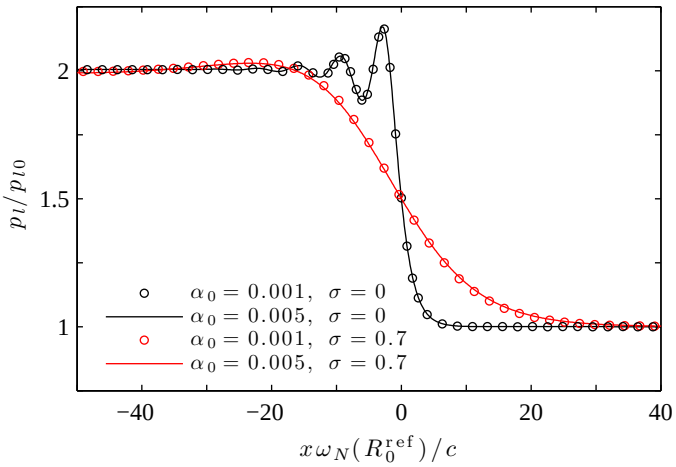

Figure 4.6: Effect of the initial void fraction, α_0, on steady shock propagation in an air/water mixture of $R_0^{\rm ref} = 10$ μm at STP. $M_s \approx 1.4$ for all the cases.

associated with the broad distribution.

The effect of the initial void fraction α_0 is explored in figure 4.6 which presents the averaged pressure distributions for steady shocks (with shock strength $p_{lH} = 2p_{l0}$) in an air/water mixture of $R_0^{\rm ref} = 10$ μm at STP. We consider two initial void fractions $\alpha_0 = 0.001$ and 0.005; the corresponding (isothermal) sonic speeds (3.15) of the mixture in the unperturbed states are $c = 312$ m/s and 142 m/s, respectively. In the normalized coordinate, $x\omega_N(R_0^{\rm ref})/c$, where $\omega_N(R_0^{\rm ref})$ is the isothermal natural frequency for $R_0^{\rm ref}$, the averaged shock structures coincide for both monodisperse and polydisperse cases. That is, the initial void fraction simply changes the propagation speed, but the shock profile remains similar.

4.5 Bubble screen problems

Bubble screens are a useful problem in understanding the fundamental physics of shock/bubble-cloud interactions and are used to prevent damage of submerged structures due to UNDEX (Domenico, 1982). Reflection and transmission of linear wave propagation through a bubble screen were formulated by Carstensen & Foldy (1947) and Commander & Prosperetti (1989). Here, shock/bubble-screen interaction is considered as an application example of the bubbly flow computations.

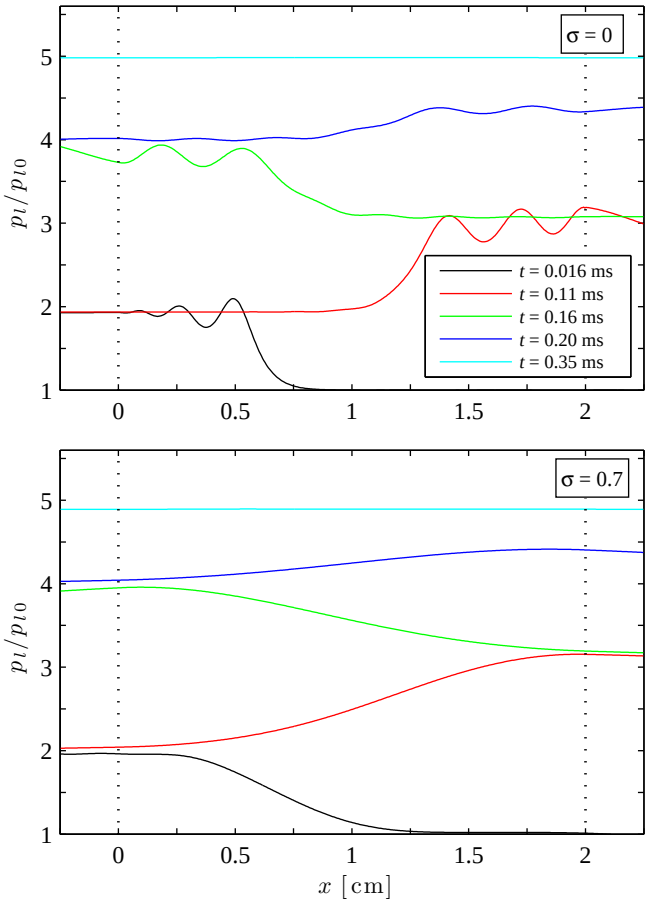

Figure 4.7: Spatial evolution of the averaged liquid pressure for shock propagation through an air/water bubble screen of $\alpha_0 = 0.005$ and $R_0^{\text{ref}} = 50$ μm. The screen is placed between the dotted lines. At $t = 0$, the precursory wave reaches a probe just downstream of the screen.

One-dimensional shock propagation through an air-bubble screen of $\alpha_0 = 0.005$ at STP in water is now computed with the initial void fraction distribution:

$$\alpha = \begin{cases} \alpha_0, & \text{if } 0 < x < L, \\ \epsilon, & \text{otherwise,} \end{cases} \tag{4.12}$$

where $0 < \epsilon \ll \alpha_0$ and $L = 2$ cm. The equilibrium bubble size in the screen ($0 < x < L$) is lognormally distributed about $R_0^{\text{ref}} = 50$ μm and with $\sigma = 0$ and 0.7. The incident, right-going shock with strength $p_{lH} = 5p_{l0}$ is initially placed at $x < 0$.

The snapshots of the averaged liquid pressure distributions are shown in figure 4.7. At the left

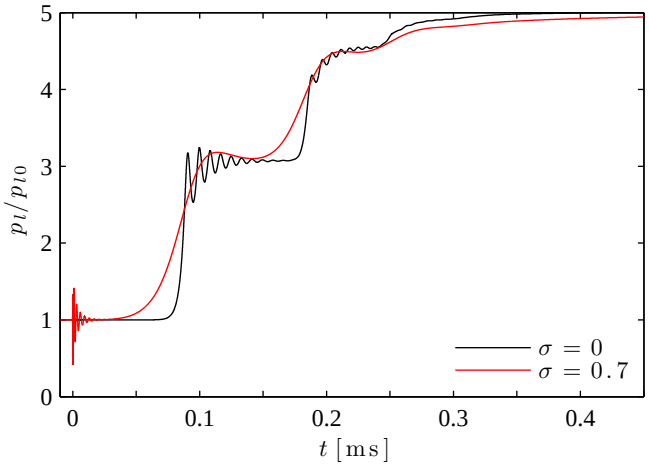

Figure 4.8: Evolution of the liquid pressure for the transmitted waves.

interface ($x = 0$), the incident shock reflects as a rarefaction wave and transmits as a shock due to the fact that the acoustic impedance of the screen is smaller than that of water (i.e., $\rho c < \rho_l c_l$). The transmitted shock trapped in the screen keeps reflecting at the interfaces, and the pressure inside the screen eventually increases to the incident shock pressure. We see that the bubble size distribution smoothes out the oscillatory structure of the trapped waves.

The pressure just downstream of the screen is presented in figure 4.8. The precursory waves propagating with the sonic speed of water are measured at $t = 0$. Note that for the case with no bubble screen, the probe measurement would show an instantaneous jump to p_{lH} at $t \approx 0$. The bubble size distribution with $\sigma = 0.7$ increases the amplitude of the precursory wave because the distribution decreases the attenuation of high-frequency waves (see figure 3.2). The transmitted shock waves leave the screen at late times, and the liquid pressure increases in a step-wise manner because of the reflections of the trapped waves in the screen. As expected, the distribution makes the averaged pressure evolution less oscillatory and broadens the averaged shock width. This implies that the polydisperse bubble screen may be capable of more effectively cushioning UNDEX impulsive loading than the monodisperse screen, but there is still a need to quantify the scattering effect in each realization in order to further investigate the practical implications.

4.6 Summary

One-dimensional shock propagation in bubbly liquids was simulated to quantify the effects of polydispersity on the averaged shock dynamics. The steady shock relations were derived and employed as the initial conditions. The comparison to the experiment of Kameda *et al.* (1998) demonstrated that the present method is capable of resolving the oscillatory shock structure that appears in the monodisperse case. The numerical experiments revealed that the averaged shock structure becomes less oscillatory as the bubble size distribution broadens. If the distribution is sufficiently broad, the shock profile is practically monotonic as experimentally identified by Beylich & Gülhan (1990). Because the different-sized bubbles can oscillate with different frequencies, phase cancellations in a polydisperse mixture occur locally. For cases with the broad size distributions, the polydisperse cloud does not oscillate in volume (or in void fraction) due to the phase cancellations and can be considered to behave quasistatically, regardless of individual bubble dynamics. In this case, the effect of polydispersity dominates over the single-bubble-dynamic damping.

Chapter 5

Dynamics of cavitation clouds

This chapter concerns the dynamics of cavitation clouds caused by the structural interaction with an underwater shock. First, the classical UNDEX/FSI theories of Cole (1948) and Taylor (1950) are reviewed, and the present FSI model with which we simulate the experiment of Rajendran & Satyanarayana (1997) is presented and verified. One-dimensional cloud cavitation with monodisperse and polydisperse nuclei is then simulated to clarify the fundamental mechanism of the inception and collapse of cavitation bubbles.

5.1 Sequence of underwater shock events

The sequence of events of interest in UNDEX can be summarized as follows:

- A solid explosive such as trinitrotoluene (TNT) detonates and rapidly produces a gas bubble with very high pressure.
- The gas bubble expands and produces a strong shock that propagates spherically in the ambient water.
- The shock interacts with interfaces such as the solid target, the seabed and the sea surface.
- There often appear tension waves in water due to structural deformation during reflection or acoustic impedance mismatch.

- The resulting tension waves can cause cloud cavitation, and violent collapse of the cloud of cavitation bubbles may follow.

Particularly, we are now interested in the interaction of UNDEX shocks with the target and the subsequent cloud cavitation. The cloud collapse can account for erosion of the submerged structures (Brennen, 1994, 1995). In the following, we review Cole's empirical formula for the shock evolution and Taylor's fluid-structure interaction model. These classical theories are employed in the present simulations.

5.2 Modeling of underwater shock problems

5.2.1 Cole's formula for shock evolution

As the spherical shock propagates outward, it can be regarded as a linear wave that attenuates as $1/r$ where r is the distance from the center of the bubble that is the product of the detonation of a condensed explosive. Following Cole (1948), the typical evolution of the shock pressure may be represented by an instantaneous pressure increase (with the peak pressure p_s) followed by an exponential decay (with the time constant τ):

$$p_l(t; z, r_s, m_s) = p_{l0}(z) + p_s(r_s, m_s) \exp\left(-\frac{t}{\tau(r_s, m_s)}\right), \tag{5.1}$$

where z is the underwater depth. The peak pressure and time constant depend on the standoff distance, r_s, and (the TNT equivalent of) the charge mass, m_s, and are empirically given by

$$p_s = 52.2 \left(\frac{m_s^{1/3}}{r_s}\right)^{1.13} \text{[MPa]}, \tag{5.2}$$

$$\tau = 96.5 m_s^{1/3} \left(\frac{m_s^{1/3}}{r_s}\right)^{-0.22} [\mu\text{s}], \tag{5.3}$$

where the parameters are based on the SI units.

Suppose that the standoff distance is far larger than the dimension of the target, we can treat

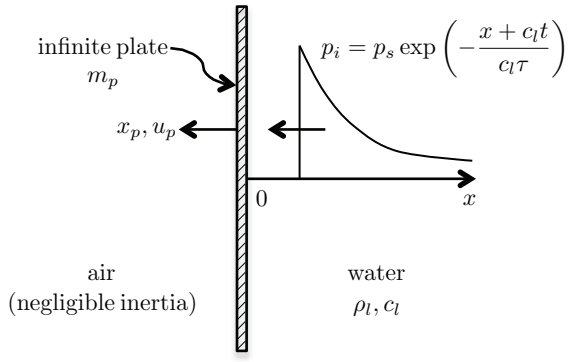

Figure 5.1: Schematic of Taylor's fluid-structure interaction problem.

the spherical wave (5.1) as a one-dimensional (right-going) wave:

$$p_l(x,t) = \begin{cases} p_{l0}, & \text{if } x > c_l t, \\ p_{l0} + p_s \exp\left(\frac{x - c_l t}{c_l \tau}\right), & \text{otherwise.} \end{cases} \tag{5.4}$$

Note that the waves are assumed to propagate with the (constant) sonic speed of water, c_l.

5.2.2 Taylor's free plate model

Consider the fluid-structure interaction problem of Taylor (1950) in which an UNDEX plane shock interacts with a movable rigid plate as depicted in figure 5.1. The plate is assumed to be "free" and "air-backed," meaning that the plate dynamics depend only on the pressure force from the water side. It is also assumed that cavitation does not occur even when water is under tension.

Let p_i and p_r be the pressures of the incident and reflected waves, respectively, at the plate surface ($x = 0$). Newton's second law requires

$$m_p \frac{du_p}{dt} = p_i + p_r, \tag{5.5}$$

where m_p is the mass of the plate per unit area and u_p is the plate velocity. It is assumed that the acoustic relation holds:

$$p_r = p_i - \rho_l c_l u_p. \tag{5.6}$$

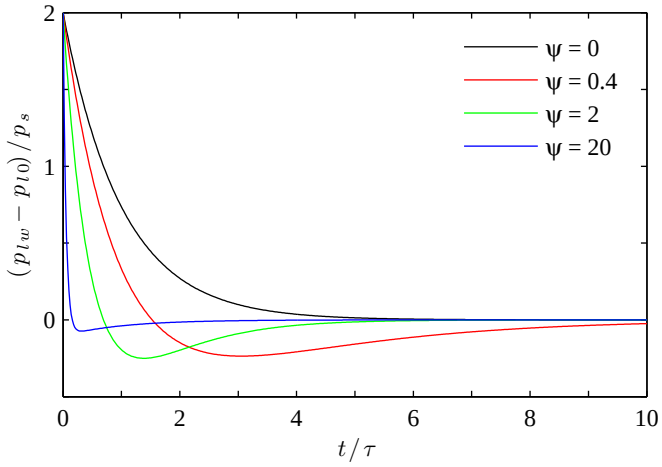

Figure 5.2: Evolution of the wall pressure with different values of ψ.

From equations (5.5) and (5.6) with $p_i = p_s \exp(-t/\tau)$ and $u_p(0) = 0$, the plate velocity and the reflected pressure at $x = 0$ are written as

$$u_p(t) = \frac{2p_s\tau}{m_p(1-\psi)}\left[\exp\left(-\frac{\psi t}{\tau}\right) - \exp\left(-\frac{t}{\tau}\right)\right] > 0, \tag{5.7}$$

$$p_r(t) = \frac{p_s}{1-\psi}\left[(1+\psi)\exp\left(-\frac{t}{\tau}\right) - 2\psi\exp\left(-\frac{\psi t}{\tau}\right)\right], \tag{5.8}$$

where the dimensionless parameter ψ is defined as $\psi = \rho_l c_l \tau/m_p$. The evolution of the plate displacement is described by

$$x_p(t) = \frac{2p_s\tau^2}{m_p(1-\psi)}\left[\frac{1}{\psi}\left\{1 - \exp\left(-\frac{\psi t}{\tau}\right)\right\} - \left\{1 - \exp\left(-\frac{t}{\tau}\right)\right\}\right], \tag{5.9}$$

and the final displacement is thus

$$x_p(\infty) = \frac{2p_s\tau^2}{m_p\psi} = \frac{2p_s\tau}{\rho_l c_l}. \tag{5.10}$$

The evolution of the resulting pressure (i.e., superposition of the incident and reflected waves)

in $0 < x < c_l t$ is

$$p_l(x,t;\psi) = p_{l0} + p_s\left[\exp\left(-\frac{x+c_l t}{c_l\tau}\right) + \frac{1+\psi}{1-\psi}\exp\left(\frac{x-c_l t}{c_l\tau}\right) - \frac{2\psi}{1-\psi}\exp\left(\psi\frac{x-c_l t}{c_l\tau}\right)\right]. \quad (5.11)$$

Specifically, the temporal evolution of the pressure on the plate wall is

$$p_{lw}(t;\psi) = p_{l0} + \frac{2p_s}{1-\psi}\left[\exp\left(-\frac{t}{\tau}\right) - \psi\exp\left(-\frac{\psi t}{\tau}\right)\right]. \quad (5.12)$$

Note that the wall pressure shows an instantaneous increase of the double incident shock strength at the collision time (i.e., $p_{lw}(0;\psi) = p_{l0} + 2p_s$), regardless of the value of ψ. It is readily shown that the minimum pressure is given by

$$p_{lw}(t_{\min};\psi) = p_{l0} + \frac{2p_s}{1-\psi}\left[\exp\left(\frac{2\ln\psi}{1-\psi}\right) - \psi\exp\left(\frac{2\psi\ln\psi}{1-\psi}\right)\right] < p_{l0}, \quad (5.13)$$

where $t_{\min} = 2\tau(\psi-1)^{-1}\ln\psi$.

The wall pressure history with varying the value of ψ is plotted in figure 5.2. Unlike the stationary wall case ($\psi = 0$), the plate motion can yield tension in water and this tension wave can thus cause cavitation near the plate. Because the plate with smaller inertia more promptly responds to the shock loading, the time to achieve the minimum pressure decreases as the plate mass m_p decreases. However, the duration of the tension part increases with increasing m_p (or decreasing ψ). This implies that Taylor's FSI parameter ψ will affect cavitation inception dynamics that depend strongly on the duration of negative pressure as well as its amplitude.

5.2.3 Boundary conditions with plate dynamics

If the plate displacement is sufficiently small, we can incorporate the plate dynamics as boundary conditions in an Eulerian frame; specifically, we substitute $u_w = -u_p$ into the reflective boundary conditions (3.14) where u_w is the induced fluid velocity at $x = 0$ and u_p is updated by solving equation (5.5). The small displacement condition will be satisfied if the final displacement (5.10) is

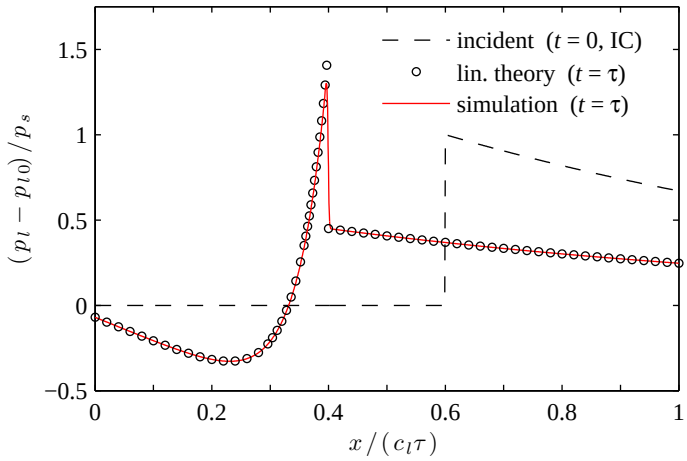

Figure 5.3: Comparison of the theoretical and computed liquid pressure distributions in Taylor's problem with $p_s = 10p_{l0}$ and $\psi = 20$ in pure water (no bubbles).

far smaller than the relaxation length of the UNDEX shock; namely

$$\frac{x_p(\infty)}{c_l\tau} = \frac{2p_s}{\rho_l c_l^2} \ll 1, \tag{5.14}$$

where the denominator, $\rho_l c_l^2$, is 2.2 GPa for water. This suggests that the implementation of the moving wall boundary conditions will be valid for shock pressures up to several megapascals.

In figure 5.3, the reflection of the UNDEX shock ($p_s = 10p_{l0} \approx 1$ MPa) at the plate ($\psi = 20$, $x = 0$) is simulated based on the nonlinear Euler equations for non-cavitating water (CFL $= 0.5$, $\Delta x = c_l\tau/2000$, $\alpha_0 = 0$). The initial pressure and velocity perturbations due to the shock wave are determined with the acoustic relation. The reflective boundary conditions with the plate dynamics are implemented at the left boundary ($x = 0$); the nonreflective boundary conditions with the incoming wave evaluation are imposed at the right boundary ($x = c_l\tau$). Note that this example adequately satisfies the small displacement constraint (5.14). The computation shows good agreement with the theoretical prediction, indicating that the linear theory is reasonably applicable to shock problems in this pressure range.

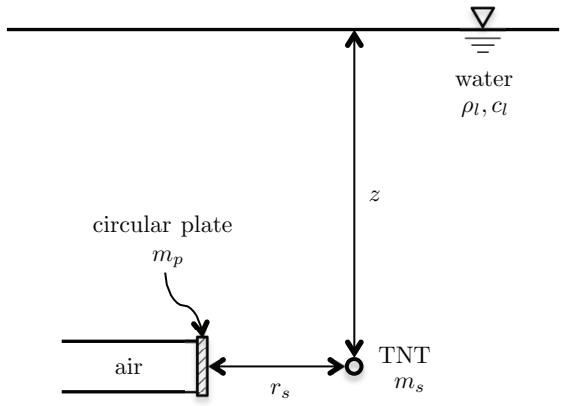

Figure 5.4: Configuration of the UNDEX/FSI model problem.

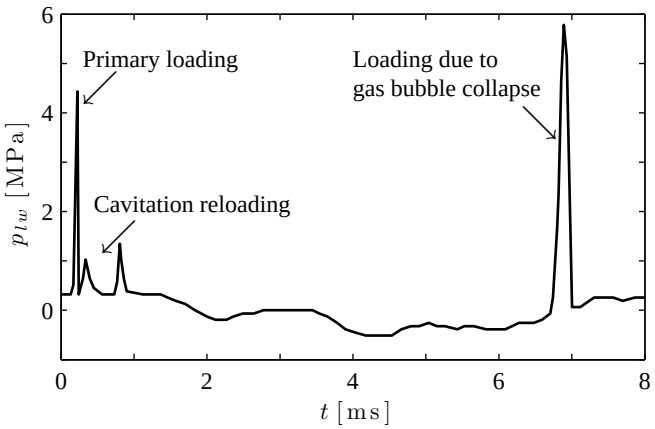

Figure 5.5: An example of the evolution of pressure measured at the plate center (Rajendran & Satyanarayana, 1997).

5.2.4 Model problems

In figure 5.4, the configuration of the present model problem that replicates that of Eldridge *et al.* (1950) and Rajendran & Satyanarayana (1997) is presented. One side of the circular plate is covered with an air-filled cylindrical tube, and the plate is loaded from the other side. The plate is assumed to be rigid so that Taylor's FSI model can be employed. The intent is to observe cloud cavitation and its subsequent collapse near the surface of a shock-loaded plate.

In the experiment of Rajendran & Satyanarayana (1997), an air-backed steel plate ($300 \times 250 \times 4$ mm, $m_p = 31.4$ kg/m^2) was loaded by a shock due to UNDEX with $z = 2$ m, $r_s = 0.8$ m and

$m_s = 1$ g. Figure 5.5 shows typical pressure evolution measured at the plate center. They claimed that the two impulses that follow just after the UNDEX shock reflection are due to the collapse of cavitation bubbles near the loaded plate. With their parameters and Cole's formulas (5.2) and (5.3), the peak pressure and relaxation time of the UNDEX shock are computed as $p_s = 4.98$ MPa and $\tau = 15.2$ μs, respectively. Assuming that the cylindrical tube attached to the plate is massless, the corresponding Taylor's FSI parameter is computed as $\psi = 0.72$. For comparative purposes, the different value of ψ is also considered. Because of the additional mass of the cylindrical tube, the smaller value (e.g., $\psi = 0.1$) may be better to replicate their experiment.

5.3 One-dimensional cloud cavitation

With the neglect of the wave diffraction effect in the model problem in figure 5.4, one-dimensional cloud cavitation caused by the interaction of the UNDEX shock and the free plate is simulated based on the continuum bubbly flow model and Taylor's theory. We now consider the shock with $p_s = 4.98$ MPa and $\tau = 15.2$ μs and the free plate with $\psi = 0.1$ and 0.72. The shock front is initially located three computational cells ($3\Delta x = 3R_0^{\mathrm{ref}}$) away from the plate surface at $x = 0$; the shock-induced velocity is determined from the steady shock relation (4.10). The air nuclei size in water ($T_0 = 20\,^{\circ}$C, $z = 2$ m) is assumed lognormally distributed about $R_0^{\mathrm{ref}} = 50$ μm and with $\sigma = 0$ and 0.7. The initial nuclei concentration is set to be $\alpha_0 = 10^{-5}$ that may be a representative value for tap water (Kedrinskii, 2005). In the following, we observe the dynamics of cavitation clouds in the inception and collapse stages and also discuss the effect of polydispersity on the collapse dynamics.

5.3.1 Inception process

In figure 5.6, we observe the evolution of the shock reflecting from the plate with $\psi = 0.1$ and the subsequent cloud cavitation in the case of monodisperse nuclei. The nuclei are compressed by the shock and show some oscillations in volume behind the shock front. Despite the fact that the initial nuclei concentration is as small as 10^{-5}, the sharp shock front decays due to their bubble-dynamic

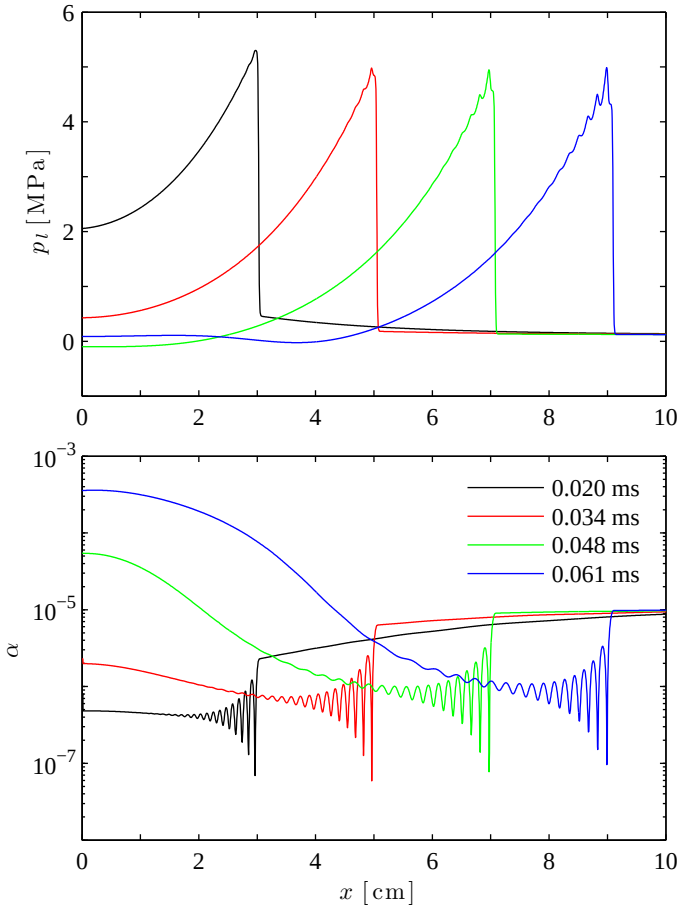

Figure 5.6: Spatial evolution of the averaged liquid pressure (top) and the void fraction (bottom) for the UNDEX shock reflecting from the free plate with $\psi = 0.1$. The time is measured from when the incident shock collides with the plate at $x = 0$.

effect as it evolves. The following tension wave leads to the growth of the cavitation bubbles. The relaxation tail of the reflected shock exhibits oscillations in the averaged pressure field in accordance with the volumetric oscillations of the cavitation clouds. The case with decreasing the plate inertia ($\psi = 0.72$) is presented in figure 5.7. Now that the plate responds to the loading more promptly, the relaxation tail of the shock shortens. As a result, the cloud expansion is more violent and the corresponding pressure rise is augmented.

The wall pressure histories for the cases with $\psi = 0.1$ and 0.72 are compared in figure 5.8. For reference, we also plot the non-cavitating solutions (5.12) in which the minimum (or the most negative) wall pressures for $\psi = 0.1$ and 0.72 are encountered at $t_{\min} = 0.078$ ms and 0.036 ms,

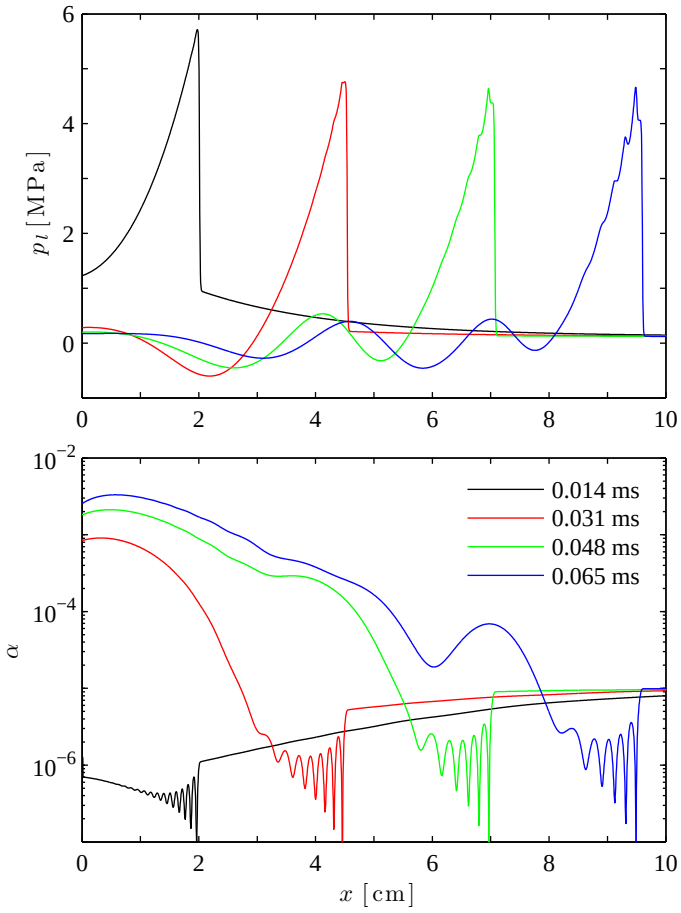

Figure 5.7: As figure 5.6, but with $\psi = 0.72$.

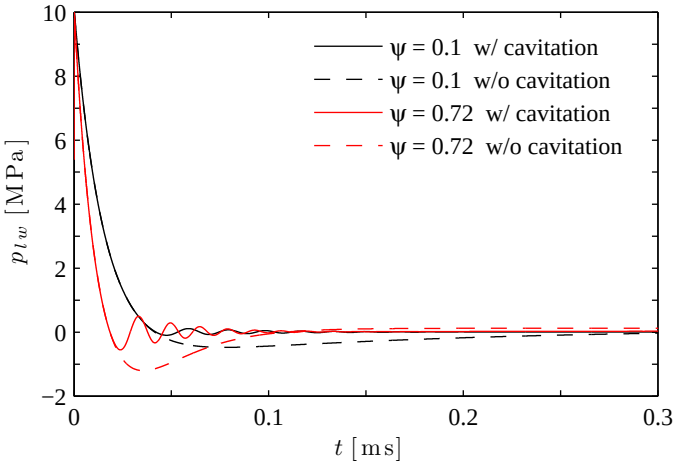

Figure 5.8: The computed wall pressures in figures 5.6 and 5.7 and the non-cavitating solutions (5.12).

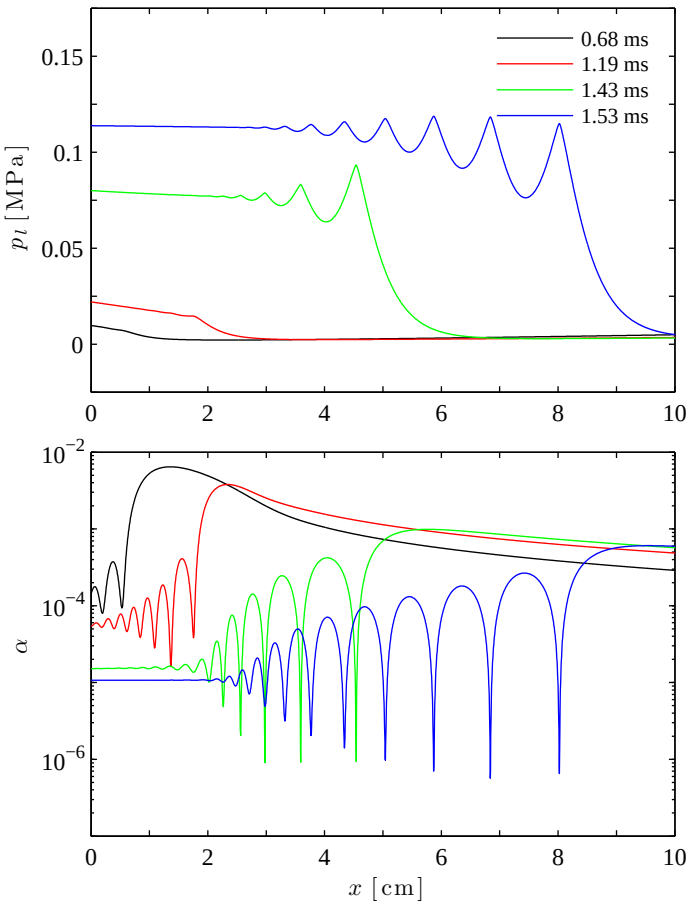

Figure 5.9: As figure 5.6, but for cloud collapse at late times.

respectively. The time for the minimum pressures is longer than the isothermal natural period of bubble oscillations, $2\pi/\omega_N(R_0^{\text{ref}}) = 0.017$ ms. It should be noticed that the negative pressure duration (at which water is under tension) substantially disappears due to cavitation caused by the structural interaction with $\psi = 0.1$. In this case, the decay time t_{min} is about five times as long as the period of bubble oscillations, so that the nuclei tend to respond to the pressure forcing in a quasistatic manner. In other words, the inception of cloud cavitation can occur immediately after the pressure falls below the vapor pressure. The tension wave with $\psi = 0.72$, on the contrary, leads to the negative pressure duration because of the inception delay. This example thus suggests that the cavitation inception is sensitive to the rate of change in liquid pressure to negative values.

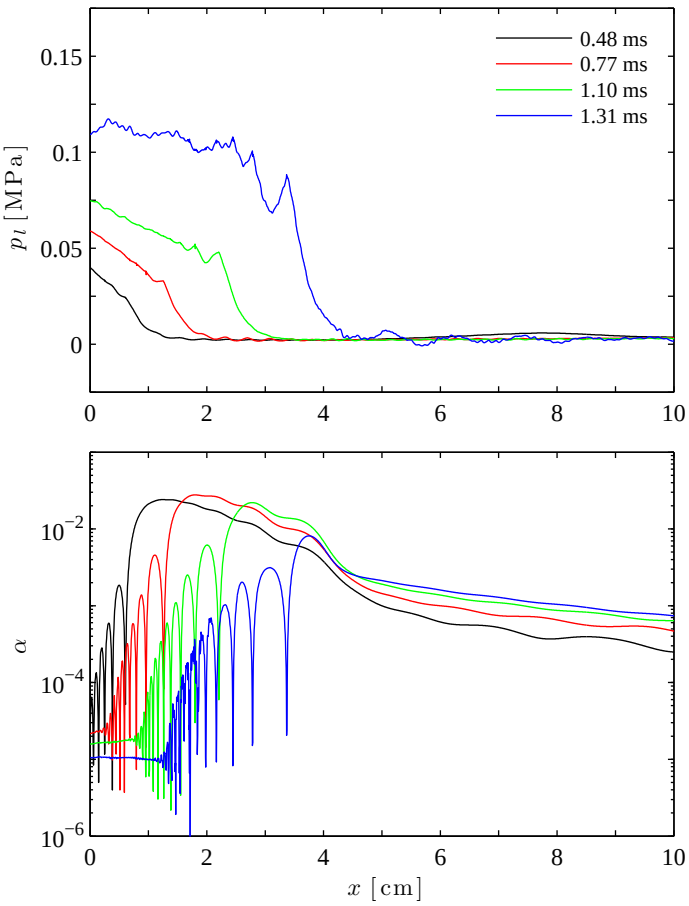

Figure 5.10: As figure 5.7, but for cloud collapse at late times.

5.3.2 Collapse of cavitation clouds

The cavitation clouds in figures 5.6 and 5.7 begin to collapse and the shock forms from the plate surface as presented in figures 5.9 and 5.10, respectively. Note that the cloud collapse in the case of $\psi = 0.72$ starts earlier due to the observation that the wall pressure with increasing ψ returns to the ambient pressure more quickly in the non-cavitating case (see figure 5.2). The resulting shock pressure increases to the ambient pressure as the shock evolves. Behind the shock front, the clouds exhibit some oscillations in void fraction (or in volume); the cloud dynamics lead to oscillatory shock structures in the averaged pressure field as seen in shock propagation through monodisperse bubbly liquids in chapter 4. It is more obvious in the case of $\psi = 0.1$ that the violent collapse yields remarkable increases in the averaged pressure. However, the shock induced by the cloud collapse

is far weaker than the incident shock and cannot explain the cavitation reloading as observed in Rajendran & Satyanarayana (1997). Hence, in this particular example, the one-dimensional cloud collapse is not violent enough to produce strong shocks that can account for the cavitation reloading.

5.3.3 Cavitation with polydisperse nuclei

We now consider cavitation with polydisperse nuclei and investigate the effects of nuclei size distributions on the averaged dynamics of cavitation clouds. As an example, we compute the UNDEX/FSI problem using the lognormal distributions (2.10) of air nuclei sizes with $\sigma = 0$ and 0.7. It is assumed that the bubbles behave adiabatically ($\kappa = \gamma_g = 1.4$).

In figure 5.11, we observe the evolution of the shock reflecting from the plate with $\psi = 0.72$ and the subsequent cloud cavitation. Behind the shock front, the different-sized nuclei bubbles (in the polydisperse case) oscillate with different frequencies. In this example with $\sigma = 0.7$, the phase cancellation effect is so strong (compared to the individual bubble dynamics) that the void fraction distribution is smoothed out. Moreover, the growth of the cavitation cloud with polydisperse nuclei is more gradual, for the larger bubbles respond to external forcing less promptly as seen in the bubble radius distribution. Note that the nuclei bubbles grow to a similar size, regardless of the equilibrium sizes (unless the surface tension is effective enough to hinder the bubble expansion). Also note that the dimensions of the resulting cavitation bubbles with polydisperse nuclei are larger than in the monodisperse case even though the void fractions of the clouds near the plate are similar. This may be due to the fact that the initial bubble number density decreases as the distribution broadens:

$$n_0 = \alpha_0 \left(\frac{4\pi}{3} R_0^{\mathrm{ref3}} \right)^{-1} \exp\left(-\frac{9\sigma^2}{2} \right). \tag{5.15}$$

Noting that the number density change is substantially negligible, the cavitation bubbles with polydisperse nuclei need to further expand to reach the same void fraction of cavitation clouds.

Figure 5.12 shows the evolution of the cavitation clouds collapsing from the plate at a late time. It is seen that the collapsing bubbles in the polydisperse case oscillate with different frequencies.

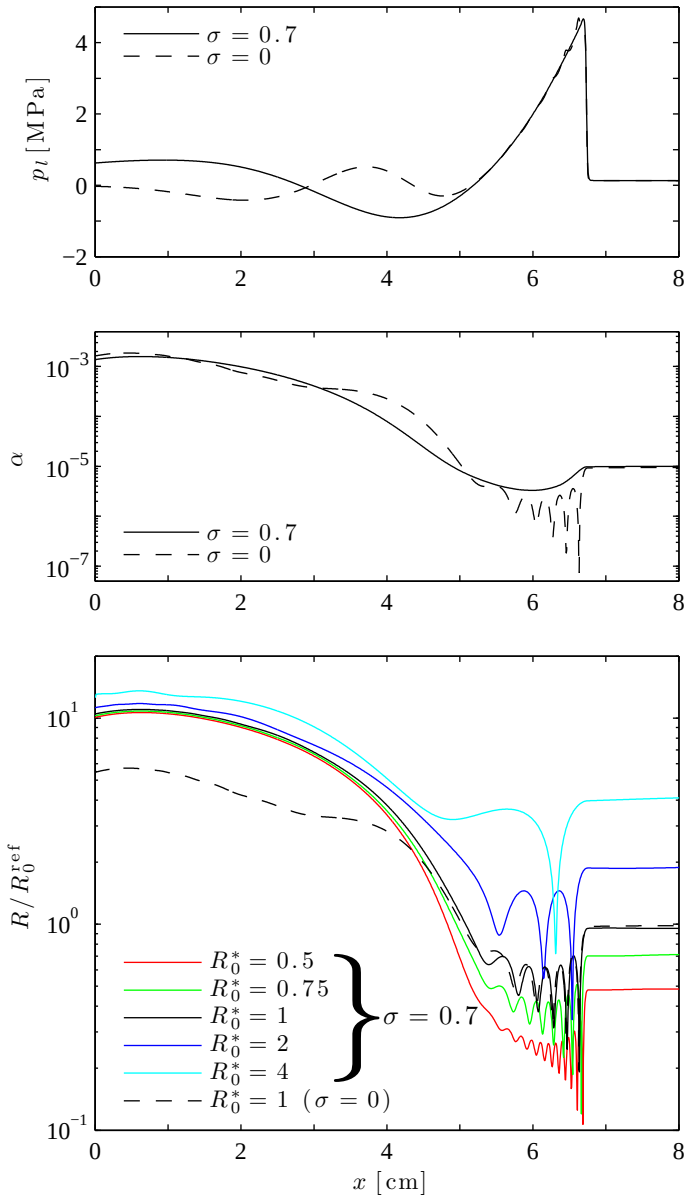

Figure 5.11: Spatial evolution of the averaged liquid pressure (top), the void fraction (middle) and the bubble radius for different equilibrium sizes (bottom) at $t = 0.045$ ms for the UNDEX shock reflecting from the free plate with $\psi = 0.72$.

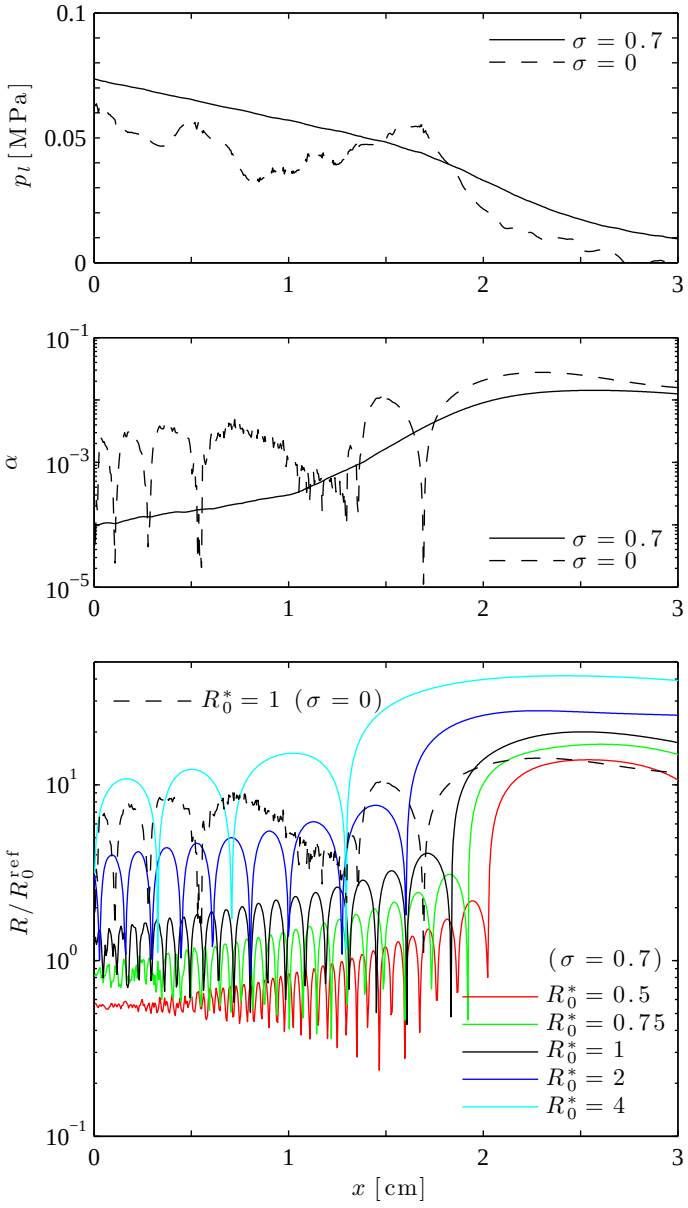

Figure 5.12: As figure 5.11, but for cloud collapse at $t = 0.91$ ms.

The resulting phase cancellations eliminate violent cloud collapse in the void fraction distribution despite the individual bubble collapse. The averaged liquid pressure is also smoothed out because of the gradual cloud behavior. Hence, if the distribution is sufficiently broad, the phase cancellation effect plays a major role in the collapse stage and the averaged cloud dynamics are insensitive to the individual bubble dynamics.

5.4 Summary

The dynamics of cavitation clouds caused by the structural interaction with an underwater shock were simulated based on the classical UNDEX/FSI theories of Cole (1948) and Taylor (1950). Computations of one-dimensional cloud cavitation in monodisperse nuclei were performed to examine the inception and cloud collapse. The cavitation inception is shown to be sensitive to the rate of change in liquid pressure to negative values. If the relaxation time of the tension wave is sufficiently large, the inception can occur immediately after the pressure falls below the vapor pressure. It also transpires that the one-dimensional cloud collapse leads to oscillatory shock structures in the averaged liquid field but is not violent enough to produce strong shocks that can account for structural damage from the cavitation reloading. The computation with polydipserse nuclei shows that the phase cancellations among the collapsing bubbles with broad nuclei size distributions can eliminate violent cloud collapse in the averaged dynamics.

Chapter 6

Shock theory of a bubbly liquid in a deformable tube

The goal of this chapter is to develop the steady shock theory for a bubbly liquid in a deformable cylindrical tube. The quasi-one-dimensional versions of the ensemble-averaged equations are formulated to take into account structural deformation. The steady shock relations are derived and the nonlinear effect due to the gas-phase nonlinearity is examined. For validation purposes, experiments are conducted in which a free-falling steel projectile impacts the top of an air/water mixture in a polycarbonate tube, and stress waves in the tube material are measured to infer wave speeds. Finally, the model limitations are discussed.

6.1 Quasi-one-dimensional FSI equations

In what follows, we include the effect of FSI in the (one-dimensional) ensemble-averaged equations derived in section 2.1.1. Let A be the internal cross-sectional area of the cylindrical tube. We now make the following simplifications: (a) the tube area changes are small and gradual in the flow direction; (b) the tube inertia is negligible; (c) the liquid pressure is only balanced by the hoop stress; and (d) the viscous shear stress on the inner wall is negligible. As a result of these assumptions, the tube area is given quasistatically by (Tijsseling, 1996)

$$A = A_0 \left[1 + \frac{2a_0}{Eh}(p_l - p_{l0}) \right], \tag{6.1}$$

where a is the internal tube radius, h is the wall thickness, E is Young's modulus of the tube material, and the subscript 0 denotes the initial (undisturbed) values. Note that the effect of $\tilde{p}$ is ignored in this expression.

With a conventional control volume analysis, the quasi-one-dimensional versions of equations (2.1), (2.2) and (2.9) (in terms of the cross-sectionally averaged quantities) become

$$\frac{\partial \rho A}{\partial t} + \frac{\partial \rho u A}{\partial x} = 0, \tag{6.2}$$

$$\frac{\partial \rho u A}{\partial t} + \frac{\partial}{\partial x}\left[\rho u^2 A + (p_l - \tilde{p})A\right] = p_l \frac{\partial A}{\partial x}, \tag{6.3}$$

$$\frac{\partial nA}{\partial t} + \frac{\partial nuA}{\partial x} = 0. \tag{6.4}$$

With the aid of equation (6.1), the momentum equation (6.3) is rewritten as

$$\frac{\partial \rho u A}{\partial t} + \frac{\partial}{\partial x}\left[\rho u^2 A + (p_l - \tilde{p})A - \frac{A_0 a_0}{Eh} p_l^2\right] = 0. \tag{6.5}$$

6.2 Steady shock speeds

6.2.1 Sonic speeds

We first derive the sonic speeds of the bubbly liquid with and without FSI. These are needed to define the shock Mach numbers. For convenience, we define the bulk modulus of the mixture, K, as

$$\frac{1}{K} = \frac{1-\alpha}{K_l} + \frac{\alpha}{K_g}, \tag{6.6}$$

where K_l and K_g are the bulk moduli of the liquid and gas, respectively. For Tait liquids, we have $K_l = \gamma(p_l + B)$. If the effects of the vapor and the surface tension are neglected, we may take $K_g = \kappa p_l$ where κ is the polytropic index of the gas. Note that in the low-frequency limit, the polytropic index approaches unity so that the bubbles behave isothermally (Brennen, 1995). With the mixture bulk modulus (6.6), the sonic speed of the mixture (in which the bubbles behave

quasistatically) becomes

$$c = \sqrt{\frac{K}{\rho}} = \sqrt{\frac{K_l/\rho}{1 + \alpha\left(\frac{K_l}{K_g} - 1\right)}}. \tag{6.7}$$

In the dilute limit ($\alpha \to 0$),

$$c \to c_l = \sqrt{\frac{K_l}{\rho_l}}, \tag{6.8}$$

where c_l is the sonic speed of the liquid alone.

We now include the effect of the structural compressibility on the mixture sonic speed (6.7). The Korteweg–Joukowsky wave speed for the mixture may be defined and evaluated as

$$c_J = \left(\frac{1}{A}\frac{\partial \rho A}{\partial p_l}\bigg|_{\kappa}\right)^{-\frac{1}{2}} = \frac{c}{\sqrt{1+\eta}} = \sqrt{\frac{K_l/\rho}{1 + \alpha\left(\frac{K_l}{K_g} - 1\right) + \eta_l}}, \tag{6.9}$$

where η and η_l determine the extent of fluid-structure coupling for the cases of the mixture and the liquid alone, respectively:

$$\eta = \frac{2Ka_0}{Eh}, \quad \eta_l = \frac{2K_l a_0}{Eh}.$$

This wave speed (6.9) for the mixture is identical to that of Kobori *et al.* (1955). It yielded good agreement with their experiments. Note that the structural compressibility reduces the linear wave speed in the mixture (i.e., $c_J < c$). In the dilute limit,

$$c_J \to c_{lJ} = \frac{c_l}{\sqrt{1+\eta_l}}, \tag{6.10}$$

where c_{lJ} is the (non-dispersive) wave speed for the case of the liquid alone.

Skalak (1956) quantified the tube inertia and the Poisson's ratio effects on linear waves (also see Tijsseling *et al.*, 2008). Even for the case of pure liquids, the inclusion of the tube inertia leads to wave dispersion. Skalak's extended theory of water hammer predicts the following wave speeds for the pure liquid case:

$$c_1,\ c_2 = c_l \left[\frac{r_3 \mp \sqrt{r_3^2 - 4r_2^2(1-\nu^2)(2r_1 + r_2)}}{2(2r_1 + r_2)}\right]^{1/2}, \tag{6.11}$$

where

$$r_1 = \frac{\rho_l}{\rho_s}\frac{a_0}{h}, \quad r_2 = \frac{c_s^2}{c_l^2}, \quad r_3 = 2r_1r_2 + r_2 + r_2^2(1-\nu^2), \quad c_s = \sqrt{\frac{E}{\rho_s(1-\nu^2)}}.$$

Here, c_s, ρ_s and ν are the (longitudinal) sonic speed, the density and the Poisson's ratio of the tube material, respectively. The wave speeds c_1 and c_2 are the extended versions of the Korteweg–Joukowsky wave speed c_{lJ} (for infinite wave length) and the precursory wave speed, respectively. For example, water ($c_l = 1480$ m/s) in the polycarbonate tube ($E = 2.13$ GPa, $\rho_s = 1200$ kg/m^3, $\nu = 0.37$, $a_0 = 3h = 19.1$ mm) used in the experiments (see section 6.3) would yield

$$c_{lJ} = 553\,\text{m/s}, \quad c_1 = 547\,\text{m/s}, \quad c_s = 1430\,\text{m/s}, \quad c_2 = 1440\,\text{m/s}.$$

It follows that the speed c_1 is only slightly lower than the Korteweg–Joukowsky speed c_{lJ}. Hence, if the wave length is sufficiently long (compared to the tube radius a_0), the effects of the tube inertia and of Poisson coupling are negligible. We also notice that the precursory wave speed c_2 is very close to the sonic speed of the tube material.

6.2.2 Steady shock relations

Following the derivation of the steady shock relations (without FSI) in section 4.1, we develop those for a shock in a bubbly liquid in a deformable cylindrical tube. Integrating the quasi-one-dimensional equations (6.2), (6.5) and (6.4), in a frame moving with the shock speed U_s, from upstream (denoted by subscript 0) to far downstream (denoted by subscript H), we find

$$-\rho_H u'_H A_H = \rho_0 U_s A_0, \tag{6.12}$$

$$\rho_H u'^2_H A_H + g(p_{lH}) = \rho_0 U_s^2 A_0 + g(p_{l0}), \tag{6.13}$$

$$-n_H u'_H A_H = n_0 U_s A_0, \tag{6.14}$$

where u' is the velocity measured in a coordinate system moving with U_s, and

$$g(p_l) = A_0 \left(1 - \frac{2p_{l0}a_0}{Eh}\right) p_l + \frac{A_0 a_0}{Eh} p_l^2. \tag{6.15}$$

From equations (6.12) and (6.13), the steady shock speed becomes

$$U_s = \sqrt{\frac{g(p_{lH}) - g(p_{l0})}{\rho_0 A_0 \left(1 - \frac{\rho_0 A_0}{\rho_H A_H}\right)}}, \tag{6.16}$$

and the induced velocity far downstream of the shock front is then given by

$$u_H = u'_H + U_s = \left(1 - \frac{\rho_0 A_0}{\rho_H A_H}\right) U_s, \tag{6.17}$$

where the mixture density, ρ_H, at p_{lH} is determined with the isothermal bubble assumption as in section 4.1. Noting that the shock speed (6.16) approaches the Joukowsky wave speed (6.9) in the limit of $p_{lH} \to p_{l0}$, the shock Mach number may be defined as $M_s = U_s/c_J$. It should also be noticed that in the limit of infinite structural stiffness ($E \to \infty$), the steady shock relations derived in this section reduce to the standard result for bubbly flows without FSI.

6.2.3 Gas-phase nonlinearity

We document the steady shock relations for the case of bubbly water with $\eta_l = 6.14$ where the value of η_l is computed based on the properties of the polycarbonate tube that is used in the experiments described in section 6.3. For simplicity, we ignore the effects of vapor pressure and surface tension. Figure 6.1 demonstrates the effects of the initial void fraction and the shock pressure on the shock speed and Mach number. Note that $p_{lH} = p_{l0}$ indicates the linear wave cases, in which the shock speeds (6.16) and (4.9) reduce to the sonic speeds (6.9) and (6.7), respectively. It follows from figure 6.1 (left) that the reduction in the shock speed due to structural compressibility is minimized for finite values of α_0 since the gas-phase compressibility dominates over the compressibility of the water and structure. It is also seen that the shock speeds are greatly reduced by even a tiny void

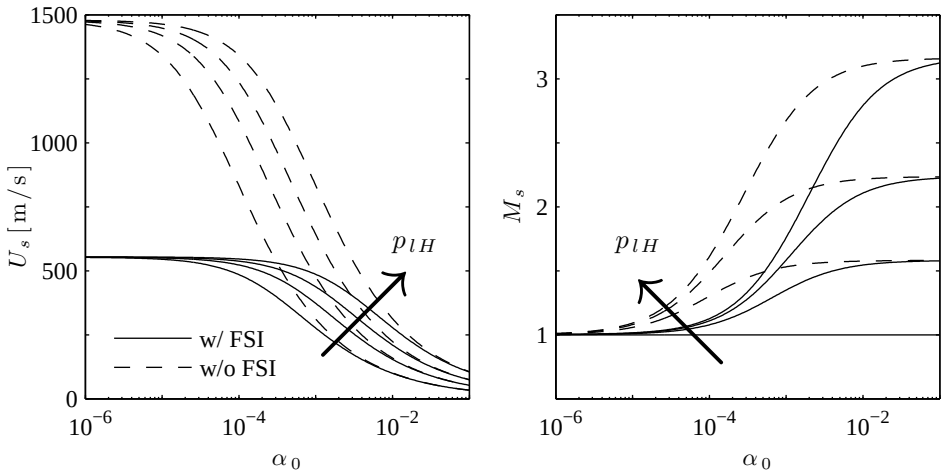

Figure 6.1: Steady shock speeds (left) and shock Mach numbers (right) as a function of initial void fraction in bubbly water with $\eta_l = 6.14$ (FSI) and $\eta_l = 0$ (no FSI). The curves are parameterized by shock pressure $p_{lH}/p_{l0} = 1$, 2.5, 5, 10 where $p_{l0} = 101$ kPa.

fraction. Moreover, unless the void fraction is extremely small, the finite shock strength yields a significant deviation from the linear wave speed due to the nonlinearity associated with the gas-phase compressibility. As a result, the shock Mach number increases as the void fraction increases as seen in figure 6.1 (right). We note that the shock Mach numbers are only slightly greater than 1 for the case of water alone ($\alpha_0 = 0$) since the pressure perturbations (in water) up to several hundred atmospheres remain very weak (Thompson, 1972). This fact was experimentally confirmed by Nagayama *et al.* (2002) and Inaba & Shepherd (2010).

To quantify the effect of the gas-phase nonlinearity, we further examine the steady shock relations. For the case of infinitesimal shock strength ($\Delta p_l = p_{lH} - p_{l0} \ll p_{l0}$), the shock speed (6.16) can be approximated by

$$U_s \approx c_J \left(1 + \frac{\Delta p_l}{\hat{K}}\right), \tag{6.18}$$

where $\hat{K}$ is defined as

$$\hat{K} = c_J \left(\frac{dU_s}{d\Delta p_l}\bigg|_{\Delta p_l = 0+}\right)^{-1}. \tag{6.19}$$

In the limits of $\alpha_0 \to 0$ (pure liquid) and $\eta \to 0$ (no FSI), we find $\hat{K} \to 4K_l/(\gamma + 1)$. Thus, $\hat{K}$ may be called the *modified* bulk modulus. It follows from equation (6.18) that the linear theory (where

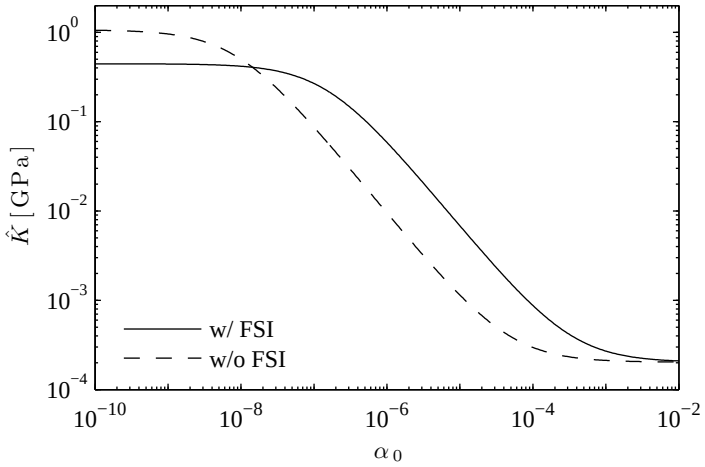

Figure 6.2: Modified bulk modulus of bubbly water with $\eta_l = 6.14$ (FSI) and $\eta_l = 0$ (no FSI).

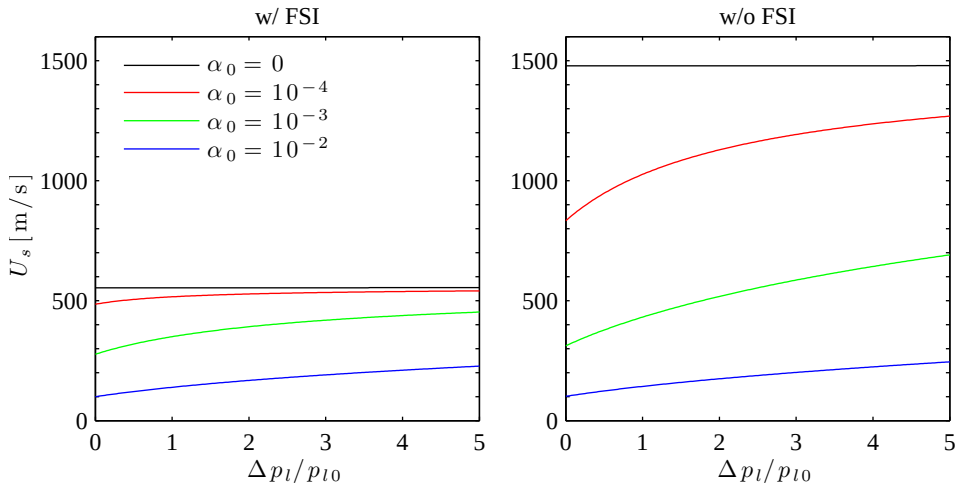

Figure 6.3: Steady shock speeds as a function of shock pressure in bubbly water with $\eta_l = 6.14$ (FSI) and $\eta_l = 0$ (no FSI). The curves are parameterized by initial void fraction α_0.

the relation $U_s = c_J$ holds) is effectively valid under the condition $\hat{K} \gg \Delta p_l$. Hence, the modified bulk modulus, $\hat{K}$, of the mixture can be regarded as a measure of the nonlinearity in the sense that larger values of $\hat{K}$ make the linear theory applicable to a broader range of the shock pressures. The modified bulk moduli of bubbly water (with and without FSI) are plotted as a function of α_0 in figure 6.2. It turns out that even a small void fraction yields a several-orders-of-magnitude reduction in the value of $\hat{K}$. This implies that the applicability of the linear theory is limited in the case of bubbly mixtures. To verify this observation, in figure 6.3 we plot the steady shock speeds (6.16) and (4.9) for the shock strength Δp_l ranging from 0 to $5p_{l0}$. It is obvious that the shocks in pure water ($\alpha_0 = 0$) propagate essentially with c_{lJ} for the FSI case (or c_l for the no-FSI case) in this pressure range due to the fact that the modified bulk moduli are much larger than the shock strength. In other words, the linear theory is sufficient to predict the shock speeds for both FSI and no-FSI cases. However, for the case of bubbly water, the shock speeds deviate from the sonic speeds of the mixtures as the shock strength increases. Since the bulk moduli of the mixtures are comparable to the shock strength, the term $\Delta p_l/\hat{K}$ in equation (6.18) cannot be ignored. In such cases, the gas-phase nonlinearity comes into play and the shock theory is needed to accurately predict the wave speeds.

6.3 Water-hammer experiments

6.3.1 Experimental setup

Experiments were conducted in order to investigate the steady shock theory. The experimental apparatus depicted in figure 6.4 is similar to that of Inaba & Shepherd (2010), and consists of a vertical polycarbonate tube (PCT0021.25, San Diego Plastics; $E = 2.13$ GPa, $\rho_s = 1200$ kg/m^3, $a_0 = 3h = 19.1$ mm) filled with an air/water mixture. A barrel is mounted above the tube and a 1.50-kg cylindrical steel projectile falls under gravity, g. The free-falling projectile (with drop height $H_p = 2$ m or 0.5 m) impacts a 0.42-kg polycarbonate buffer inserted into the top of the tube rather than directly hitting the bubbly liquid surface. Stress waves in the tube are measured using six

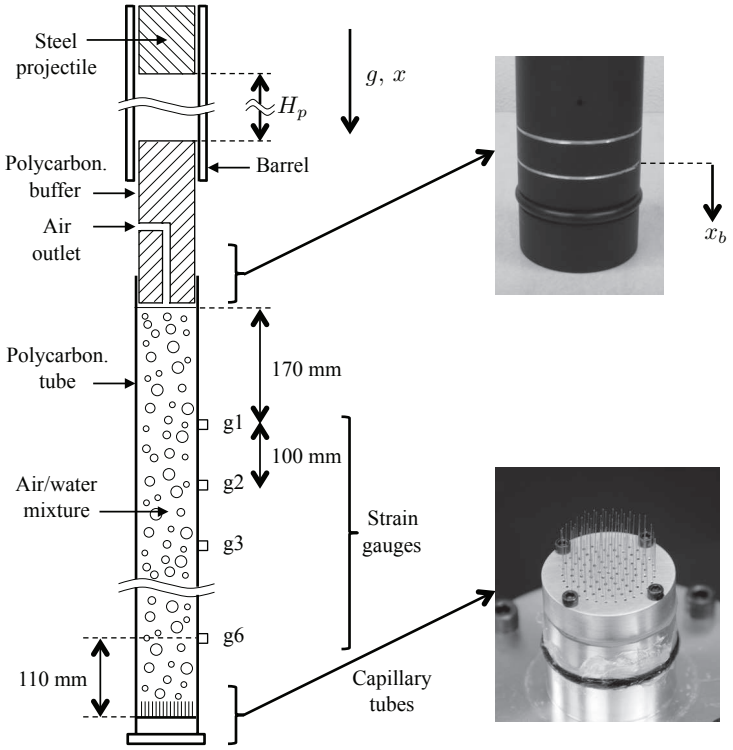

Figure 6.4: Schematic of the experimental setup. The apparatus was constructed by K. Inaba and J. E. Shepherd; the bubble generator was created based on the idea of T. Sanada.

strain gauges (SR-4, Vishay; denoted by g1 to g6 in figure 6.4) placed at intervals of 100 mm along the tube and oriented in the hoop direction; the signals are processed using a signal conditioning amplifier (2300 System, Vishay), and are stored in a digital recorder (NI 6133, National Instruments; sampling rate 2.5 MHz). Strain detection at the strain gauge location g2 triggers the recording at time $t = 0$.

6.3.2 The method of bubble generation

The bubbles are created using a bubble generator consisting of an aluminum plate and capillary tubes (TSP020150, Polymicro Technologies; inner diameter 20 μm) as shown in figure 6.4; the intent is to create small bubbles and as homogeneous a mixture as possible. Up to an initial void fraction of $\alpha_0 = 0.0056$, 91 capillary tubes are used; for higher void fractions, the number increases to 217. The capillary tubes are located in the drilled holes of the plate and are fastened with epoxy. One side

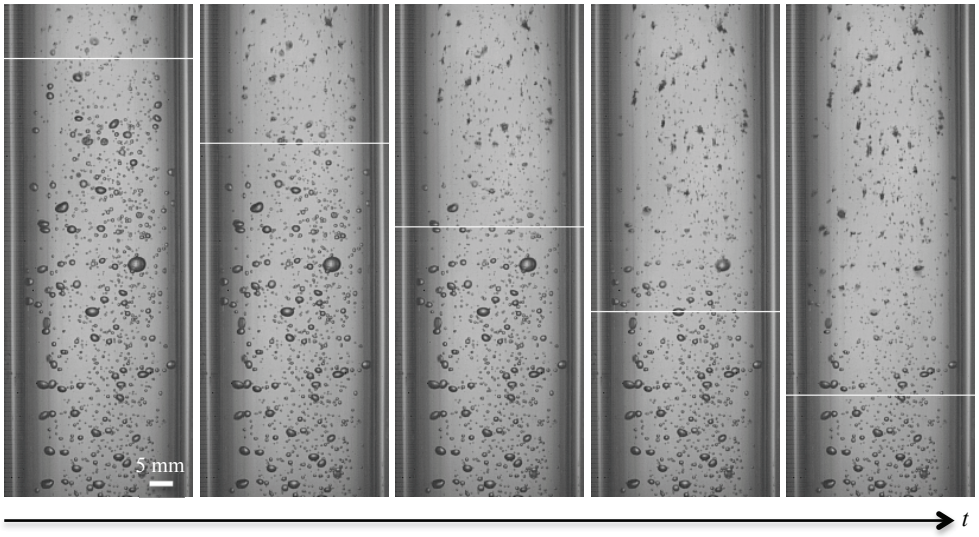

Figure 6.5: Evolution of the compression wave that propagates downward through an air/water mixture for $H_p = 2$ m and $\alpha_0 = 0.0081$. The white lines denote the estimated wave front position. The frame rate is 20000 frames per second (fps). The bubble visualization was conducted with the help of J. S. Damazo and R. Porowski.

of the plate is tightly covered with a chamber. The chamber is pressurized, and the air is injected, due to the pressure head, into the fluid column. The injected bubbles rise upward to the column surface, and eventually escape from an air outlet in the buffer.

Distilled water is used for the case of no air injection; otherwise, tap water is used. Note that the number of tiny bubbles present in tap water is negligible compared to that of the injected air. The water temperature is kept at 23 °C so that the vapor pressure is much smaller than one atmosphere.

Images of the bubbles are captured by a high-speed video camera (Phantom v7.3, Vision Research). A white LED lamp (Model 900445, Visual Instrumentation Corporation) is used for backlighting. A water jacket is attached outside the tube to minimize image distortion. The evolution of the compression wave for the case of $H_p = 2$ m and $\alpha_0 = 0.0081$ is shown in figure 6.5 where the wave front position is also estimated from the measured wave speed ($U_s = 355$ m/s) that is computed in section 6.3.5. It follows that the predicted wave position generally corresponds to where the bubbles are collapsing. Moreover, the bubble size is found to be broadly distributed (i.e., the mixture is polydisperse), and the mixture is nearly homogeneous. The detailed images of the

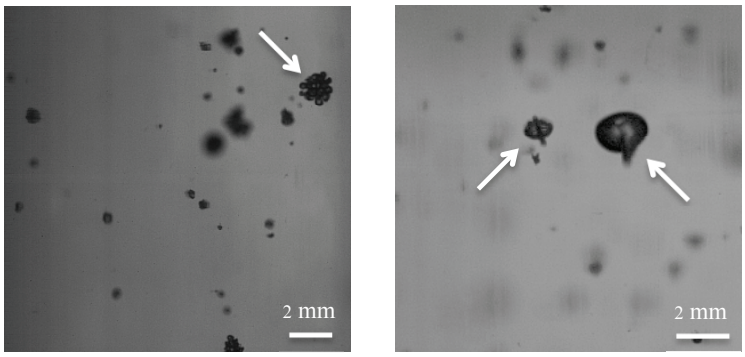

Figure 6.6: Examples of the images of bubble fission (left) and re-entrant jets (right). The frame rates are 25000 fps and 79000 fps, respectively.

compressed bubbles are presented in figure 6.6. The bubble fission in figure 6.6 (left) may be due to a Rayleigh-Taylor-type instability (Brennen, 2002). The re-entrant jets in figure 6.6 (right) are induced by interaction with the shock wave (Johnsen & Colonius, 2009).

The initial void fraction (up to one percent) is estimated based on the difference in the column height with and without the air injection. Uncertainty in this measurement is ± 0.1 mm except for the case of the highest void fraction, $\alpha_0 = 0.01$, in which the column surface waves increase the uncertainty to $\pm\, 0.5$ mm. In the water-hammer experiments, the following void fractions were tested: $\alpha_0 = 0$ (no air injection), 0.0013 ± 0.0001, 0.0024 ± 0.0001, 0.0056 ± 0.0001, 0.0081 ± 0.0001 and 0.010 ± 0.001.

6.3.3 The buffer dynamics

In the present experiments, the liquid pressure is unknown. Hence, the buffer velocity $\dot{x}_b$ (or the piston velocity u_H in the shock theory) is critical to estimate to validate the shock theory. Three experimental runs were conducted for each case of H_p and α_0. For every run, the buffer position x_b (represented by the two lines with a 10-mm separation seen in figure 6.4) was recorded using the high-speed camera with recording rate of 32000 frames per second, and the position history was extracted from the movies with MATLAB image processing. Strain detection at the strain gauge g2 triggers the recording with delay 0.3 ms. As an example, in figure 6.7 we exhibit the evolution of

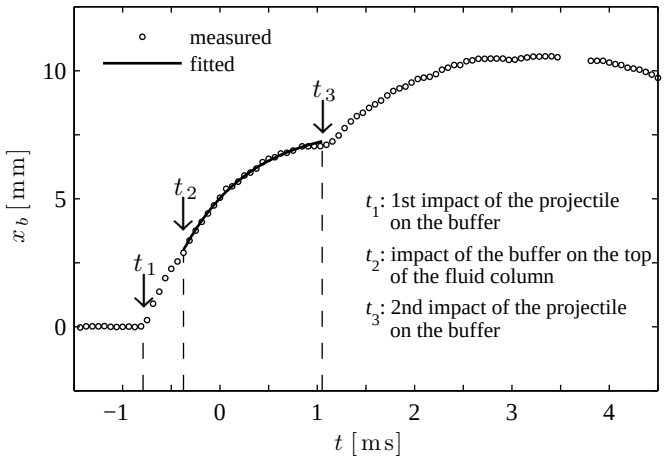

Figure 6.7: Evolution of the buffer position for $H_p = 2$ m and $\alpha_0 = 0$.

the buffer position for the case of $H_p = 2$ m and $\alpha_0 = 0$. The projectile impacts the buffer at time t_1; the projectile and the buffer separate after the collision. The buffer then impacts the top of the fluid column at time t_2. The projectile again impacts the buffer at time t_3. It should be pointed out that the buffer motion from t_1 to t_2 compresses the air in the gap between the column surface and the bottom of the buffer. The wave that results from the air compression thus propagates through the fluid column before the buffer collides directly with the column surface. However, the air inertia is negligible compared to the buffer inertia, so that the resulting wave will have smaller energy than that generated by the direct impact of the buffer.

The buffer dynamics from t_2 to t_3 may be described by Newton's second law (Dashpande *et al.*, 2006; Shepherd & Inaba, 2009). For simplicity, the buffer is treated as a rigid body and wall friction is neglected. The equation of motion of the buffer is then given by

$$m_b \ddot{x}_b = -\Delta p_l A_0, \tag{6.20}$$

where m_b is the mass of the buffer and the right-hand side represents the pressure force acting on the bottom of the buffer. In the linear case, this pressure force may be approximated by $\Delta p_l A_0 = \rho_0 c_J \dot{x}_b A_0$ as can be derived from equations (6.12) and (6.13). Integrating equation (6.20) once and

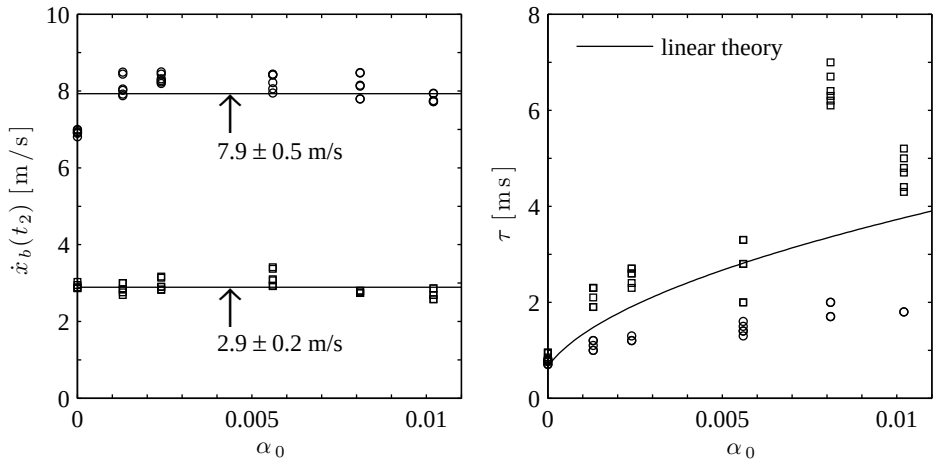

Figure 6.8: The buffer velocity at time t_2 (left) and the relaxation time τ (right) as a function of initial void fraction. The symbols (circles and squares) denote the measured values for $H_p = 2$ m and 0.5 m, respectively.

specifying the initial condition at time t_2, we get a solution of the form,

$$\dot{x}_b = \dot{x}_b(t_2) \exp\left(-\frac{t - t_2}{\tau}\right), \tag{6.21}$$

where τ is the relaxation time for the exponential decay:

$$\tau = \frac{m_b}{\rho_0 c_J A_0}. \tag{6.22}$$

Thus, the evolution of the buffer position is expressed by an exponential function.

The measured buffer positions between t_2 and t_3 were fitted to an exponential by the least-squares method. In addition, the time t_2 was determined by observing the still images taken from the high-speed camera. The resulting buffer velocity $\dot{x}_b(t_2)$ and relaxation time τ are presented in figure 6.8. We find that the buffer velocity $\dot{x}_b(t_2)$ is only weakly dependent on the void fraction and therefore seems to depend only on the drop height H_p; it is 7.9 ± 0.5 m/s and 2.9 ± 0.2 m/s for $H_p = 2$ m and 0.5 m, respectively, where the error bounds represent the standard deviation of all the runs. It follows from figure 6.8 (right) that the linear theory (6.22) is in qualitative agreement with the experimental data and is particularly good for the case of no air injection. Moreover, the

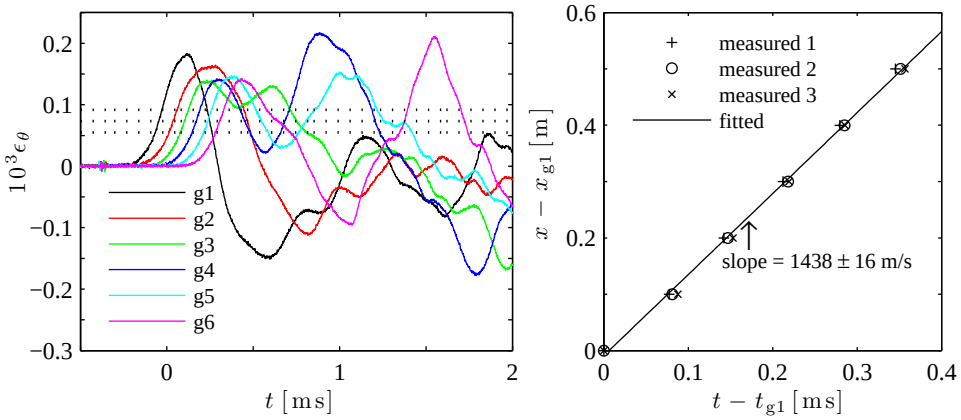

Figure 6.9: An example of the evolution of hoop strains without FSI (left) and the locations of the wave fronts (right). The dotted lines (in the left plot) denote the threshold values used to determine the wave fronts for the right plot.

relaxation time decreases as the initial buffer velocity increases. Since a stronger shock leads to a more violent bubble collapse, the buffer momentum may decay more rapidly due to bubble-dynamic energy dissipation. Note that if the relaxation time is longer than the time required for the shock to reach the last strain gauge (g6), the piston velocity will not change within the measurement period. In section 6.3.5, the shock speeds are calculated from the hoop strain measurements, and are compared to the predicted values (6.16) from the steady shock theory.

6.3.4 Precursory wave speeds

In order to verify the physical properties of the tube material, stress waves were generated by hammering the top of the tube and, with no water in the tube, wave speeds were computed. The evolution of the hoop strains and the calculated wave speeds are presented in figure 6.9. For comparative purposes, three threshold strain values (30, 40 and 50 percent of the maximum strain measured at the strain gauge g1) are used to determine the position of the wave front. Then, the wave speed was obtained from the slope of a linear least-squares fit to the wave front positions; the standard deviation of the slope was also computed. It transpires that the wave speed is fairly constant and the dispersion resulting from the thresholding is very small. Furthermore, the computed wave speed is found to agree with the theoretical value of $c_s = 1430$ m/s discussed in section 6.2.1. We also

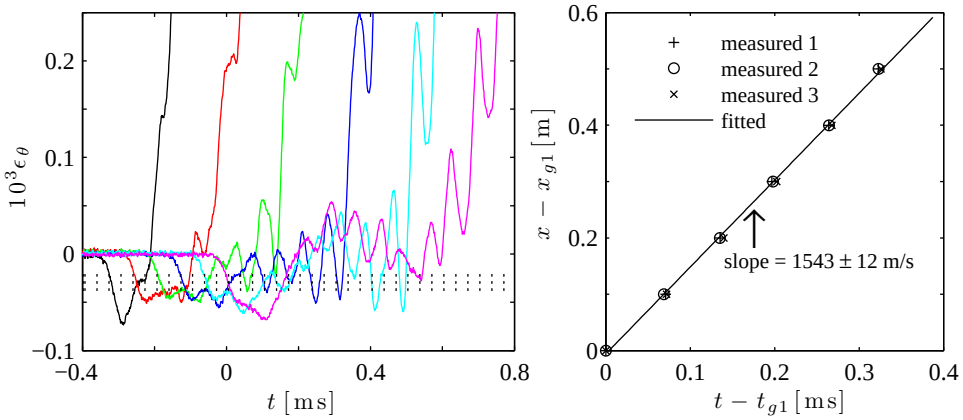

Figure 6.10: An example of the evolution of hoop strains with FSI (left) and the locations of the precursory wave fronts (right) for $H_p = 2$ m and $\alpha_0 = 0$. The dotted lines (in the left plot) denote the threshold values used to determine the wave fronts for the right plot.

note that within the measurement period, the error associated with the sampling rate (± 0.4 μs) or the inter-gauge distance (± 1 mm) is negligible compared to that of the thresholding.

We now examine the precursory waves for the tube filled with water. Figure 6.10 shows the precursory wave evolution and the wave front location for $H_p = 2$ m and $\alpha_0 = 0$. The thresholding is again based on 30, 40 and 50 percent of the minimum strain measured at g1. It is seen that the precursory waves travel slightly faster than the sonic speed, c_s, of the tube material and are followed by the primary waves. The wave structure becomes more oscillatory as time progresses. Wave dispersion results from structural oscillations in which the tube inertia comes into play (Skalak, 1956). It should be pointed out that the precursory wave front leads to contraction in the hoop direction as illustrated in figure 6.11. Behind the shock front, the shock pressure expands the tube in the radial direction. As a result of mass (or volume) conservation, the section in front of the shock needs to elongate in the axial direction. The resulting stresses propagate with a precursory wave speed that is close to the sonic speed of the tube material. Since the precursor propagates faster than the shock, the separation between the precursory and shock fronts expands and the dispersion grows as the waves evolve (see figure 6.10). In the early stage of this evolution, the dispersive effect may be ignored, and the elongation in the axial direction simply results in contraction because of the Poisson effect (in both the radial and hoop directions).

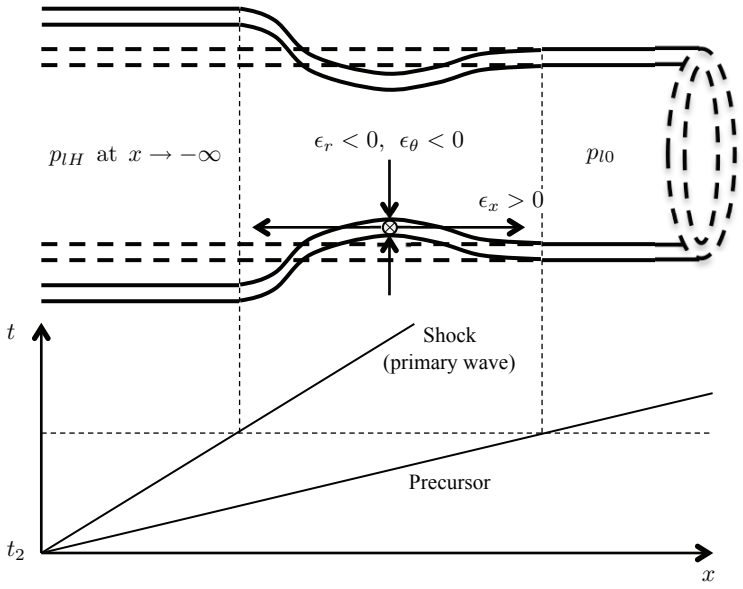

Figure 6.11: Illustration of the tube deformation (top) and the corresponding x–t diagram showing the relation of the precursory and primary waves (bottom).

6.3.5 Primary wave speeds

Here, we examine the shock (or primary) waves, which produce larger-amplitude hoop strains than the precursory waves. These water-hammer experiments are characterized by the drop height H_p and the initial void fraction α_0. To confirm repeatability in the measurements, three experimental runs were conducted for each case of H_p and α_0 as mentioned in section 6.3.3. In what follows, we choose some particular cases, and investigate the wave structures and the propagation speeds.

The evolution of the hoop strains for the case of $H_p = 2$ m and $\alpha_0 = 0$ is shown in figure 6.12 (left). Every strain gauge records the primary wave following a small-amplitude precursor. It also records a wave reflected from the tube bottom, and significant wave dispersion as seen in figure 6.10 (left). Moreover, the primary wave noticeably decays within the measurement period; thus the decay time is comparable to the relaxation time of the piston velocity computed in figure 6.8. Consequently, the unsteadiness of the buffer dynamics cannot be ignored.

In figure 6.12 (right), the primary wave speeds are computed as described in section 6.3.4. To determine the positions of the wave fronts, three different threshold strain levels are chosen (30,

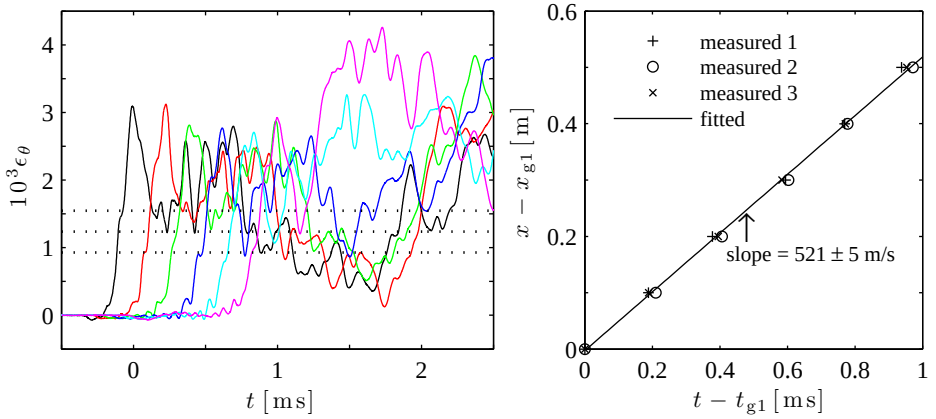

Figure 6.12: An example of the evolution of hoop strains with FSI (left) and the locations of the primary wave fronts (right) for $H_p = 2$ m and $\alpha_0 = 0$. The dotted lines (in the left plot) denote the threshold values used to determine the wave fronts for the right plot.

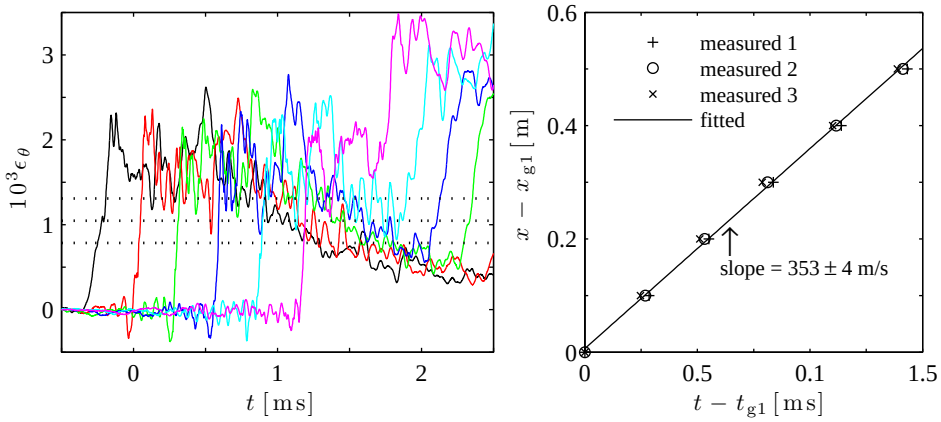

Figure 6.13: As figure 6.12, but with $H_p = 2$ m and $\alpha_0 = 0.0081$.

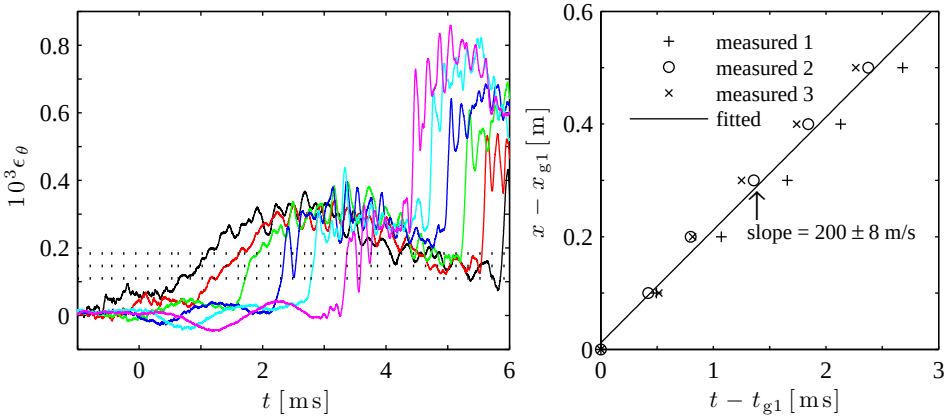

Figure 6.14: As figure 6.12, but with $H_p = 0.5$ m and $\alpha_0 = 0.0081$.

α_0^{mean}	0	0.0013	0.0024	0.0056	0.0081	0.010
$\Delta\alpha_0$	$\ll 1$	± 0.0001	± 0.0001	± 0.0001	± 0.0001	± 0.001
	521 ± 5	502 ± 1	459 ± 2	404 ± 2	353 ± 4	313 ± 2
$H_p = 2$ m	524 ± 2	499 ± 3	458 ± 1	386 ± 2	356 ± 2	329 ± 2
	524 ± 3	492 ± 2	475 ± 3	388 ± 1	356 ± 1	321 ± 2
	508 ± 4	477 ± 5	421 ± 13	259 ± 3	200 ± 8	168 ± 5
$H_p = 0.5$ m	524 ± 4	440 ± 9	385 ± 3	242 ± 4	201 ± 13	170 ± 5
	515 ± 5	446 ± 13	368 ± 3	257 ± 2	200 ± 10	183 ± 2

Table 6.1: Primary wave speeds [m/s] for various H_p and α_0. The error bounds in the wave speeds are standard deviations.

40 and 50 percent of the maximum strain measured at the strain gauge g1 before the reflected wave is observed). The computed speed (521 m/s) is in reasonable agreement with the Korteweg–Joukowsky wave speed ($c_{lJ} = 553$ m/s), and the the dispersion due to the thresholding is very small. This suggests that the linear theory is effectively valid for the case of pure water, even though the wave is dispersive and unsteady.

The bubbly water case ($H_p = 2$ m, $\alpha_0 = 0.0081$) is presented in figure 6.13. Now that the bubble dynamics play a role, the structural response manifests more complex structures than in the pure liquid case. The comparison of the figures 6.12 and 6.13 (left) reveals that the bubbles reduce the tube deformation. This is due to the fact that some fraction of the potential energy of the projectile is absorbed as bubble-dynamic work. Moreover, the wave speed is reduced by the bubbles. To further see the effect of the bubbles, the case of the lower drop height ($H_p = 0.5$ m, $\alpha_0 = 0.0081$) is presented in figure 6.14. In this case, the wave propagation is evidently unsteady. As pointed out in section 6.3.3, the wave due to the air compression propagates before the primary wave; the larger-amplitude primary wave catches up the preceding wave so that the wave front steepens as it evolves. The unsteadiness may also result from the fact that the relaxation time for the piston velocity and the measurement time are comparable. As a result of the unsteadiness, the threshold value becomes more critical, and the standard deviation in the computed wave speed becomes larger. We should note that the lower piston velocity reduces the wave speed. This is the effect of the gas-phase nonlinearity as pointed out in section 6.2.3.

The wave speeds are computed for each run, and are organized in table 6.1. The difference in

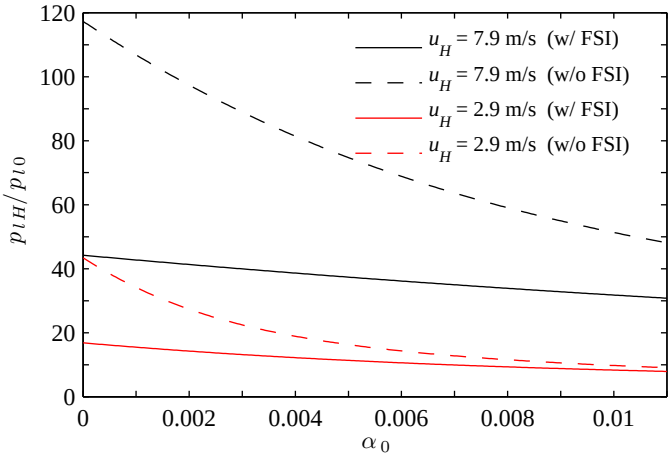

Figure 6.15: Estimated shock pressure as a function of α_0.

the wave speeds among the three runs is small. As expected, the wave speed decreases as the void fraction increases. Furthermore, for the cases with air injection, a reduction in the drop height of the projectile slows down the wave propagation.

We now compare the steady shock theory to the experimental data. Despite the unsteady buffer dynamics, we use the buffer velocity $\dot{x}_b(t_2) = 7.9$ m/s (or 2.9 m/s) for $H_p = 2$ m (or 0.5 m) to complete the steady shock relations in section 6.2.2. Since vapor pressure at the room temperature is negligible compared to the atmospheric pressure and surface tension may not be very important for the bubble sizes in the experiments, we neglect the vapor pressure and the surface tension (i.e., $p_v = 0$, $\Upsilon = 0$) in computing the shock relations. The theoretical shock pressure is presented in figure 6.15. The structural compressibility reduces the shock pressure because a part of the impact energy is absorbed into tube deformation. The bubble compressibility also dissipates energy so that the shock pressure decreases as the void fraction increases. Figure 6.16 compares the measured wave speeds to the theory including both the sonic and shock speeds. The error bars documented in table 6.1 are small and omitted for clarity. The measured speeds for the cases with air injection clearly show differences from the sonic speeds, and those for $H_p = 2$ m are larger than those for $H_p = 0.5$ m. These indicate the effect of the gas-phase nonlinearity on the wave speeds. The shock theory with FSI is found to more accurately capture the trend with increasing α_0 than the shock

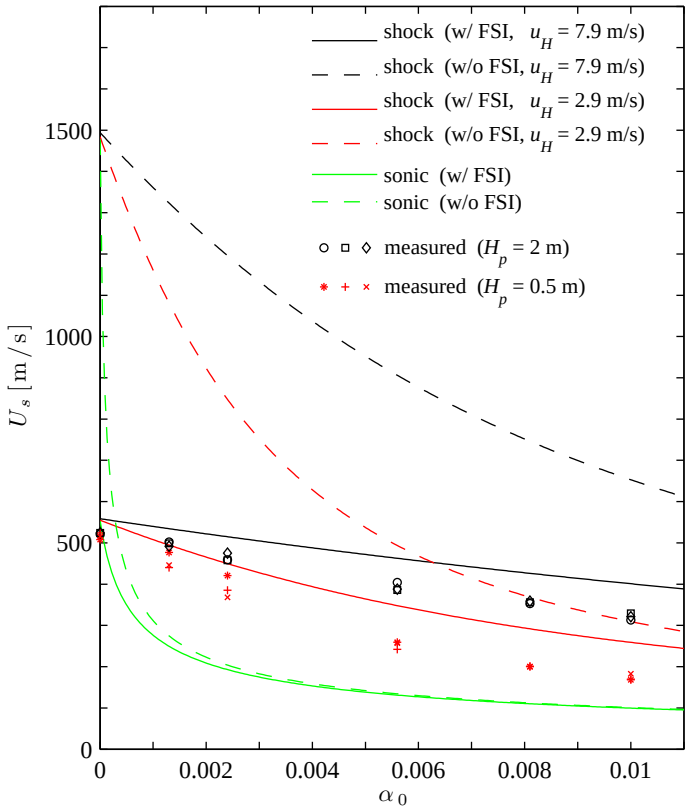

Figure 6.16: Theoretical and measured wave speeds as a function of α_0.

theory without FSI and the linear theory. It is therefore concluded that both FSI and the nonlinear effect need to be considered to accurately estimate the propagation speeds of finite-amplitude waves in mixture-filled pipes. However, the agreement between the present theory and the experiments is qualitative rather than quantitative.

Because the buffer (or piston) velocity considerably changes within the measurement period, it may be irrelevant to directly compare the measured wave speeds to the theoretical predictions with the assumption of constant piston velocities. Nonetheless, the differences between the measured wave speeds and the sonic speeds clearly indicate the need to take into account the gas-phase nonlinearity. We can say that the present FSI shock theory is the first step to include the nonlinear effect. The model limitations are discussed below to try to account for the discrepancy between the present theory and the experiments.

6.4 Model limitations

One of the most obvious limitations in the theory is related to the assumption of steady wave propagation. The strain evolution in figures 6.12 to 6.14 (left) demonstrates unsteady wave propagation in the sense that the piston velocity decays during the measurement period. Hence, the unsteadiness will degrade the model validity. If one quantifies the decay rate in the relaxation process, both the structural and the bubble-dynamic damping need to be included in the thoery. The viscoelasticity of the polycarbonate may affect the wave speed and damping (Meißner & Frank, 1977; Gally *et al.*, 1979; Suo & Wylie, 1990; Covas *et al.*, 2004). The unsteady wall friction may also have some impact on the relaxation (Bergant, 2001). If bubble fission occurs after passage of the shock (as in figure 6.6), the fission damping needs to be included in bubble-dynamic modeling (Brennen, 2002). Moreover, because polydispersity results in different frequency responses for different-sized bubbles, phase cancellations can cause an additional damping of the wave propagation.

Other limitations are the neglect of the tube inertia and the quasi-one-dimensional assumption. Since the waves are dispersive (due to the tube inertia) and of finite wave length, the wave speed as a function of the wave length cannot be accurately predicted by the current model. To quantify the effect of the tube inertia, a four-equation model describing both the fluid and the tube dynamics could be calculated (see for example Tijsseling, 1996).

6.5 Summary

A quasi-one-dimensional conservation law governing continuum bubbly flows in a deformable cylindrical tube was formulated based on the ensemble-averaged equations, and the steady shock relations were derived. The Korteweg–Joukowsky wave speed for the case of bubbly liquids was introduced, and the shock Mach number was formally defined. The modified bulk modulus of the mixture was introduced to reveal the importance of the gas-phase nonlinearity to shock propagation. The present FSI shock theory is found to be in better agreement with the measured wave speeds than the linear theory or the shock theory without FSI. This suggests that both FSI and the gas-phase nonlinearity

need to be taken into account to accurately predict the propagation speeds of finite-amplitude waves in bubbly-liquid-filled pipes.

Chapter 7

Concluding remarks

7.1 Summary and conclusions

The dynamics of bubbly flows with a distribution of equilibrium bubble sizes have been explored based on the continuum approach in order to quantify the effects of polydispersity on the average mixture dynamics. Fluid-structure interaction problems have also been considered to examine the coupling effects on the dynamics of cavitation clouds and shock propagation through a mixture-filled, deformable tube. The contributions and findings of this work can be summarized as follows.

The continuum bubbly flow equations incorporating nuclei size distributions were derived based on the ensemble-averaging technique. The single-bubble-dynamic model that includes the effects of thermal, viscous and acoustic damping was also introduced to close the continuum model. It was confirmed based on the ergodic hypothesis that the volume averages will be equivalent to the ensemble-averaged quantities if one appropriately chooses averaging volume under the scale separation assumption. One-way-coupling flow computations suggested that the different-sized bubbles oscillate with different frequencies and the phase cancellations can be regarded as an apparent damping of the averaged dynamics of polydisperse mixtures.

The high-order-accurate FV method and the time-marching scheme with the time-step splitting technique were developed and shown to accurately resolve wave dispersion and stiffness in continuum bubbly flows. For the present computations, the fifth-order monotonicity-preserving FV-WENO reconstruction is implemented in the characteristic space and the HLLC Riemann solver is used to

compute the numerical flux.

Numerical simulations of one-dimensional shock propagation in bubbly liquids were conducted. The steady shock relations were derived and used as the initial conditions. The comparison to the experiment of Kameda *et al.* (1998) demonstrated that the present model can accurately predict the oscillatory shock structure that appears in the monodisperse case. The numerical experiments showed that the averaged shock structure becomes less oscillatory as the bubble size distribution broadens. If the distribution is sufficiently broad, the shock profile is practically monotonic as experimentally identified by Beylich & Gülhan (1990). Because the different-sized bubbles can oscillate with different frequencies, phase cancellations in a polydisperse mixture occur locally. For the broad distribution case, the polydisperse cloud does not oscillate in volume due to the phase cancellations and can be regarded to behave quasistatically, regardless of single bubble dynamics. In this case, the effect of polydispersity dominates over the single-bubble-dynamic damping.

The dynamics of cavitation clouds caused by the structural interaction with an underwater shock were considered using the classical theories of Cole (1948) and Taylor (1950). Computations of one-dimensional cloud cavitation with monodisperse nuclei were performed to examine the inception and cloud collapse. The cavitation inception is shown to be sensitive to the rate of change in liquid pressure to negative values. If the decay time of the tension wave is sufficiently large, the inception can occur immediately after the pressure falls below the vapor pressure. It also transpires that the one-dimensional cloud collapse leads to oscillatory shock structures in the averaged liquid field but is not violent enough to produce strong shocks that can account for structural damage from the cavitation reloading. The case with polydipserse nuclei reveals that the phase cancellations with broad nuclei size distributions can eliminate violent collapse in the averaged dynamics.

The quasi-one-dimensional conservation law governing continuum bubbly flows in a deformable cylindrical tube was formulated, and the steady shock relations were derived. The modified bulk modulus of the mixture was introduced, and the nonlinear effect due to the gas-phase compressibility was shown to be important for finite-amplitude wave propagation. The present FSI shock theory was found to be in better agreement with the measured wave speeds than the linear theory or

the shock theory without FSI. This suggests that both FSI and the gas-phase nonlinearity need to be taken into account to accurately estimate the propagation speeds of finite-amplitude waves in bubbly-liquid-filled pipes.

7.2 Suggestions for future work

The present method has been shown to accurately capture the averaged dynamics of dilute bubbly flows in which direct interactions among the bubbles are negligible. The continuum bubbly flow model assumes cold liquids, indicating that the vapor pressure is small compared to the atmospheric pressure and the bubbles are inertially controlled (Brennen, 1995). The spherical-bubble assumption that implies no fission and coalescence of the bubbles is also employed for computational efficiency. However, these simplifications may be invalid in practice. The applicability of the continuum model needs to be extended for more accurate computations.

If a flow regime is disperse, the continuum approach may be applicable even to flows with high void fractions. One of the challenges is to take into account mutual interactions between the neighboring bubbles where local scattering due to the dynamics of individual bubbles can directly affect their neighbors. In this situation, there would be a need to modify a Rayleigh-Plesset-type equation to include the local scattering effect.

In the case of hot liquids (close to the boiling point), the liquid-phase thermodynamics will come into play, and the mixture-averaged energy equation needs to be solved. It is also necessary to develop a computational technique to efficiently and properly predict the damping of the dynamics of thermally controlled bubbles for practical purposes. This extension will be of significant importance to cavitating flow computations in rocket engines.

The fission of collapsing bubbles often occurs in many situations. Once the fission is permitted in the modeling, the bubble number conservation does not hold. For engineering applications, a simple model for the fission damping may be needed in the framework of Rayleigh-Plesset-type computations (Brennen, 2002).

Appendix A

Derivation of mixture-averaged equations

In this appendix, the ensemble-averaged technique of Zhang & Prosperetti (1994) is reviewed in sections A.1 and A.2, and the derivation of the mixture-averaged equations for polydisperse bubbly flows with a model closure is presented in section A.3.

A.1 Preliminaries

A.1.1 Probability function

Consider an ensemble of N spherical bubbles in polydisperse bubbly flows arranged in a time-dependent configuration, $\mathcal{C}^N$, that is defined as a set of quantities sufficient to uniquely specify the dynamical state of the system at time t. The configuration may be defined as

> a set of bubble centers $\mathbf{y}^{(i)}$, (current) radius $R^{(i)}$, equilibrium radius $R_0^{(i)}$, particle velocity $\mathbf{w}^{(i)}$ and bubble wall velocity $\dot{R}^{(i)}$ where $i = 1, 2, \ldots, N$.

Because the ensemble consists of a large number of realizations, it is convenient to introduce a probability function, $\mathcal{P}(\mathcal{C}^N; t) \equiv \mathcal{P}(N; t)$, to specify each realization. Specifically,

$$\begin{aligned}\mathcal{P}(N;t)\, d\mathcal{C}^N \equiv \mathcal{P}(N;t)\, d^3y^{(1)}\, dR^{(1)}\, dR_0^{(1)}\, d^3w^{(1)}\, d\dot{R}^{(1)} \\ \times \cdots d^3y^{(N)}\, dR^{(N)}\, dR_0^{(N)}\, d^3w^{(N)}\, d\dot{R}^{(N)}\end{aligned} \tag{A.1}$$

represents the probability of finding, at time t, a realization in which the state of the first bubble is within $d^3y^{(1)}$ of $\mathbf{y}^{(1)}$, etc. Provided that fission and coalescence of the bubbles do not occur, the probability function is conserved in time:

$$\frac{\partial \mathcal{P}}{\partial t} + \sum_{i=1}^{N} \left[\nabla_{\mathbf{y}^{(i)}} \cdot \left(\mathbf{w}^{(i)} \mathcal{P} \right) + \frac{\partial}{\partial R^{(i)}} \left(\dot{R}^{(i)} \mathcal{P} \right) + \nabla_{\mathbf{w}^{(i)}} \cdot \left(\dot{\mathbf{w}}^{(i)} \mathcal{P} \right) + \frac{\partial}{\partial \dot{R}^{(i)}} \left(\ddot{R}^{(i)} \mathcal{P} \right) \right] = 0, \tag{A.2}$$

where the dot denotes the substantial derivative. Note that the term associated with $R_0^{(i)}$ drops out due to the insoluble gas assumption. A convenient normalization is

$$\int d\mathcal{C}^N \, \mathcal{P}(N;t) = N!, \tag{A.3}$$

with the integration over the complete range for each variable.

The reduced probability in which the configuration of the first K bubbles is prescribed is

$$\mathcal{P}(K;t) = \frac{1}{(N-K)!} \int d\mathcal{C}^{N-K} \, \mathcal{P}(N;t), \tag{A.4}$$

where the integration is taken over the configuration of the last $N-K$ bubbles. It follows from equation (A.3) that

$$\int d\mathcal{C}^K \, \mathcal{P}(K;t) = \frac{N!}{(N-K)!}. \tag{A.5}$$

Especially, the one-bubble probability function, $\mathcal{P}(1;t) \equiv \mathcal{P}(\mathbf{y}, R, R_0, \mathbf{w}, \dot{R}; t)$, satisfies

$$\int d^3y \, dR \, dR_0 \, d^3w \, d\dot{R} \, \mathcal{P}(1;t) = N, \tag{A.6}$$

so that the bubble number density per unit volume of the mixture is formally defined as

$$n(\mathbf{y}, t) = \int dR \, dR_0 \, d^3w \, d\dot{R} \, \mathcal{P}(1;t). \tag{A.7}$$

The conditional probability of having the last $N-K$ bubbles in a certain configuration, given that the configuration of the first K bubbles is specified, is defined as

$$\mathcal{P}(N-K|K;t) = \frac{\mathcal{P}(N;t)}{\mathcal{P}(K;t)}, \tag{A.8}$$

and is subject to the normalization,

$$\int d\mathcal{C}^{N-K}\, \mathcal{P}(N-K|K;t) = (N-K)!, \tag{A.9}$$

in consequence of equations (A.3), (A.5) and (A.8).

By averaging equation (A.2) over the configuration of the last $N-K$ bubbles, we find

$$\begin{aligned}\frac{\partial \mathcal{P}(K;t)}{\partial t} + \sum_{i=1}^{K} \Bigg[\nabla_{\mathbf{y}^{(i)}} \cdot \left(\mathbf{w}^{(i)} \mathcal{P}(K;t) \right) + \frac{\partial}{\partial R^{(i)}} \left(\dot{R}^{(i)} \mathcal{P}(K;t) \right) \\ + \nabla_{\mathbf{w}^{(i)}} \cdot \left(\left\langle \left\langle \dot{\mathbf{w}}^{(i)} \right\rangle \right\rangle_K \mathcal{P}(K;t) \right) + \frac{\partial}{\partial \dot{R}^{(i)}} \left(\left\langle \left\langle \ddot{R}^{(i)} \right\rangle \right\rangle_K \mathcal{P}(K;t) \right) \Bigg] = 0,\end{aligned} \tag{A.10}$$

where $\langle\langle \cdot \rangle\rangle_K$ is defined as

$$\left\langle \left\langle \dot{\mathbf{w}}^{(i)} \right\rangle \right\rangle_K = \frac{1}{(N-K)!} \int d\mathcal{C}^{N-K}\, \mathcal{P}(N-K|K;t)\, \dot{\mathbf{w}}^{(i)}, \tag{A.11}$$

$$\left\langle \left\langle \ddot{R}^{(i)} \right\rangle \right\rangle_K = \frac{1}{(N-K)!} \int d\mathcal{C}^{N-K}\, \mathcal{P}(N-K|K;t)\, \ddot{R}^{(i)}. \tag{A.12}$$

Assumimg that $\mathcal{P}$ vanishes in the integration limits, we can derive the bubble number density conservation with the aid of equations (A.7) and (A.10):

$$\frac{\partial n}{\partial t} + \nabla_{\mathbf{y}} \cdot (n \overline{\mathbf{w}}) = 0, \tag{A.13}$$

where the mean particle velocity, $\overline{\mathbf{w}}$, is

$$\overline{\mathbf{w}}(\mathbf{y},t) = \frac{1}{n(\mathbf{y},t)} \int dR\, dR_0\, d^3w\, d\dot{R}\, \mathcal{P}(1;t)\mathbf{w}. \tag{A.14}$$

A.1.2 Volume fractions

To formally define volume fractions of each phase, we introduce the indicator function of the disperse phase:

$$\zeta_D(\mathbf{x}; N) = \sum_{i=1}^{N} H\left(R^{(i)} - \left|\mathbf{x} - \mathbf{y}^{(i)}\right|\right). \tag{A.15}$$

The indicator function of the continuous phase is then given by $\zeta_C(\mathbf{x}; N) = 1 - \zeta_D(\mathbf{x}; N)$. Note that ζ_D and ζ_C are geometrical entities that depend on time only indirectly through the time evolution of the configuration. For future reference, the gradients of ζ_C are written as

$$\nabla\zeta_C = \sum_{i=1}^{N} \delta\left(R^{(i)} - \left|\mathbf{x} - \mathbf{y}^{(i)}\right|\right) \frac{\mathbf{x} - \mathbf{y}^{(i)}}{R^{(i)}}, \tag{A.16}$$

$$\nabla_{\mathbf{y}^{(i)}}\zeta_C = -\delta\left(R^{(i)} - \left|\mathbf{x} - \mathbf{y}^{(i)}\right|\right) \frac{\mathbf{x} - \mathbf{y}^{(i)}}{R^{(i)}}, \tag{A.17}$$

$$\frac{\partial\zeta_C}{\partial R^{(i)}} = -\delta\left(R^{(i)} - \left|\mathbf{x} - \mathbf{y}^{(i)}\right|\right), \tag{A.18}$$

where $\nabla \equiv \nabla_{\mathbf{x}} = (\partial/\partial x_1, \partial/\partial x_2, \partial/\partial x_3)^T$.

The volume fractions of the phases are defined as averages of the indicator functions over the probability $\mathcal{P}(N; t)$:

$$\alpha_C(\mathbf{x}, t) = \frac{1}{N!} \int d\mathcal{C}^N \, \mathcal{P}(N; t)\, \zeta_C(\mathbf{x}; N), \tag{A.19}$$

$$\alpha_D(\mathbf{x}, t) = \frac{1}{N!} \int d\mathcal{C}^N \, \mathcal{P}(N; t)\, \zeta_D(\mathbf{x}; N). \tag{A.20}$$

The definition (A.20) with the indicator function (A.15) gives

$$\alpha_D(\mathbf{x}, t) = 1 - \alpha_C(\mathbf{x}, t) = \int dR \int_{|\mathbf{x}-\mathbf{y}|\leq R} d^3y \int dR_0 \, d^3w \, d\dot{R} \, \mathcal{P}(1; t). \tag{A.21}$$

The volume fraction of the disperse phase, α_D, is generally called *void fraction*.

A.2 Ensemble phase averaging

A.2.1 Continuous-phase averaging

Averages of field quantities pertaining to the continuus phase are defined as

$$\langle f_C \rangle(\mathbf{x}, t) = \frac{1}{N! \alpha_C} \int d\mathcal{C}^N \, \mathcal{P}(N; t) \, \zeta_C(\mathbf{x}; N) \, f_C(\mathbf{x}, t; N). \tag{A.22}$$

The conditional averages with K bubbles fixed are

$$\langle f_C \rangle_K(\mathbf{x}, t|K) = \frac{1}{(N-K)! \alpha_{C,K}} \int d\mathcal{C}^{N-K} \, \mathcal{P}(N-K|K; t) \, \zeta_C(\mathbf{x}; N) \, f_C(\mathbf{x}, t; N). \tag{A.23}$$

We first derive the expression for the gradient of $\langle f_C \rangle$. From equation (A.16), we find

$$\begin{aligned} \nabla\big(\alpha_C \langle f_C \rangle\big) &= \frac{1}{N!} \int d\mathcal{C}^N \, \mathcal{P}(N; t) \left[\zeta_C \nabla f_C + f_C \nabla \zeta_C \right] \\ &= \alpha_C \langle \nabla f_C \rangle + \frac{1}{N!} \int d\mathcal{C}^N \, \mathcal{P}(N; t) \, f_C \sum_{i=1}^{N} \delta\left(R^{(i)} - \left| \mathbf{x} - \mathbf{y}^{(i)} \right| \right) \frac{\mathbf{x} - \mathbf{y}^{(i)}}{R^{(i)}}. \end{aligned} \tag{A.24}$$

Assuming that each term of the summation in equation (A.24) gives the same contribution and using the conditional probability (A.8) with $K = 1$, equation (A.24) becomes

$$\begin{aligned} \nabla\big(\alpha_C \langle f_C \rangle\big) &= \alpha_C \langle \nabla f_C \rangle + \frac{1}{(N-1)!} \int d\mathcal{C}^N \, \mathcal{P}(N; t) \, f_C \, \delta\left(R^{(1)} - \left| \mathbf{x} - \mathbf{y}^{(1)} \right| \right) \frac{\mathbf{x} - \mathbf{y}^{(1)}}{R^{(1)}} \\ &= \alpha_C \langle \nabla f_C \rangle + \int d\mathcal{C}^{(1)} \, \mathcal{P}(1; t) \, \delta\left(R^{(1)} - \left| \mathbf{x} - \mathbf{y}^{(1)} \right| \right) \frac{\mathbf{x} - \mathbf{y}^{(1)}}{R^{(1)}} \\ &\quad \times \int d\mathcal{C}^{N-1} \, \mathcal{P}(N-1|1; t) \, f_C. \end{aligned} \tag{A.25}$$

Noting that in evaluating the delta function, $\mathbf{x}$ must be taken on the bubble wall in the continuous phase ($\zeta_C = 1$, $\alpha_{C,1} = 1$) and using the definition (A.23) with $K = 1$, equation (A.25) can be written

as

$$\nabla\big(\alpha_C\langle f_C\rangle\big) = \alpha_C\langle\nabla f_C\rangle + \int dR \int_{|\mathbf{x}-\mathbf{y}|=R} dS_y\, \mathbf{n}_y \int dR_0\, d^3w\, d\dot{R}\, \mathcal{P}(1;t)\, \langle f_C\rangle_1(\mathbf{x},t|1), \tag{A.26}$$

where $\mathbf{n}_y$ is the unit normal directed out of the bubble. Note that the integration in the above equation is taken over all the bubbles that touch the fixed point $\mathbf{x}$. If taking $f_C = 1$, then we obtain

$$\nabla\alpha_C = \int dR \int_{|\mathbf{x}-\mathbf{y}|=R} dS_y\, \mathbf{n}_y \int dR_0\, d^3w\, d\dot{R}\, \mathcal{P}(1;t) = \int dR \int_{|\mathbf{x}-\mathbf{y}|=R} dS_y\, \mathbf{n}_y\, n(\mathbf{y},t). \tag{A.27}$$

From equation (A.27), equation (A.26) is equivalently written as

$$\begin{aligned}\nabla\langle f_C\rangle &= \langle\nabla f_C\rangle \\ &\quad + \frac{1}{\alpha_C}\int dR \int_{|\mathbf{x}-\mathbf{y}|=R} dS_y\, \mathbf{n}_y \int dR_0\, d^3w\, d\dot{R}\, \mathcal{P}(1;t)\big[\langle f_C\rangle_1(\mathbf{x},t|1) - \langle f_C\rangle(\mathbf{x},t)\big].\end{aligned} \tag{A.28}$$

This relation shows that averaging and spatial differentiation do not commute.

We also derive the expression for the time derivative of $\langle f_C\rangle$. From the definition (A.22),

$$\frac{\partial}{\partial t}\big(\alpha_C\langle f_C\rangle\big) = \frac{1}{N!}\int d\mathcal{C}^N \left[\mathcal{P}(N;t)\frac{\hat{\partial} f_C}{\hat{\partial} t} + f_C\frac{\partial\mathcal{P}(N;t)}{\partial t}\right]\zeta_C(\mathbf{x};N), \tag{A.29}$$

where $\hat{\partial}/\hat{\partial}t$ is the partial time derivative with fixed $\mathbf{x}$ and $\mathcal{C}^N$. Substitution of equation (A.2) and integration by parts yield

$$\frac{\partial}{\partial t}\big(\alpha_C\langle f_C\rangle\big) = \alpha_C\left\langle\frac{\partial f_C}{\partial t}\right\rangle + \frac{1}{N!}\int d\mathcal{C}^N\, \mathcal{P}(N;t)\, f_C \sum_{i=1}^{N}\left(\mathbf{w}^{(i)}\cdot\nabla_{\mathbf{y}^{(i)}}\zeta_C + \dot{R}^{(i)}\frac{\partial\zeta_C}{\partial R^{(i)}}\right). \tag{A.30}$$

Substituting equations (A.17) and (A.18) into equation (A.30), we obtain

$$\frac{\partial}{\partial t}\big(\alpha_C\langle f_C\rangle\big) = \alpha_C\left\langle\frac{\partial f_C}{\partial t}\right\rangle - \int dR \int_{|\mathbf{x}-\mathbf{y}|=R} dS_y \int dR_0\, d^3w\, d\dot{R}\left(\mathbf{w}\cdot\mathbf{n}_y + \dot{R}\right)\mathcal{P}(1;t)\langle f_C\rangle_1. \tag{A.31}$$

For $f_C = 1$, the above equation reduces to

$$\frac{\partial \alpha_C}{\partial t} = -\int dR \int_{|\mathbf{x}-\mathbf{y}|=R} dS_y \int dR_0\, d^3w\, d\dot{R} \left(\mathbf{w}\cdot\mathbf{n}_y + \dot{R}\right) \mathcal{P}(1;t), \tag{A.32}$$

so that equation (A.31) can be rewritten as

$$\begin{aligned}\frac{\partial \langle f_C\rangle}{\partial t} &= \left\langle \frac{\partial f_C}{\partial t}\right\rangle \\ &\quad - \frac{1}{\alpha_C}\int dR \int_{|\mathbf{x}-\mathbf{y}|=R} dS_y \int dR_0\, d^3w\, d\dot{R} \left(\mathbf{w}\cdot\mathbf{n}_y + \dot{R}\right) \mathcal{P}(1;t)\big[\langle f_C\rangle_1 - \langle f_C\rangle\big].\end{aligned} \tag{A.33}$$

This suggests that averaging and time differentiation do not commute.

At this stage, we can derive a transport theorem that applies for the derivation of the mixture-averaged equations. Let $\mathbf{u}_C$ be the velocity of the continuous phase. From equations (A.26) and (A.31), we find

$$\begin{aligned}\frac{\partial}{\partial t}\big(\alpha_C\langle f_C\rangle\big) + \nabla\cdot\big(\alpha_C\langle f_C\mathbf{u}_C\rangle\big) &= \alpha_C\left\langle \frac{\partial f_C}{\partial t} + \nabla\cdot(f_C\mathbf{u}_C)\right\rangle - \int dR \int_{|\mathbf{x}-\mathbf{y}|=R} dS_y \\ &\quad \times \int dR_0\, d^3w\, d\dot{R}\, \mathcal{P}(1;t)\left[\left(\mathbf{w}\cdot\mathbf{n}_y + \dot{R}\right)\langle f_C\rangle_1 - \mathbf{n}_y\cdot\langle f_C\mathbf{u}_C\rangle_1\right].\end{aligned} \tag{A.34}$$

At the bubble interfaces, the velocity field must satisfy the kinematic boundary condition,

$$\mathbf{w}\cdot\mathbf{n}_y + \dot{R} = \mathbf{n}_y\cdot\mathbf{u}_C(\mathbf{x},t;N). \tag{A.35}$$

It follows from definition (A.23) that

$$\left(\mathbf{w}\cdot\mathbf{n}_y + \dot{R}\right)\langle f_C\rangle_1 = \left\langle \left(\mathbf{w}\cdot\mathbf{n}_y + \dot{R}\right) f_C\right\rangle_1, \tag{A.36}$$

$$\mathbf{n}_y\cdot\langle f_C\mathbf{u}_C\rangle_1 = \langle f_C\mathbf{n}_y\cdot\mathbf{u}_C\rangle_1. \tag{A.37}$$

As a result, the integral term in equation (A.34) identically vanishes; namely

$$\frac{\partial}{\partial t}\big(\alpha_C\langle f_C\rangle\big) + \nabla\cdot\big(\alpha_C\langle f_C\mathbf{u}_C\rangle\big) = \alpha_C\left\langle\frac{\partial f_C}{\partial t} + \nabla\cdot(f_C\mathbf{u}_C)\right\rangle. \tag{A.38}$$

A special case, $f_C = 1$, gives the evolution equation for α_C:

$$\frac{\partial\alpha_C}{\partial t} + \nabla\cdot\big(\alpha_C\langle\mathbf{u}_C\rangle\big) = \alpha_C\langle\nabla\cdot\mathbf{u}_C\rangle. \tag{A.39}$$

A.2.2 Disperse-phase averaging

When it comes to dealing with the disperse phase, we introduce particle averaging for quantities associated with the bubbles, such as particle velocity, bubble radius and bubble wall velocity. Let $\varphi^{(i)}(N;t)$ be such quantities where the notation implies that the value of φ for the bubble i generally depends on the entire configuration. We define the ensemble average for φ:

$$n\overline{\varphi}(\mathbf{x},t) = \frac{1}{N!}\int d\mathcal{C}^N\,\mathcal{P}(N;t)\sum_{i=1}^{N}\delta\left(\mathbf{x}-\mathbf{y}^{(i)}\right)\varphi^{(i)}(N;t). \tag{A.40}$$

Assuming that each bubble has the same contribution to the summation, the above relation reduces to

$$\overline{\varphi}(\mathbf{x},t) = \frac{1}{n}\frac{1}{(N-1)!}\int d\mathcal{C}^1\,\mathcal{P}(1;t)\delta\left(\mathbf{x}-\mathbf{y}^{(1)}\right)\int d\mathcal{C}^{N-1}\,\mathcal{P}(N-1|1;t)\varphi^{(1)}(N;t). \tag{A.41}$$

Suppose that $\varphi^{(1)}$ does not depend explicitly on the configuration of the other bubbles ($i\neq 1$), we find

$$\overline{\varphi}(\mathbf{x},t) = \frac{1}{n}\int dR^{(1)}\,dR_0^{(1)}\,d^3w^{(1)}\,d\dot{R}^{(1)}\,\mathcal{P}(1;t)\varphi^{(1)}(1;t). \tag{A.42}$$

According to the property of the delta function in equation (A.40), $\mathcal{P}$ and $\varphi^{(1)}$ are functions of $\mathbf{x}$, not $\mathbf{y}$. Notice that the mean particle velocity, $\overline{\mathbf{w}}$, defined in equation (A.14) is a special case for this

definition. We also define the average associated with bubbles of radius R,

$$\overline{\varphi}_R(\mathbf{x},t) = \frac{1}{n_R}\int dR_0^{(1)}\, d^3w^{(1)}\, d\dot{R}^{(1)}\, \mathcal{P}(1;t)\varphi^{(1)}(1;t), \tag{A.43}$$

where n_R is the number density of bubbles of radius R,

$$n_R(\mathbf{y},R,t) = \int dR_0^{(1)}\, d^3w^{(1)}\, d\dot{R}^{(1)}\, \mathcal{P}(1;t). \tag{A.44}$$

Note that according to this definition, $\overline{R}_R = R$. Also note that $\overline{\varphi}$ and $\overline{\varphi}_R$ are related by

$$n\overline{\varphi}(\mathbf{x},t) = \int dR^{(1)}\, n_R\, \overline{\varphi}_R(\mathbf{x},R,t). \tag{A.45}$$

From definition (A.43), we calculate the partial time derivative of $n_R\overline{\varphi}_R$ as

$$\begin{aligned}\frac{\partial}{\partial t}\left(n_R\overline{\varphi}_R\right) &= \int dR_0^{(1)}\, d^3w^{(1)}\, d\dot{R}^{(1)} \left[\mathcal{P}(1;t)\frac{\hat{\partial}\varphi^{(1)}}{\hat{\partial}t} + \varphi^{(1)}\frac{\partial\mathcal{P}(1;t)}{\partial t}\right] \\ &= n_R\overline{\left(\frac{\hat{\partial}\varphi^{(1)}}{\hat{\partial}t}\right)}_R - \int dR_0^{(1)}\, d^3w^{(1)}\, d\dot{R}^{(1)}\, \varphi^{(1)}\left[\nabla\cdot\left(\mathbf{w}^{(1)}\mathcal{P}(1;t)\right)\right. \\ &\quad \left. + \frac{\partial\dot{R}^{(1)}\mathcal{P}(1;t)}{\partial R^{(1)}} + \nabla_{\mathbf{w}^{(1)}}\cdot\left(\left\langle\left\langle\dot{\mathbf{w}}^{(1)}\right\rangle\right\rangle_1\mathcal{P}(1;t)\right) + \frac{\partial\left\langle\left\langle\ddot{R}^{(1)}\right\rangle\right\rangle_1\mathcal{P}(1;t)}{\partial\dot{R}^{(1)}}\right].\end{aligned} \tag{A.46}$$

Because we assume that $\dot{\mathbf{w}}^{(1)}$ and $\ddot{R}^{(1)}$ do not depend explicitly on the configuration of the other bubbles ($i \neq 1$), the relations, $\left\langle\left\langle\dot{\mathbf{w}}^{(1)}\right\rangle\right\rangle_1 = \dot{\mathbf{w}}^{(1)}$ and $\left\langle\left\langle\ddot{R}^{(1)}\right\rangle\right\rangle_1 = \ddot{R}^{(1)}$, hold. Integration by parts leads to

$$\frac{\partial}{\partial t}\left(n_R\overline{\varphi}_R\right) + \nabla\cdot\left(n_R\overline{(\varphi\mathbf{w})}_R\right) + \frac{\partial}{\partial R}\left(n_R\overline{\left(\varphi\dot{R}\right)}_R\right) = n_R\overline{\left(\frac{\partial\varphi^{(1)}}{\partial t}\right)}_R, \tag{A.47}$$

where $\partial\varphi^{(1)}/\partial t$ is given by

$$\frac{\partial\varphi^{(1)}}{\partial t} = \frac{\hat{\partial}\varphi^{(1)}}{\hat{\partial}t} + \mathbf{w}^{(1)}\cdot\nabla\varphi^{(1)} + \dot{R}^{(1)}\frac{\partial\varphi^{(1)}}{\partial R^{(1)}} + \dot{\mathbf{w}}^{(1)}\cdot\nabla_{\mathbf{w}^{(1)}}\varphi^{(1)} + \ddot{R}^{(1)}\frac{\partial\varphi^{(1)}}{\partial\dot{R}^{(1)}}. \tag{A.48}$$

By integrating equation (A.47) over R from 0 to ∞, we finally find

$$\frac{\partial}{\partial t}\left(n\overline{\varphi}\right) + \nabla\cdot\left(n\overline{\varphi\mathbf{w}}\right) = n\overline{\left(\frac{\partial\varphi^{(1)}}{\partial t}\right)}. \tag{A.49}$$

A.3 Ensemble-averaged equations

A.3.1 Continuity and momentum equations

In order to derive the ensemble-averaged Euler equations for dilute bubbly flows, mixture density and momentum are defined as

$$\langle\rho\rangle = \alpha_C\langle\rho_C\rangle, \tag{A.50}$$

$$\langle\rho\mathbf{u}\rangle = \alpha_C\langle\rho_C\mathbf{u}_C\rangle. \tag{A.51}$$

Substitution of $f_C = \rho_C$ and $\rho_C\mathbf{u}_C$ into equation (A.38) yields

$$\frac{\partial\langle\rho\rangle}{\partial t} + \nabla\cdot\langle\rho\mathbf{u}\rangle = 0, \tag{A.52}$$

$$\frac{\partial\langle\rho\mathbf{u}\rangle}{\partial t} + \nabla\cdot\langle\rho\mathbf{u}\mathbf{u}\rangle = -\nabla\big(\alpha_C\langle p_C\rangle\big) + \alpha_C\mathbf{A}_C, \tag{A.53}$$

where $\alpha_C\mathbf{A}_C$ is given by equation (A.26):

$$\alpha_C\mathbf{A}_C = \int dR\int_{|\mathbf{x}-\mathbf{y}|=R} dS_y\,\mathbf{n}_y\int dR_0\,d^3w\,d\dot{R}\,\mathcal{P}(1;t)\langle p_C\rangle_1. \tag{A.54}$$

The correlations such as $\langle\rho\mathbf{u}\rangle$ and $\langle\rho\mathbf{u}\mathbf{u}\rangle$ in equations (A.52) and (A.53) need to be expressed in terms of $\langle\rho\rangle$ and $\langle\mathbf{u}\rangle$. Because the velocity fluctuations caused by the bubble dynamics concentrate in the vicinity of the bubbles, where the liquid is effectively incompressible (Prosperetti & Lezzi,

1986), the density and velocity fluctuations can be assumed uncorrelated:

$$\langle \rho \mathbf{u} \rangle = \underbrace{\alpha_C \langle \rho_C \rangle}_{\langle \rho \rangle} \langle \mathbf{u}_C \rangle = \langle \rho \rangle \langle \mathbf{u} \rangle, \tag{A.55}$$

where $\langle \mathbf{u} \rangle = \langle \mathbf{u}_C \rangle$. Moreover, we introduce the kinematic Reynolds stress tensor,

$$\mathbf{M}_C = \langle \mathbf{u}_C \rangle \langle \mathbf{u}_C \rangle - \langle \mathbf{u}_C \mathbf{u}_C \rangle = -\Big\langle \big(\mathbf{u}_C - \langle \mathbf{u}_C \rangle\big)\big(\mathbf{u}_C - \langle \mathbf{u}_C \rangle\big) \Big\rangle. \tag{A.56}$$

As a direct consequence, the continuity and momentum equations are rewritten as

$$\frac{\partial \langle \rho \rangle}{\partial t} + \nabla \cdot \big(\langle \rho \rangle \langle \mathbf{u} \rangle \big) = 0, \tag{A.57}$$

$$\frac{\partial \langle \rho \rangle \langle \mathbf{u} \rangle}{\partial t} + \nabla \cdot \big(\langle \rho \rangle \langle \mathbf{u} \rangle \langle \mathbf{u} \rangle + \alpha_C \langle p_C \rangle \mathbf{I} \big) = \alpha_C \mathbf{A}_C + \nabla \cdot \big(\langle \rho \rangle \mathbf{M}_C \big), \tag{A.58}$$

where $\mathbf{I}$ is an identity tensor.

When computing the vector quantity $\alpha_C \mathbf{A}_C$, we need to evaluate the integration over all the bubbles that touch the fixed point $\mathbf{x}$. For convenience, we prefer to use the integration over the surface of a fixed bubble (Zhang & Prosperetti, 1997) rather than directly use the exact definition (A.54). Let $\mathbf{r} = \mathbf{x} - \mathbf{y}$ and we introduce

$$\mathcal{F}(\mathbf{r}, \mathbf{y}) \equiv \mathcal{P}(1; t) \langle p_C \rangle_1 (\mathbf{y} + \mathbf{r}, t | 1), \tag{A.59}$$

where the argument 1 denotes configuration ($\mathbf{y}$, R, R_0, $\mathbf{w}$, $\dot{R}$). Assuming that the probability function and the ensemble-averaged continuous-phase pressure do not show a rapid change in space, $\mathcal{F}$ may be expanded using Taylor's theorem centered at $\mathbf{x}$:

$$\mathcal{F}(\mathbf{r}, \mathbf{y}) = \mathcal{F}(\mathbf{r}, \mathbf{x}) - \mathbf{r} \cdot \nabla \mathcal{F}(\mathbf{r}, \mathbf{x} - \mathbf{h}). \tag{A.60}$$

Here, we employ the Lagrange form of the remainder with $|\mathbf{h}| < R$. If the bubble sizes are suffi-

ciently small compared to typical wavelengths in the averaged field, we can reasonably take $\mathbf{h} = \mathbf{0}$. Substitution of equation (A.60) into equation (A.54) gives

$$\alpha_C \mathbf{A}_C = \alpha_D \mathcal{A}[p_C] - \nabla \cdot \big(\alpha_D \mathcal{L}[p_C]\big), \tag{A.61}$$

where $\mathcal{A}$ and $\mathcal{L}$ are given by

$$\alpha_D \mathcal{A}[p_C] = \int dR_0\, d^3w\, d\dot{R} \int dR\, \mathcal{P}(1;t) \int_{|\mathbf{z}-\mathbf{x}|=R} dS_z\, \mathbf{n}_z \langle p_C \rangle_1(\mathbf{z}, t|1), \tag{A.62}$$

$$\alpha_D \mathcal{L}[p_C] = \int dR_0\, d^3w\, d\dot{R} \int dR\, \mathcal{P}(1;t)\, R \int_{|\mathbf{z}-\mathbf{x}|=R} dS_z\, \mathbf{n}_z\, \mathbf{n}_z \langle p_C \rangle_1(\mathbf{z}, t|1). \tag{A.63}$$

Here, the argument 1 denotes configuration ($\mathbf{x}$, R, R_0, $\mathbf{w}$, $\dot{R}$). It is now clear that the integration for $\alpha_D \mathcal{A}$ and $\alpha_D \mathcal{L}$ is taken over the surface of a bubble centered at $\mathbf{x}$.

The pressure in the continuous phase, p_C, is generally a function of the configurations of the N bubbles. However, in the dilute limit, direct interactions among the bubbles may be minimized and the bubble wall pressure ($p_{bw} = p_C|_{|\mathbf{z}-\mathbf{x}|=R^+}$) may depend only on the configuration of a bubble centered at $\mathbf{x}$. As a result, we find

$$\langle p_C \rangle_1(\mathbf{z}, t|1)\big|_{|\mathbf{z}-\mathbf{x}|=R^+} = p_{bw}(\mathbf{z}, t|1). \tag{A.64}$$

Since the bubbles are spherical, the bubble wall pressure must be uniform; namely

$$\int_{|\mathbf{z}-\mathbf{x}|=R} dS_z\, \mathbf{n}_z\, p_{bw}(\mathbf{z}, t|1) = \mathbf{0}, \tag{A.65}$$

so that

$$\alpha_D \mathcal{A}[p_C] = \mathbf{0}. \tag{A.66}$$

Also, the term $\alpha_D \mathcal{L}$ can be computed as

$$\alpha_D \mathcal{L}[p_C] = \frac{1}{3}\mathbf{I} \int dR_0\, d^3w\, d\dot{R} \int dR\, \mathcal{P}(1;t) R\, p_{bw}(t|1) \overbrace{\int_{|\mathbf{z}-\mathbf{x}|=R} dS_z}^{4\pi R^2} = \frac{4\pi}{3} n \overline{R^3 p_{bw}}\, \mathbf{I}. \tag{A.67}$$

The last quantity to be determined is the kinetic Reynolds stress tensor (A.56). In the dilute limit, this may be approximated by

$$\begin{aligned} \mathbf{M}_C &\approx -\Big\langle \big(\langle \mathbf{u}_C \rangle_1 - \langle \mathbf{u}_C \rangle\big)\big(\langle \mathbf{u}_C \rangle_1 - \langle \mathbf{u}_C \rangle\big) \Big\rangle_1 \\ &= -\int dR\, dR_0\, d^3w\, d\dot{R} \int_{|\mathbf{x}-\mathbf{y}|\geq R} d^3y\, \mathcal{P}(1;t) \big(\langle \mathbf{u}_C \rangle_1 - \langle \mathbf{u}_C \rangle\big)\big(\langle \mathbf{u}_C \rangle_1 - \langle \mathbf{u}_C \rangle\big). \end{aligned} \tag{A.68}$$

If relative motion between the two phases is negligible, the velocity fluctuation due to the oscillations of a bubble centered at $\mathbf{y}$ is

$$\langle \mathbf{u}_C \rangle_1 - \langle \mathbf{u}_C \rangle \approx \dot{R} R^2 \frac{\mathbf{x}-\mathbf{y}}{r^3}, \tag{A.69}$$

where $r = |\mathbf{x}-\mathbf{y}|$. Substituting equation (A.69) into equation (A.68) and changing the bubble center from $\mathbf{y}$ to $\mathbf{x}$ by Taylor's theorem, we find

$$\mathbf{M}_C \approx -\frac{4\pi}{3} n \overline{R^3 \dot{R}^2}\, \mathbf{I}. \tag{A.70}$$

With equations (A.66), (A.67) and (A.70), the momentum equation (A.58) is written as

$$\frac{\partial \langle \rho \rangle \langle \mathbf{u} \rangle}{\partial t} + \nabla \cdot \big(\langle \rho \rangle \langle \mathbf{u} \rangle \langle \mathbf{u} \rangle + \alpha_C \langle p_C \rangle \mathbf{I} \big) = -\nabla \left[\frac{4\pi}{3} n \left(\overline{R^3 p_{bw}} + \langle \rho \rangle \overline{R^3 \dot{R}^2} \right) \right]. \tag{A.71}$$

Furthermore, suppose that we can find bubbles equally in space, the void fraction can be expressed by

$$\alpha_D(\mathbf{x},t) = \int dR\, dR_0\, d^3w\, d\dot{R}\, \mathcal{P}(1;t) \int_{|\mathbf{x}-\mathbf{y}|\leq R} d^3y = \frac{4\pi}{3} n \overline{R^3}. \tag{A.72}$$

The momentum equation finally becomes

$$\frac{\partial\langle\rho\rangle\langle\mathbf{u}\rangle}{\partial t}+\nabla\cdot\left(\langle\rho\rangle\langle\mathbf{u}\rangle\langle\mathbf{u}\rangle+\alpha_C\langle p_C\rangle\mathbf{I}\right)=-\nabla\left[\alpha_D\left(\frac{\overline{R^3p_{bw}}}{\overline{R^3}}+\langle\rho\rangle\frac{\overline{R^3\dot{R}^2}}{\overline{R^3}}\right)\right]. \tag{A.73}$$

For simplicity, we omit the angular brackets for the ensemble-averaged quantities. Moreover, we replace the subscript C by l that denotes the liquid phase, and simply use α instead of α_D. The continuity (A.57) and the momentum equation (A.73) are then rewritten as

$$\frac{\partial\rho}{\partial t}+\nabla\cdot(\rho\mathbf{u})=0, \tag{A.74}$$

$$\frac{\partial\rho\mathbf{u}}{\partial t}+\nabla\cdot(\rho\mathbf{u}\mathbf{u}+p_l\mathbf{I})=\nabla\Bigg[\underbrace{\alpha\left(p_l-\frac{\overline{R^3p_{bw}}}{\overline{R^3}}-\rho\frac{\overline{R^3\dot{R}^2}}{\overline{R^3}}\right)}_{\tilde{p}}\Bigg], \tag{A.75}$$

where $\tilde{p}$ vanishes in the equilibrium state.

A.3.2 Bubble number conservation

Substituting $\varphi^{(1)}=1$ into equation (A.47), we find the conservation equation for the number density of bubbles of radius R,

$$\frac{\partial n_R}{\partial t}+\nabla\cdot(n_R\overline{\mathbf{w}}_R)+\frac{\partial}{\partial R}\left(n_R\overline{\dot{R}}_R\right)=0. \tag{A.76}$$

From equation (A.49), the total bubble number density requires

$$\frac{\partial n}{\partial t}+\nabla\cdot(n\overline{\mathbf{w}})=0. \tag{A.77}$$

Due to the no-slip assumption, we may replace $\overline{\mathbf{w}}$ with $\mathbf{u}$, so that

$$\frac{\partial n}{\partial t}+\nabla\cdot(n\mathbf{u})=0. \tag{A.78}$$

Hence, the total bubble number density is conserved in time. The evolution equation for the void fraction (A.72) is then described by

$$\frac{\partial \alpha}{\partial t} + \nabla \cdot (\alpha \mathbf{u}) = 3\alpha \frac{\overline{R^2 \dot{R}}}{\overline{R^3}}. \tag{A.79}$$

From equation (A.77), general transport theorem (A.49) becomes

$$\frac{\partial \overline{\varphi}}{\partial t} + \overline{\mathbf{w}} \cdot \nabla \overline{\varphi} - \frac{1}{n} \nabla \cdot \left[n \left(\overline{\varphi \mathbf{w}} - \overline{\varphi} \, \overline{\mathbf{w}} \right) \right] = \overline{\left(\frac{\partial \varphi^{(1)}}{\partial t} \right)}. \tag{A.80}$$

Specifically, for $\varphi^{(1)} = R$ and $\dot{R}$, we find

$$\overline{\dot{R}} = \frac{\partial \overline{R}}{\partial t} + \overline{\mathbf{w}} \cdot \nabla \overline{R} - \frac{1}{n} \nabla \cdot \left[n \left(\overline{R \mathbf{w}} - \overline{R} \, \overline{\mathbf{w}} \right) \right], \tag{A.81}$$

$$\overline{\ddot{R}} = \frac{\partial \overline{\dot{R}}}{\partial t} + \overline{\mathbf{w}} \cdot \nabla \overline{\dot{R}} - \frac{1}{n} \nabla \cdot \left[n \left(\overline{\dot{R} \mathbf{w}} - \overline{\dot{R}} \, \overline{\mathbf{w}} \right) \right]. \tag{A.82}$$

It follows from Zhang & Prosperetti (1994) that an ensemble-averaged Reyleigh-Plesset-type equation can be derived by directly averaging the equation of motion of the individual bubbles.

A.3.3 Model closure

To close the mixture model, there is a need to evaluate particle averaging $\overline{\varphi}(\mathbf{x}, t)$ where φ represents any of $R^3 p_{bw}$, $R^3 \dot{R}^2$, R^3 or $R^2 \dot{R}$. For computational efficiency, we should consider the probability function that is narrowly peaked around average values ($\hat{R}$, $\hat{\mathbf{w}}$, $\hat{\dot{R}}$) that are parameterized by R_0:

$$\mathcal{P}(1; t) \propto \delta \left(R - \hat{R}(\mathbf{x}, t; R_0) \right) \delta \Big(\mathbf{w} - \hat{\mathbf{w}}(\mathbf{x}, t; R_0) \Big) \delta \left(\dot{R} - \hat{\dot{R}}(\mathbf{x}, t; R_0) \right) f(R_0). \tag{A.83}$$

Here, the distribution of equilibrium radius, $f(R_0)$, is assumed uniform both in space and in time. This assumption is validated by the no-slip assumption. The narrowly peaked probability function implies that the bubble dynamics in the neighborhood of $\mathbf{x}$ coincide if the equilibrium radius is the same. This implication suggests that wavelengths in the averaged flow are larger than the mean

bubble spacing.

It follows from the narrow-peaked probability (A.83) that the particle-averaged quantity is computed by

$$\overline{\varphi}(\mathbf{x},t) = \int_0^\infty \varphi(\mathbf{x},t;R_0) f(R_0) dR_0, \tag{A.84}$$

where $f(R_0)$ satisfies $\int_0^\infty f(R_0) dR_0 = 1$.

Appendix B

Dimensionless bubble-dynamic equations

This appendix presents the normalization of the single-bubble-dynamic equations including the reduced-order model of Preston *et al.* (2007). For clarity, the superscript asterisk that denotes dimensionless variables is omitted in sections B.2 and B.3.

B.1 Nondimensional parameters

The single-bubble-dynamic time scale can be characterized by the natural frequency of bubble oscillations that depends on the equilibrium sizes (Brennen, 1995):

$$\omega_N = \frac{1}{R_0}\sqrt{3\kappa\frac{p_{l0}-p_v}{\rho_{l0}} + (3\kappa-1)\frac{2\Upsilon}{\rho_{l0}R_0}}. \tag{B.1}$$

The inverse of ω_N may be approximated by $R_0\sqrt{\rho_{l0}/p_{l0}}$. Time is normalized by the time scale, $R_0^{\mathrm{ref}}\sqrt{\rho_{l0}/p_{l0}}$, for the probable size R_0^{ref} among polydisperse mixtures. All length scales are normalized by R_0^{ref}. Nondimensional parameters governing the single bubble dynamics are a cavitation number Ca, a Reynolds number Re, a Weber number $\hat{\Upsilon}$, and Peclet numbers Pe for heat and mass transfers:

$$\mathrm{Ca} = \frac{p_{l0}-p_v}{p_{l0}}, \quad \mathrm{Re} = \sqrt{\frac{p_{l0}}{\rho_{l0}}}\frac{R_0^{\mathrm{ref}}}{\nu_l}, \quad \hat{\Upsilon} = \frac{p_{l0}R_0^{\mathrm{ref}}}{\Upsilon}, \quad \mathrm{Pe}_T = \sqrt{\frac{p_{l0}}{\rho_{l0}}}\frac{R_0^{\mathrm{ref}}}{\alpha_T}, \quad \mathrm{Pe}_\chi = \sqrt{\frac{p_{l0}}{\rho_{l0}}}\frac{R_0^{\mathrm{ref}}}{\mathcal{D}},$$

R_0^{ref} [μm]	1	10	100	1000
$R_0^{\mathrm{ref}}\sqrt{\rho_{l0}/p_{l0}}$ [s]	10^{-7}	10^{-6}	10^{-5}	10^{-4}
$2\pi/\omega_N(R_0^{\mathrm{ref}})$ [s]	2.59×10^{-7}	3.48×10^{-6}	3.63×10^{-5}	3.64×10^{-4}
Re	10.0	100	1000	10000
$\hat{\Upsilon}$	1.39	13.9	139	1390
Pe_T	1.16	5.50	48.8	482
Pe_χ	0.416	4.16	41.6	416

Table B.1: Time scales and nondimensional parameters for air bubbles of different equilibrium radii in water at STP. The air is assumed to behave isothermally ($\kappa = 1$). For bubbles of any size, $\mathrm{Ca} = 0.977$.

where ν_l is the kinematic viscosity of the liquid and α_T is the heat diffusivity of the bubble contents.

The dimensionless natural frequency ω_N^* is now written as

$$\omega_N^* = \frac{1}{R_0^*}\sqrt{3\kappa\mathrm{Ca} + \frac{2(3\kappa-1)}{\hat{\Upsilon}R_0^*}}, \tag{B.2}$$

where $R_0^* = R_0/R_0^{\mathrm{ref}}$ (the asterisk denotes dimensionless quantities). We also introduce the normalized radial coordinate (measured from the bubble center) and the pressure coefficients:

$$y = \frac{r}{R}, \quad C_{bw} = \frac{p_{bw} - p_{l0}}{p_{l0}}, \quad C_p = \frac{p_l - p_{l0}}{p_{l0}}.$$

For reference, table B.1 gives dimensional values of the time scale, $R_0^{\mathrm{ref}}\sqrt{\rho_{l0}/p_{l0}}$, and the natural period, $2\pi/\omega_N$, for air/vapor bubbles in water at STP, and the nondimensional parameters.

B.2 The Gilmore equation

The dimensionless Gilmore equation is

$$R\ddot{R}\left(1-\frac{\dot{R}}{C}\right) + \frac{3}{2}\dot{R}^2\left(1-\frac{\dot{R}}{3C}\right) = H\left(1+\frac{\dot{R}}{C}\right) + \frac{R\dot{H}}{C}\left(1-\frac{\dot{R}}{C}\right). \tag{B.3}$$

Here, the enthalpy H and sonic speed C at the bubble wall are written as

$$H = \frac{\gamma(p_{l0}+B)}{\gamma-1}\left[\left(\frac{C_{bw}}{p_{l0}+B}+1\right)^{\frac{\gamma-1}{\gamma}} - \left(\frac{C_p}{p_{l0}+B}+1\right)^{\frac{\gamma-1}{\gamma}}\right], \tag{B.4}$$

$$C = \sqrt{\gamma(p_{l0}+B)\left(\frac{C_p}{p_{l0}+B}+1\right)^{\frac{\gamma-1}{\gamma}} + (\gamma-1)H}, \tag{B.5}$$

where the bubble wall pressure coefficient is given by

$$C_{bw} = p_b - p_{l0} - \frac{4}{\mathrm{Re}}\frac{\dot{R}}{R} - \frac{2}{\hat{\Upsilon}R}. \tag{B.6}$$

In the incompressible limit (i.e., $\gamma \to \infty$), it is readily shown that $H \to C_{bw} - C_p$ and $C \to \infty$. As a result, the Gilmore equation (B.3) reduces to the well-known Rayleigh–Plesset equation (Rayleigh, 1917),

$$R\ddot{R} + \frac{3}{2}\dot{R}^2 = C_{bw} - C_p. \tag{B.7}$$

It is instructive to provide the computation of $\dot{H}$ in the Gilmore equation (B.3). From equation (B.4), we find

$$\dot{H} = \left(\frac{C_{bw}}{p_{l0}+B}+1\right)^{-\frac{1}{\gamma}}\dot{C}_{bw} - \left(\frac{C_p}{p_{l0}+B}+1\right)^{-\frac{1}{\gamma}}\dot{C}_p, \tag{B.8}$$

where $\dot{C}_p$ is given and $\dot{C}_{bw}$ is

$$\dot{C}_{bw} = \dot{p}_b + \left(\frac{4\dot{R}}{\mathrm{Re}} + \frac{2}{\hat{\Upsilon}}\right)\frac{\dot{R}}{R^2} - \frac{4}{\mathrm{Re}}\frac{\ddot{R}}{R}. \tag{B.9}$$

Substituting equations (B.8) and (B.9) into equation (B.3) and collecting terms involving $\ddot{R}$ on the left-hand side, we finally obtain

$$\begin{aligned} &R\ddot{R}\left(1-\frac{\dot{R}}{C}\right)\left[1+\frac{4}{\mathrm{Re}\,CR}\left(\frac{C_{bw}}{p_{l0}+B}+1\right)^{-\frac{1}{\gamma}}\right] + \frac{3}{2}\dot{R}^2\left(1-\frac{\dot{R}}{3C}\right) \\ &= H\left(1+\frac{\dot{R}}{C}\right) + \frac{R\dot{H}_{\mathrm{rhs}}}{C}\left(1-\frac{\dot{R}}{C}\right), \end{aligned} \tag{B.10}$$

where $\dot{H}_{\rm rhs}$ is given by

$$\dot{H}_{\rm rhs} = \left(\frac{C_{bw}}{p_{l0}+B}+1\right)^{-\frac{1}{\gamma}}\left[\dot{p}_b + \left(\frac{4\dot{R}}{\mathrm{Re}}+\frac{2}{\hat{\Upsilon}}\right)\frac{\dot{R}}{R^2}\right] - \left(\frac{C_p}{p_{l0}+B}+1\right)^{-\frac{1}{\gamma}}\dot{C}_p. \tag{B.11}$$

In two-way-coupled bubbly flows, the rate of change of the liquid pressure is given by

$$\dot{C}_p = \rho\tilde{c}_l^2\left(3\alpha\frac{\overline{R^3\dot{R}^2}}{\overline{R^3}} - \nabla\cdot\mathbf{u}\right), \tag{B.12}$$

which is obtained from equations (2.1) and (2.3).

B.3 Equations for bubble contents

The evolution of the internal bubble pressure is now written as

$$\dot{p}_b = \frac{3\gamma_b}{R}\left(-\dot{R}p_b + \mathfrak{R}_v T_w \dot{m}_v'' + p_{b0}\frac{k_{bw}}{\mathrm{Pe}_T R}\left.\frac{\partial T}{\partial y}\right|_w\right), \tag{B.13}$$

where p_{b0} is the internal bubble pressure in the equilibrium state, and the vapor flux at the bubble wall is governed by

$$\dot{m}_v'' = \frac{\rho_{bw}}{\mathrm{Pe}_\chi(1-\chi_{vw})R}\left.\frac{\partial \chi_v}{\partial y}\right|_w. \tag{B.14}$$

In order to estimate the temperature and concentration gradients at the bubble wall, we use the reduced-order model of Preston *et al.* (2007) that has been shown to be accurate for bubbles of small Peclet numbers:

$$\left.\frac{\partial T}{\partial y}\right|_w \approx -\Theta_T\left(\bar{T}-T_w\right), \tag{B.15}$$

$$\left.\frac{\partial \chi_v}{\partial y}\right|_w \approx -\Theta_\chi\left(\bar{\chi}_v-\chi_{vw}\right), \tag{B.16}$$

where the volume-averaged quantities are approximated by

$$\bar{\chi}_v \approx \frac{m_v}{m_{g0} + m_v}, \quad \bar{T} \approx \frac{p_b}{p_{b0}} \frac{R^3}{R_0^3} \frac{m_{g0} + m_{v0}}{m_{g0} + m_v}. \tag{B.17}$$

Here, the subscript 0 denotes the undisturbed values, m is mass, and the mass of vapor is updated by solving

$$\dot{m}_v = 4\pi R^2 \dot{m}_v''. \tag{B.18}$$

The constant transfer coefficients in equations (B.15) and (B.16) are approximated by

$$\Theta \approx \Re \left\{ \left[\left(\sqrt{j\mathrm{Pe}\, R_0^2\, \omega_N|_{\kappa=1}} \coth \sqrt{j\mathrm{Pe}\, R_0^2\, \omega_N|_{\kappa=1}} - 1 \right)^{-1} - \frac{3}{j\mathrm{Pe}\, R_0^2\, \omega_N|_{\kappa=1}} \right]^{-1} \right\}, \tag{B.19}$$

where j is the imaginary unit, $\omega_N|_{\kappa=1}$ is the isothermal natural frequency, and Pe_T and Pe_χ are used for Θ_T and Θ_χ, respectively. In the linear scenario, Preston's model is exact as the Peclet numbers approach zero.

Appendix C

Computation of phase velocity and attenuation

Consider a wave of form, $\exp[j(2\pi ft - kx)]$, where j is the imaginary unit, f is the temporal frequency and k is the complex wave number ($= k_r - jk_i$). Following Commander & Prosperetti (1989), the phase velocity $c^{\rm ph}$ and attenuation $a^{\rm att}$ (in decibels per unit length) are defined as

$$c^{\rm ph} = \frac{2\pi f}{k_r}, \quad a^{\rm att} = 20(\log_{10} e)k_i. \tag{C.1}$$

The real and imaginary parts of the complex wave number can be determined based on the time history of the computed liquid pressure as follows. The evolution of the normalized liquid pressure, $p' = (p_l - p_{l0})/(\epsilon p_{l0})$, is sampled at Δt at two different locations (say x_1 and x_2), and its discrete Fourier transform is then computed. The Fourier coefficients $\hat{p}'$ for the (discrete) frequency f can be written as

$$\hat{p}'(x, f) = \hat{p}'_0 \exp\big[-k_i(f)x\big] \exp\big[-jk_r(f)x\big]. \tag{C.2}$$

Given the complex ratio $P_{1,2} = \hat{p}'(x_1, f)/\hat{p}'(x_2, f)$, the complex wave number is computed as

$$k_r = \frac{1}{\Delta x_{1,2}} \cos^{-1}\big[\Re\{P_{1,2}\} \exp(-\ln|P_{1,2}|)\big], \quad k_i = \frac{1}{\Delta x_{1,2}} \ln|P_{1,2}|, \tag{C.3}$$

where $\Delta x_{1,2} = x_2 - x_1$.

Bibliography

Ando, K., Colonius, T. & Brennen, C. E. 2009 Improvement of acoustic theory of ultrasonic waves in dilute bubbly liquids. *J. Acoust. Soc. Am.* **126**, EL69–EL74.

Arndt, R. E. A. 1981 Cavitation in fluid machinery and hydraulic structures. *Annu. Rev. Fluid Mech.* **13**, 273–328.

Balsara, D. S. & Shu, C.-W. 2000 Monotonicity preserving weighted essentially non-oscillatory schemes with increasingly high order of accuracy. *J. Comput. Phys.* **160**, 405–452.

Batchelor, G. K. 1970 The stress system in a suspension of force-free particles. *J. Fluid Mech.* **41**, 545–570.

Batten, P., Clarke, N., Lambert, C. & Causon, D. M. 1997 On the choice of wavespeeds for the HLLC Riemann solver. *SIAM J. Sci. Comput.* **18**, 1553–1570.

Bergant, A. 2001 Developments in unsteady pipe flow friction modeling. *J. Hydraul. Res.* **39**, 249–257.

Bergant, A., Simpson, A. R. & Tijsseling, A. S. 2006 Water hammer with column separation: A historical review. *J. Fluids Struct.* **22**, 135–171.

Beylich, A. E. & Gülhan, A. 1990 On the structure of nonlinear waves in liquids with gas bubbles. *Phys. Fluids A* **2**, 1412–1428.

Biesheuvel, A. & van Wijngaarden, L. 1984 Two-phase flow equations for a dilute dispersion of gas bubbles in liquid. *J. Fluid Mech.* **148**, 301–318.

Bird, R. B., Stewart, W. E. & Lightfoot, E. N. 1960 *Transport Phenomena*. Wiley.

Bleich, H. H. & Sandler, I. S. 1970 Interaction between structures and bilinear fluids. *Int. J. Solids Struct.* **6**, 617–639.

Brennen, C. E. 1994 *Hydrodynamics of Pumps*. Oxford University Press.

Brennen, C. E. 1995 *Cavitation and Bubble Dynamics*. Oxford University Press.

Brennen, C. E. 2002 Fission of collapsing cavitation bubbles. *J. Fluid Mech.* **472**, 153–166.

Brennen, C. E. 2005 *Fundamentals of Multiphase Flow*. Cambridge University Press.

Brett, J. M. & Yiannakopolous, G. 2008 A study of explosive effects in close proximity to a submerged cylinder. *Int. J. Impact Eng.* **35**, 206–225.

Brett, J. M., Yiannakopolous, G. & van der Schaaf, P. J. 2000 Time-resolved measurement of the deformation of submerged cylinders subjected to loading from a nearby explosion. *Int. J. Impact Eng.* **24**, 875–890.

Campbell, I. J. & Pitcher, A. S. 1958 Shock waves in a liquid containing gas bubbles. *Proc. R. Soc. Lond. A* **243**, 534–545.

Carstensen, E. L. & Foldy, L. L. 1947 Propagation of sound through a liquid containing bubbles. *J. Acoust. Soc. Am.* **19**, 481–501.

Chahine, G. L. 1982 Cloud cavitation: Theory. In *Proceedings of the Fourteenth ONR Symposium on Naval Hydrodynamics*, pp. 165–194.

Chambers, G., Sandusky, H., Zerilli, F., Rye, K., Tussing, R. & Forbes, J. 2001 Pressure measurements on a deforming surface in response to an underwater explosion in a water-filled aluminum tube. *Shock Vib.* **8**, 1–7.

Cole, R. H. 1948 *Underwater Explosions*. Princeton University Press.

Colonius, T., d'Auria, F. & Brennen, C. E. 2000 Acoustic saturation in bubbly cavitating flow adjacent to an oscillating wall. *Phys. Fluids* **12**, 2752–2761.

Colonius, T., Hagmeijer, R., Ando, K. & Brennen, C. E. 2008 Statistical equilibrium of bubble oscillations in dilute bubbly flows. *Phys. Fluids* **20**, 040902.

Commander, K. W. & Prosperetti, A. 1989 Linear pressure waves in bubbly liquids: Comparison between theory and experiments. *J. Acoust. Soc. Am.* **85**, 732–746.

Covas, D., Stoianov, I., Mano, J., Romas, H., Graham, N. & Maksimovic, C. 2004 The dynamic effect of pipe-wall viscoelasticity in hydraulic transients (Part I—experimental analysis and creep characterization). *J. Hydraul. Res.* **42**, 516–530.

Dadone, A. & Grossman, B. 1994 Surface boundary conditions for the numerical solution of the Euler equations. *AIAA J.* **32**, 285–293.

d'Agostino, L. & Brennen, C. E. 1989 Linearized dynamics of spherical bubble clouds. *J. Fluid Mech.* **199**, 155–176.

d'Agostino, L., Brennen, C. E. & Acosta, A. J. 1988 Linearized dynamics of two-dimensional bubbly and cavitating flows over slender surfaces. *J. Fluid Mech.* **192**, 485–509.

Dashpande, V. S., Heaver, A. & Fleck, N. A. 2006 An underwater shock simulator. *Proc. R. Soc. A* **462**, 1021–1041.

Delale, C. F., Nas, S. & Tryggvason, G. 2005 Direct numerical simulations of shock propagation in bubbly liquids. *Phys. Fluids* **17**, 121705.

Delale, C. F. & Tryggvason, G. 2008 Shock structure in bubbly liquids: comparison of direct numerical simulations and model equations. *Shock Waves* **17**, 433–440.

Domenico, S. N. 1982 Acoustic wave propagation in air-bubble curtains in water—Part I: History and theory. *Geophysics* **47**, 345–353.

Einfeldt, B., Munz, C. D., Roe, P. L. & Sjögreen, B. 1991 On Godunov-type methods near low densities. *J. Comput. Phys.* **92**, 273–295.

Eldridge, J. E., Fye, P. M. & Spitzer, R. W. 1950 Photography of underwater explosions: I. In *Underwater Explosion Research (Volume 1. The Shock Wave)* (ed. G. K. Hartmann & E. G. Hill), pp. 969–1052. Office of Naval Research.

Espinosa, H. D., Lee, S. & Moldovan, N. 2006 A novel fluid structure interaction experiment to investigate deformation of structural elements subjected to impulsive loading. *Exp. Mech.* **46**, 805–824.

Feuillade, C. 1996 The attenuation and dispersion of sound in water containing multiply interacting air bubbles. *J. Acoust. Soc. Am.* **99**, 3412–3430.

Fujikawa, S. & Akamatsu, T. 1980 Effects of the non-equilibrium condensation of vapour on the pressure wave produced by the collapse of a bubble in a liquid. *J. Fluid Mech.* **97**, 481–512.

Gally, M., Güney, M. & Rieutord, E. 1979 An investigation of pressure transients in viscoelastic pipes. *J. Fluids Eng.* **101**, 495–499.

Gilmore, F. R. 1952 The collapse and growth of a spherical bubble in a viscous compressible liquid. Hydrodynamics Laboratory Report 26-4. California Institute of Technology.

Gottlieb, S. & Shu, C.-W. 1998 Total variation diminishing Runge-Kutta schemes. *Math. Compt.* **67**, 73–85.

Harten, A., Engquist, B., Osher, S. & Chakravarthy, S. R. 1987 Uniformly high order accurate essentially non-oscillatory schemes, III. *J. Comput. Phys.* **71**, 231–303.

Harten, A., Lax, P. D. & van Leer, B. 1983 On upstream differencing and Godunov-type schemes for hyperbolic conservation laws. *SIAM Rev.* **25**, 35–61.

Inaba, K. & Shepherd, J. E. 2010 Flexural waves in fluid-filled tubes subject to axial impact. *J. Pressure Vessel Technol.* **132**, 021302.

Johnsen, E. 2007 Numerical simulations of non-spherical bubble collapse: With applications to shockwave lithotripsy. PhD Thesis, California Institute of Technology.

Johnsen, E. & Colonius, T. 2009 Numerical simulations of non-spherical bubble collapse. *J. Fluid Mech.* **629**, 231–262.

Joukowsky, N. E. 1898 Memoirs of the Imperial Academy Society of St. Petersburg. *Proc. Amer. Water Works Assoc.* **24**, 341–424.

Kameda, M. & Matsumoto, Y. 1996 Shock waves in a liquid containing small gas bubbles. *Phys. Fluids* **8**, 322–335.

Kameda, M., Shimaura, N., Higashino, F. & Matsumoto, Y. 1998 Shock waves in a uniform bubbly flow. *Phys. Fluids* **10**, 2661–2668.

Katz, J. 1978 Determination of solid nuclei and bubble distributions in water by holography. Engineering and Applied Science Division Report 183-3. California Institute of Technology.

Kedrinskii, V. K. 2005 *Hydrodynamics of Explosion*. Springer.

Kennard, E. H. 1950 Explosive load on underwater structures as modified by bulk cavitation. In *Underwater Explosion Research (Volume 3. The Damage Process)* (ed. G. K. Hartmann & E. G. Hill), pp. 227–253. Office of Naval Research.

Kobori, T., Yokoyama, S. & Miyashiro, H. 1955 Propagation velocity of pressure wave in pipe line. *Hitachi Hyoron* **37**, 33–37.

Korteweg, D. J. 1878 Ueber die Fortpflanzungsgeschwindigkeit des Shalles in elastischen Röhren. *Annalen der Physik und Chemie* **5**, 525–542.

Kuznetsov, V. V., Nakoryakov, V. E., Pokusaev, B. G. & Shreiber, I. R. 1978 Propagation of perturbations in a gas-liquid mixture. *J. Fluid Mech.* **85**, 85–96.

LeVeque, R. J. 1992 *Numerical Methods for Conservation Laws*. Basel: Birkhäuser Verlag.

LeVeque, R. J. 2002 *Finite Volume Methods for Hyperbolic Problems*, 2nd edn. New York: Cambridge University Press.

Lide, D. R., ed. 2006 *CRC Handbook of Chemistry and Physics*, 87th edn., chap. 6. CRC Press.

Liu, X.-D., Osher, S. & Chan, T. 1994 Weighted essentially non-oscillatory schemes. *J. Comput. Phys.* **115**, 200–212.

Mair, H. U. 1999 Benchmarks for submerged structure response to underwater explosions. *Shock Vib.* **6**, 169–181.

Matsumoto, Y. & Kameda, M. 1996 Propagation of shock waves in dilute bubbly liquids (Governing equations, Hugoniot relations, and effect of slippage between two phases). *JSME Int. J. Ser. B* **39**, 264–272.

Meissner, E. & Frank, P.-G. 1977 Influence of pipe material on the damping of water hammer. In *Proceedings of the Seventeenth Congress of the International Association for Hydraulic Research.*

Nagayama, K., Mori, Y. & Shimada, K. 2002 Shock Hugoniot compression curve for water up to 1 GPa by using a compressed gas gun. *J. Appl. Phys.* **91**, 476–482.

Nigmatulin, R. I. 1979 Spatial averaging in the mechanics of heterogeneous and dispersed systems. *Int. J. Heat Mass Transfer* **5**, 353–385.

Nigmatulin, R. I., Khabeev, N. S. & Hai, Z. N. 1988 Waves in liquids with vapour bubbles. *J. Fluid Mech.* **186**, 85–117.

Nigmatulin, R. I., Khabeev, N. S. & Nagiev, F. B. 1981 Dynamics, heat and mass transfer of vapour-gas bubbles in a liquid. *Int. J. Heat Mass Transfer* **24**, 1033–1044.

Noordzij, L. & van Wijngaarden, L. 1974 Relaxation effects, caused by relative motion, on shock waves in gas-bubble/liquid mixtures. *J. Fluid Mech.* **66**, 115–143.

Nurick, G. N. & Martin, J. B. 1989 Deformation of thin plates subjected to impulsive loading—a review (Part II: Experimental studies). *Int. J. Impact Eng.* **8**, 171–186.

O'Hern, T. J., d'Agostino, L. & Acosta, A. J. 1988 Comparison of holographic and Coulter Counter measurements of cavitation nuclei in the ocean. *J. Fluids Eng.* **110**, 200–207.

Omta, R. 1987 Oscillations of a cloud of bubbles of small and not so small amplitude. *J. Acoust. Soc. Am.* **82**, 1018–1033.

Plesset, M. S. & Prosperetti, A. 1977 Bubble dynamics and cavitation. *Annu. Rev. Fluid Mech.* **9**, 145–185.

Press, W. H., Teukolsky, S. A., Vetterling, W. T. & Flannery, B. P. 1994 *Numerical Recipes in FORTRAN: The Art of Scientific Computing*, 2nd edn. Cambridge University Press.

Preston, A. T., Colonius, T. & Brennen, C. E. 2007 A reduced-order model of diffusive effects on the dynamics of bubbles. *Phys. Fluids* **19**, 123302.

Prosperetti, A. 2001 Fundamental acoustic properties of bubbly liquids. In *Handbook of Elastic Properties of Solids, Liquids, and Gases (Volume 4. Elastic Properties of Fluids: Liquids and Gases)* (ed. M. Levy, H. E. Bass & R. R. Stern), pp. 183–205. Academic.

Prosperetti, A., Crum, L. A. & Commander, K. W. 1988 Nonlinear bubble dynamics. *J. Acoust. Soc. Am.* **83**, 502–514.

Prosperetti, A. & Lezzi, A. 1986 Bubbly dynamics in a compressible liquid (Part 1. First-order theory). *J. Fluid Mech.* **168**, 457–478.

Qiu, J. & Shu, C.-W. 2002 On the construction, comparison, and local characteristic decomposition for high-order central WENO schemes. *J. Comput. Phys.* **183**, 187–209.

Rajendran, R. 2008 Reloading effects on plane plates subjected to non-contact underwater explosion. *J. Mater. Process. Technol.* **206**, 275–281.

Rajendran, R. & Narasimhan, K. 2006*a* Deformation and fracture behavior of plate specimens subjected to underwater explosion—a review. *Int. J. Impact Eng.* **32**, 1945–1963.

Rajendran, R. & Narasimhan, K. 2006*b* A shock factor based approach for the damage assessment of plane plates subjected to underwater explosion. *J. Strain Anal. Eng. Des.* **41**, 417–425.

Rajendran, R. & Satyanarayana, K. H. B. S. 1997 Interaction of finite amplitude acoustic wave with a plane plate. *J. Acoust. Soc. India* **25**, V5.1–7.

Rayleigh, Lord 1917 On the pressure developed in a liquid during the collapse of a spherical cavity. *Phil. Mag.* **34**, 94–98.

Roe, P. L. 1981 Approximate Riemann solvers, parameter vectors, and difference schemes. *J. Comput. Phys.* **43**, 357–372.

Shepherd, J. E. & Inaba, K. 2009 Shock loading and failure of fluid-filled tubular structures. In *Dynamic Failure of Materials and Structures* (ed. A. Shukla, G. Ravichandran & Y. D. S. Rajapakse), pp. 153–190. Springer.

Shimada, M., Matsumoto, Y. & Kobayashi, T. 2000 Influence of the nuclei size distribution on the collapsing behavior of the cloud cavitation. *JSME Int. J., Ser. B* **43**, 380–385.

Shu, C.-W. 1997 Essentially non-oscillatory and weighted essentially non-oscillatory schemes for hyperbolic conservation laws. ICASE Report 97-65. NASA Langley Research Center.

Shu, C.-W. & Osher, S. 1988 Efficient implementation of essentially non-oscillatory shock-capturing schemes. *J. Comput. Phys.* **77**, 439–471.

Skalak, R. 1956 An extension of the theory of water hammer. *Trans. ASME* **78**, 105–116.

Smereka, P. 2002 A Vlasov equation for pressure wave propagation in bubbly fluids. *J. Fluid Mech.* **454**, 287–325.

Sportisse, B. 2000 An analysis of operator splitting techniques in the stiff case. *J. Comput. Phys.* **161**, 140–168.

Strang, G. 1968 On the construction and comparison of difference schemes. *SIAM J. Numer. Anal.* **5**, 506–517.

Suo, L. & Wylie, E. B. 1990 Complex wavespeed and hydraulic transients in viscoelastic pipes. *J. Fluids Eng.* **112**, 496–500.

Takahira, H. 2004 A remark on the pressure terms in the Rayleigh-Plesset equation for cavitating flows. *Trans. Jpn. Soc. Mech. Eng. B* **70**, 617–622.

Taylor, G. I. 1950 The pressure and impulse of submarine explosion waves on plates. In *Underwater Explosion Research (Volume 1. The Shock Wave)* (ed. G. K. Hartmann & E. G. Hill), pp. 1155–1173. Office of Naval Research.

Temperley, H. N. V. 1950 Theoretical investigation of cavitation phenomena occurring when an underwater pressure pulse is incident on a yielding surface: I. In *Underwater Explosion Research (Volume 3. The Damage Process)* (ed. G. K. Hartmann & E. G. Hill), pp. 255–268. Office of Naval Research.

Thompson, K. W. 1987 Time dependent boundary conditions for hyperbolic systems. *J. Comput. Phys.* **68**, 1–24.

Thompson, P. A. 1972 *Compressible-Fluid Dynamics*. McGraw-Hill.

Tijsseling, A. S. 1996 Fluid-structure interaction in liquid-filled pipe systems: A review. *J. Fluids Struct.* **10**, 109–146.

Tijsseling, A. S., Lambert, M. F., Simpson, A. R., Stephens, M. L., Vítkovský, J. P. & Bergant, A. 2008 Skalak's extended theory of water hammer. *J. Sound Vib.* **310**, 718–728.

Toro, E. F. 1999 *Riemann Solvers and Numerical Methods for Fluid Dynamics: A Practical Introduction*, 2nd edn. New York: Springer.

Toro, E. F., Spruce, M. & Speares, W. 1994 Restoration of the contact surface in the HLL-Riemann solver. *Shock Waves* **4**, 25–34.

van Wijngaarden, L. 1964 On the collective collapse of a large number of gas bubbles in water. In *Proceedings of the Eleventh International Congress on Applied Mechanics*.

van Wijngaarden, L. 1968 On the equations of motion for mixtures of liquid and gas bubbles. *J. Fluid Mech.* **33**, 465–474.

van Wijngaarden, L. 1972 One-dimensional flow of liquids containing small gas bubbles. *Annu. Rev. Fluid Mech.* **4**, 369–396.

Wang, Y.-C. 1999 Effects of nuclei size distribution on the dynamics of a spherical cloud of cavitation bubbles. *J. Fluids Eng.* **121**, 881–886.

Wang, Y.-C. & Brennen, C. E. 1999 Numerical computation of shock waves in a spherical cloud of cavitation bubbles. *J. Fluids Eng.* **121**, 872–880.

Wardlaw, A. B. & Luton, J. A. 2000 Fluid-structure interaction mechanisms for close-in explosions. *Shock Vib.* **7**, 265–275.

Watanabe, M. & Prosperetti, A. 1994 Shock waves in dilute bubbly liquids. *J. Fluid Mech.* **274**, 349–381.

Waterman, P. C. & Truell, R. 1961 Multiple scattering of waves. *J. Math. Phys.* **2**, 512–537.

Wylie, E. B. & Streeter, V. L. 1993 *Fluid Transients in Systems*. Prentice Hall.

Xie, W. F., Liu, Z. K. & Young, Y. L. 2009 Application of a coupled Eulerian–Lagrangian method to simulate interactions between deformable composite structures and compressible multiphase flow. *Int. J. Numer. Methods Eng.* **80**, 1497–1519.

Xie, W. F., Young, Y. L. & Liu, T. G. 2008 Multiphase modeling of dynamic fluid-structure interaction during close-in explosion. *Int. J. Numer. Methods Eng.* **74**, 1019–1043.

Xie, W. F., Young, Y. L., Liu, T. G. & Khoo, B. C. 2007 Dynamic response of deformable structures subjected to shock load and cavitation reload. *Comput. Mech.* **40**, 667–681.

Zhang, Z. D. & Prosperetti, A. 1994 Ensemble-averaged equations for bubbly flows. *Phys. Fluids* **6**, 2956–2970.

Zhang, Z. D. & Prosperetti, A. 1997 Momentum and energy equations for disperse two-phase flows and their closure for dilute suspensions. *Int. J. Multiphase Flow* **23**, 425–453.